PACIFIC EARTHQUAKE ENGINEERING RESEARCH CENTER

Identification of Site Parameters that Improve Predictions of Site Amplification

Ellen M. Rathje
Sara Navidi

Department of Civil, Architectural, and Environmental Engineering
University of Texas at Austin

PEER 2013/18
JULY 2013

Identification of Site Parameters that Improve Predictions of Site Amplification

Ellen M. Rathje

Sara Navidi

Department of Civil, Architectural, and Environmental Engineering
University of Texas at Austin

PEER Report 2013/18
Pacific Earthquake Engineering Research Center
Headquarters at the University of California, Berkeley

July 2013

ABSTRACT

The effects of the local soil conditions on earthquake shaking are often quantified via an amplification factor, which is defined as the ratio of the ground motion at the soil surface to the ground motion at a rock site at the same location. Site amplification models are empirical equations that predict site amplification based on the general characteristics of the site. Most of the current site amplification models predict amplification based on the average shear wave velocity in the top 30 m (V_{S30}). However, additional site parameters influence site amplification and should be included in site amplification models.

To identify site parameters beyond V_{S30} that influence site amplification and to develop an empirical site amplification model that includes these parameters, site response analyses are performed for a large suite of shear wave velocity profiles. These analyses identified the parameter V_{ratio}, defined as the ratio of the average shear wave velocity from 20 m and 30 m to the average shear wave velocity in the top 10 m, as an important site parameter that influences site amplification. An empirical site amplification model is developed based on the site response results that predicts amplification as a function of V_{s30}, V_{ratio}, spectral acceleration on rock, and depth to rock.

ACKNOWLEDGMENTS

This study was sponsored by the Pacific Earthquake Engineering Research Center's (PEER) Program of Applied Earthquake Engineering Research of Lifelines Systems supported by the California Department of Transportation and the Pacific Gas & Electric Company. Any opinions, findings, and conclusions or recommendations expressed in this material are those of the authors and do not necessarily reflect those of the sponsoring organizations.

CONTENTS

LIST OF FIGURES

LIST OF TABLES

1 Study Overview

1.1 INTRODUCTION

When an earthquake occurs, seismic waves are released at the source, travel through the earth, and generate ground shaking at the ground surface. The characteristics of shaking at a site depend on the source characteristics, and these characteristics change as they travel through their path to get to the site. The wave amplitudes generally attenuate with distance and are modified by the local soil conditions at the site (i.e., site effects). The important characteristic of the local soil conditions that influence ground shaking is the shear wave velocity profile.

The effects of local soil conditions are often quantified via an amplification factor (AF), which is defined as the ratio of the ground motion at the soil surface to the ground motion at a rock site at the same location. Although AFs can be defined for any ground motion parameter, they are most commonly assessed for acceleration response spectral values (Sa) at different periods.

Empirical estimates of site amplification are often used to evaluate site effects. This approach uses an empirical equation to predict site amplification based on the input motion intensity and the general characteristics of a site. This approach is incorporated in empirical ground motion prediction equations (GMPEs), which are statistical models that predict an acceleration response spectrum at a site as a function of earthquake magnitude (M), site to source distance (R), local site conditions, and other parameters. These GMPEs are developed predominantly from recorded ground motions obtained from previous earthquakes. To account for local site conditions, GMPEs characterize sites simply by one or two parameters (e.g., the average shear wave velocity over the top 30 m, V_{s30}), and the amplification at each period is related to these parameters. The amplification relationship included in a GMPE is often called a site response or site amplification model. While these models are relatively simple and ignore important details about the shear wave velocity profile and nonlinear properties at a site, they are important tools in estimating site amplification for a range of applications. Yet enhancements in these models can be made to improve their ability to predict site amplification.

The main objective of this research is to improve the site amplification models included in GMPEs. Important site details that control site amplification are identified and statistical models are developed that include these parameters. These models or their functional forms then can be implemented in GMPEs. To meet these objectives, first the important site parameters that influence site amplification are identified. To identify these site parameters, hypothetical shear wave velocity profiles are generated manually and their seismic response computed using the equivalent linear approach. Various site parameters are computed from the hypothetical velocity profiles and the relationship between each of these parameters and the computed site amplification. After identifying appropriate site parameters for use in the empirical site amplification model, appropriate functional forms for the statistical model are developed. The developed functional forms are fit to the computed amplification data.

1.2 SITE AMPLIFICATION MODELS

Site amplification has been included in GMPEs for several decades. The initial site amplification models simply distinguished between rock and soil sites and incorporated site amplification by a scaling parameter or by defining different statistical models for soil and rock sites (e.g., Boore et al. [1993]; Campbell [1993]; Sadigh et al. [1997]). Current models explicitly use V_{s30} and also include the effects of soil nonlinearity, where the stiffness of the soil decreases and the damping increases as larger shear strains are induced in the soil. As a result of soil nonlinearity, amplification is a nonlinear function of the input rock motion. Some models also include the effects of depth to rock, which is important for long-period amplification.

Site amplification models typically predict the natural log of the amplification factor and the effect can be separated into the linear elastic and nonlinear components:

$$\ln(\mathrm{AF}) = \ln(\mathrm{AF})_{\mathrm{lin}} + \ln(\mathrm{AF})_{\mathrm{nl}} \tag{1.1}$$

Boore et al. [1997] were the first to use V_{S30} in their site amplification model. Their model only included the linear elastic component and is written as:

$$\ln(\mathrm{AF}) = \mathrm{a} \cdot \ln\left(\frac{\mathrm{V_{s30}}}{\mathrm{V_{ref}}}\right) \tag{1.2}$$

where a and V_{ref} are coefficients estimated by regression. This model results in amplification decreasing log-linearly with an increase in V_{S30} (i.e., the coefficient a is negative).

Choi and Stewart [2005] expanded the Boore et al. [1997] site amplification model to include both linear and nonlinear site amplification effects. The general form of the model is given as:

$$\ln(\mathrm{AF}) = \mathrm{a} \cdot \ln\left(\frac{\mathrm{V_{s30}}}{\mathrm{V_{ref}}}\right) + \mathrm{b} \cdot \ln\left(\frac{\mathrm{PGA_{rock}}}{0.1g}\right) \tag{1.3}$$

where PGA_{rock} is the peak ground acceleration on rock in units of g and $0.1g$ is the reference PGA_{rock} level for nonlinear behavior. The coefficient b is generally negative, indicating that amplification decreases with increasing PGA_{rock}. The Choi and Stewart [2005] model was developed by considering recorded ground motions at sites with known V_{S30} and computing the difference between the observed ln(Sa) and the ln(Sa) predicted by an empirical GMPE for rock conditions. This difference represents ln(AF) because the observed motion is $\ln(Sa_{soil})$ and the predicted motion on rock is $\ln(Sa_{rock})$. Using the observed ln(AF), Choi and Stewart [2005] found that b generally decreases towards zero as V_{S30} increases (Figure 1.1). This decrease in b with increasing V_{S30} indicates that nonlinearity becomes less significant as sites become stiffer.

Chiou and Youngs [2008] used a modified version of Choi and Stewart [2005] site amplification model in their GMPE. While Choi and Stewart [2005] normalized PGA_{rock} by 0.1*g*, Chiou and Youngs [2008] use the following form:

$$\ln(\mathrm{AF}) = \mathrm{a} \cdot \ln\left(\frac{V_{s30}}{V_{ref}}\right) + \mathrm{b} \cdot \ln\left(\frac{Sa_{rock} + c}{c}\right) \tag{1.4}$$

This functional form uses Sa_{rock} instead of $PGA_{rock,}$ and separates the linear and nonlinear components through the term $\ln\left(\frac{Sa_{rock}+c}{c}\right)$, which tends towards zero for small Sa_{rock}. Again, the coefficient b is V_{S30}-dependent.

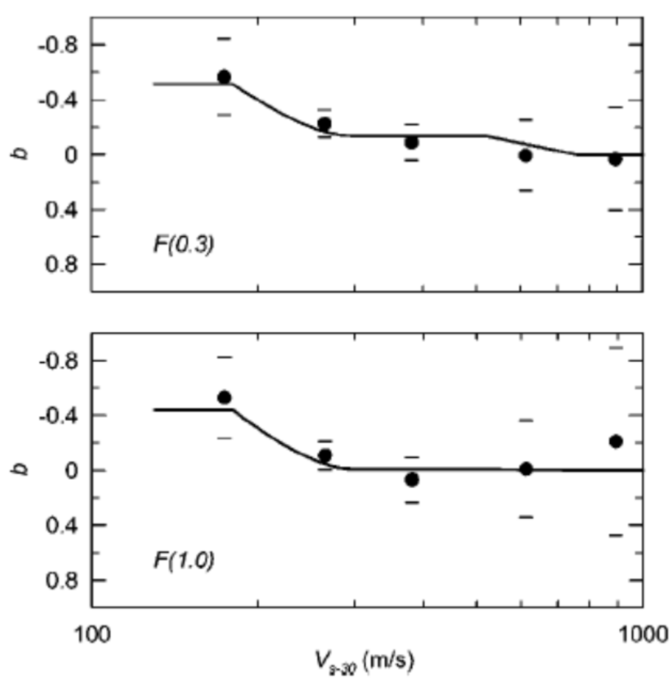

Figure 1.1 Derived values of coefficient b as a function of V_{S30} for periods of 0.3 and 1.0 sec [Choi and Stewart 2005].

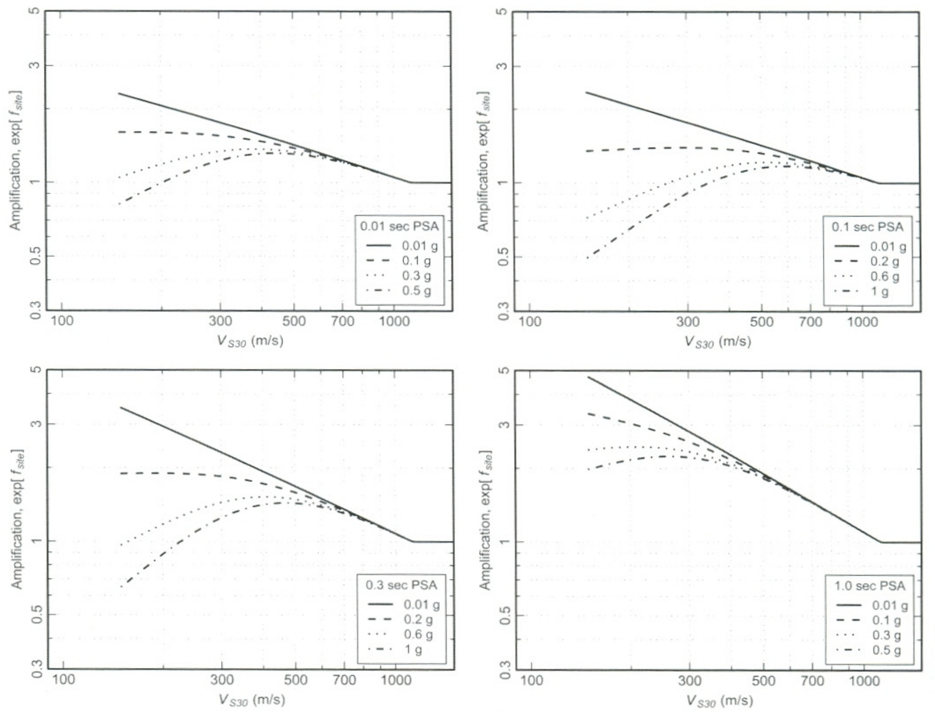

Figure 1.2 Site amplification as a function of spectral period, V_{S30}, and input motion intensity [Chiou and Youngs 2008].

Other functional forms for site amplification models are available (e.g., Walling et al. [2008]), but all generally attempt to model the effect of V_{s30} and soil nonlinearity. As an example of how these models predict amplification, Figure 1.2 plots amplification versus V_{S30} for different input intensities as predicted by the Chiou and Youngs [2008] model. Amplification is shown for spectral periods of 0.01, 0.1, 0.3, and 1.0 sec. At small input intensities (i.e., 0.01*g*) where the linear term dominates, amplification increases log-linearly as V_{S30} decreases. This effect is larger at longer periods. At larger input intensities, the amplification at each V_{S30} is reduced due to soil nonlinearity (i.e., soil stiffness reduction and increased damping). This effect is largest at small V_{S30} and shorter periods.

Some site amplification models (e.g., Abrahamson and Silva [2008], Campbell and Bozorgnia [2008], and Chiou and Youngs [2008]) include a soil-depth term in addition to V_{S30} when predicting site amplification at long periods. Because the natural period of a soil site is proportional to the soil depth (i.e., deeper sites have longer natural periods), deeper soil sites will experience more amplification at long periods than shallow soil sites. The scaling of site amplification with soil depth is commonly considered independent of input intensity (i.e., not influenced by soil nonlinearity).

The soil-depth term is defined based on the depth to a specific shear wave velocity horizon. Some models (e.g., Abrahamson and Silva [2008] and Chiou and Youngs [2008]) use the depth to V_S equal to or greater than 1.0 km/sec (called $Z_{1.0}$), while others (i.e., Campbell and Bozorgnia [2008]) use the depth to V_S equal to or greater than 2.5 km/sec (called $Z_{2.5}$).

Essentially, $Z_{1.0}$ represents the depth to "engineering" rock while $Z_{2.5}$ represents the depth to hard rock.

As noted previously, soil depth predominantly affects long-period amplification because soil depth affects the natural period of a site and the associated periods of amplification. Figure 1.3 shows the predicted acceleration response spectra for a soil site with V_{S30} = 270 m/sec and different values of $Z_{1.0}$ as predicted by the Abrahamson and Silva [2008] GMPE for a M = 7.0 earthquake at a distance of 30 km. At short periods (less than 0.4 sec) $Z_{1.0}$ does not influence the response spectrum, while at longer periods the response spectra are significantly affected by $Z_{1.0}$. For example, at a spectral period of 1.0 sec the spectral acceleration for $Z_{1.0}$ = 0.1 km is 0.08*g* while the spectral acceleration for $Z_{1.0}$ = 1.1 km is close to 0.25*g*. This represents an amplification of greater than 3.0. At longer periods the effect of $Z_{1.0}$ is even more pronounced. At a spectral period of 5.0 sec, the response spectra in Figure 1.3 indicate an amplification of greater than 4.0 between $Z_{1.0}$ = 0.1 km and 1.1 km.

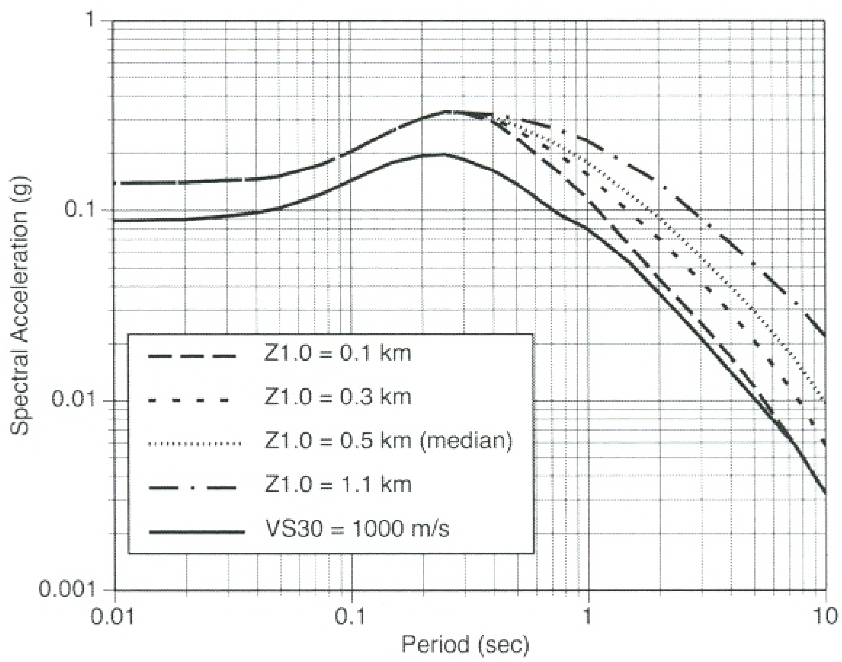

Figure 1.3 Effect of soil depth on ground shaking for a site with V_{s30} = 270 m/sec [Abrahamson and Silva 2008].

2 Identification of Site Parameters that Influence Site Amplification

2.1 INTRODUCTION

While the average shear wave velocity in top 30 m (V_{S30}) and depth to rock ($Z_{1.0}$ or $Z_{2.5}$) are considered important site parameters that influence site amplification, this research aims to identify additional site parameters to improve site amplification predictions in empirical GMPEs. First we performed wave propagation analysis (i.e., site response analysis) for sites with different velocity profiles and related the computed amplification factors to characteristics of the site profiles. This study focuses on parameters that could be determined from the shear wave velocity profile within the top 30 m of the ground surface because the shear wave velocity information below 30 m is not always available.

In this exploratory part of the research, 99 V_s profiles were generated manually and analyzed by the equivalent-linear site response program *Strata* [Kottke and Rathje 2008]. The manually generated profiles allow for different velocity structures within the top 30 m while at the same time maintaining a constant V_{S30}. Amplification factors were then calculated for all the generated profiles at multiple input intensities and spectral periods. These data were used to identify parameters that strongly influence site amplification.

2.2 SITE PROFILES

Profiles with the same average shear wave velocity (V_{S30}) but different shear wave velocity structures within the top 30 m were generated. The profiles also had the same depth to engineering rock ($Z_{1.0}$ = 150 m). The same V_{S30} and $Z_{1.0}$ in the profiles facilitates investigation of other site parameters that influence the site response. Profiles of 150 m depth are developed for five different V_{S30} values (V_{S30} = 225, 280, 350, 450, and 550 m/sec) using the baseline profiles shown in Figure 2.1. For each V_{S30} value, the profiles were manually varied in the top 30 m (keeping V_{S30} constant) with the profiles below 30 m kept at the baseline values. The half space below 150 m for all baseline profiles had a V_S equal to 1100 m/sec. Eighteen to 24 profiles were generated for each V_{S30} value, and 99 total profiles were analyzed.

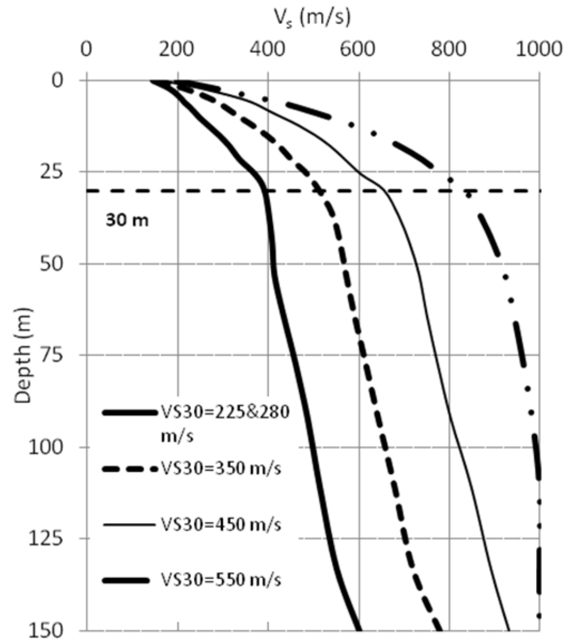

Figure 2.1 Baseline shear wave velocity profiles used for each V_{S30} value.

The top 50 m of all of the generated profiles, along with the baseline profile, for each V_{S30} value are shown in Figure 2.2. In all the generated profiles, the velocity increased with depth with no inversion in the shear wave velocity (i.e., an inversion is when a smaller V_S is found below a larger V_S). The minimum shear wave velocity was limited to 100 m/sec in the generated profiles, and for each V_{S30} the profiles all had the same maximum V_S as controlled by the baseline velocity profile at 30 m.

In addition to the shear wave velocity profile, the unit weight and the shear modulus reduction and damping curves of the soil layers were required for site response analysis. The shear modulus reduction and damping curves describe the variation of the shear modulus and damping ratio with shear strain, and represent the nonlinear properties of the soil. For each of the profiles, the same unit weights, as well as shear modulus reduction and damping curves, were used. The Darendeli [2001] model was used to develop the modulus reduction and damping curves as a function of mean effective stress (σ'_m), Plasticity Index (PI), and over-consolidation ratio (OCR). In this study the PI and OCR are taken to be 10 and 1.0, respectively, for all layers. To model the stress dependence, the 150 m of soil was split into five layers, and the nonlinear property curves computed for the mean effective stress at the middle of each layer (σ'_m = 0.6, 1.4, 2.7, 5.0, and 8.0 atm).

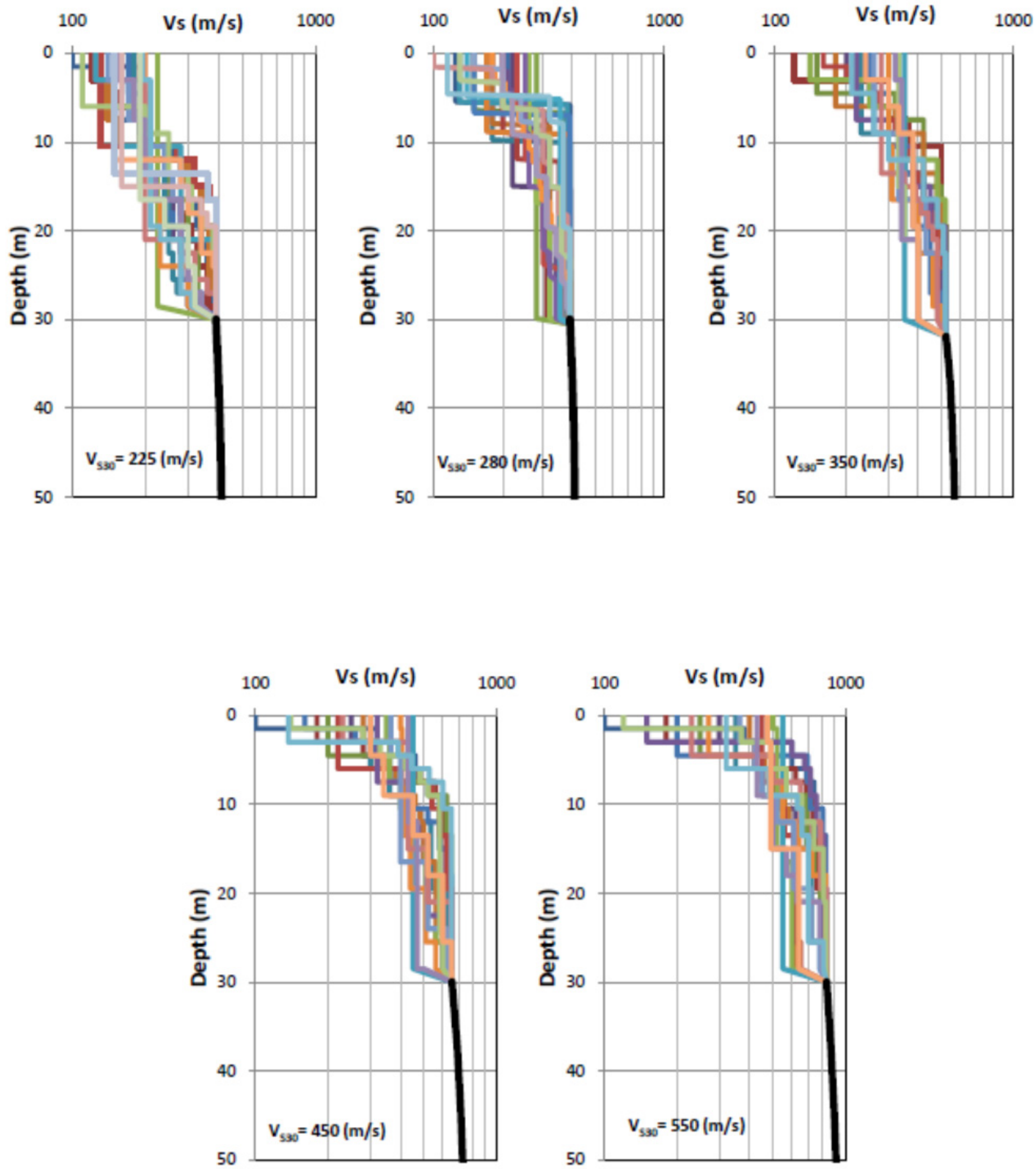

Figure 2.2 Generated velocity profiles for each V_{S30} value.

2.3 INPUT MOTIONS

The random vibration theory (RVT) approach to equivalent-linear site response analysis was used. The RVT method allows equivalent linear site response to be calculated without the need to specify an input time series. Rather, the RVT method specifies the Fourier amplitude spectrum (FAS) of the input motion and propagates the FAS through the soil column using frequency domain transfer functions. The program *Strata* can generate input FAS from a specified input response spectrum or through seismological theory. For this study, the input motion was specified by seismological theory using the single-corner frequency, ω^2 point source model

(Brune [1970]). See Boore [2003] for additional discussion on this model and its use in RVT predictions of ground shaking. To specify the input motion, the earthquake magnitude, site-to-source distance, and source depth is provided by user. The other seismological parameters in the model are taken from Campbell [2003] and represent typical values for the western U.S. region.

To consider the nonlinear behavior of the soil, analyses were performed at multiple input intensities. Earthquake magnitude and site-source distance were varied to obtain different input intensities from the seismological method. The corresponding magnitude, distance, and depth combinations used to generate the different input intensities are given in Table 2.1 along with the resulting PGA_{rock}. The range of magnitudes is between 6.5 and 7.8, while the range of distances, is 6 to 180 km. The resulting PGA_{rock} values are from 0.01*g* to 1.5*g* and the resulting rock response spectra are shown in Figure 2.3.

Table 2.1 Magnitude, distances, and PGA_{rock} for the RVT input motions.

Magnitude	Distance (km)	PGA_{rock} (*g*)
7.0	180	0.01*g*
7.0	68	0.05*g*
7.0	40	0.09*g*
6.5	20	0.16*g*
7.0	21	0.22*g*
7.0	16	0.3*g*
7.0	21	0.4*g*
7.0	10	0.5*g*
7.0	7	0.75*g*
7.6	9	0.9*g*
7.5	7	1.1*g*
7.8	6	1. *g*

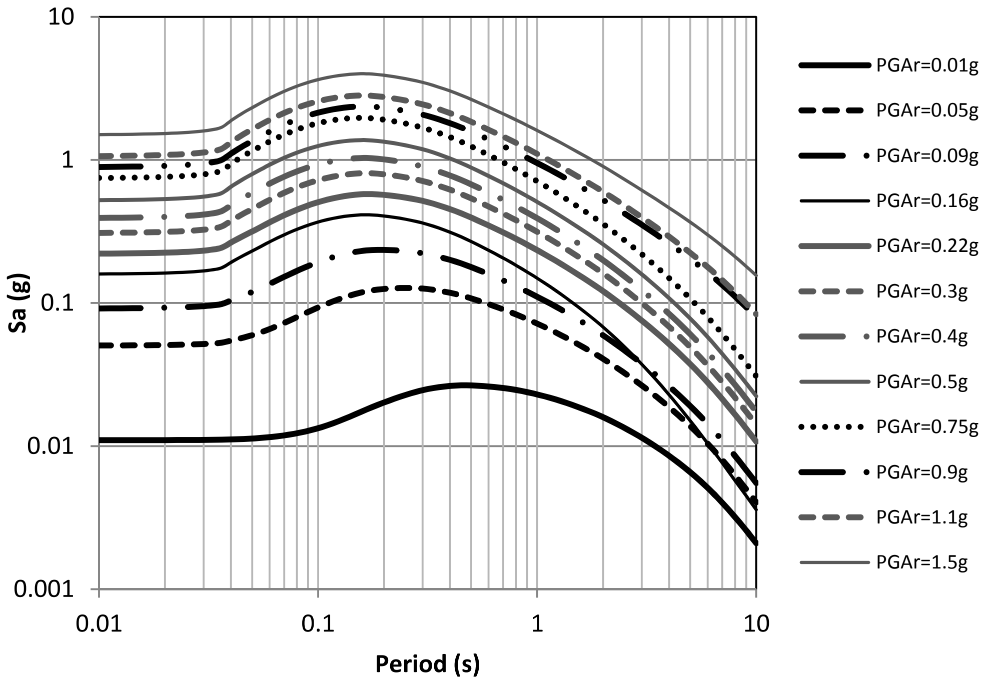

Figure 2.3 Response spectra for RVT input motions.

2.4 SITE CHARACTERISTICS

Identification of those spectral periods that are influenced by the seismic response of a site is critical. One simple parameter that can be used to consider the period range most affected by a site's response is the site period, T_S, which is the period corresponding to first mode and represents the entire V_S profile from the rock to the surface. The site period is estimated as:

$$T_s = \frac{4 \cdot H}{\overline{V}_s} \tag{2.1}$$

where H is the soil thickness, and $\overline{V}_s$ is the average shear wave velocity of the soil. $\overline{V}_s$ is computed from the travel time for a shear wave traveling through the entire soil profile. The V_S profiles developed for a given V_{S30} category, each having same V_{S30} and same V_S profile below 30 m, all have the same T_S. The values of T_S for the five V_{S30} values considered are listed in Table 2.2. T_S ranges from approximately 0.75 to 1.5 sec for the five V_{S30} profiles considered.

The detailed velocity structure in the top 30 m affects site amplification as well. To estimate the period range affected by the top 30 m, another site period corresponding to the top 30 m is defined and called T_{30}, which is computed as:

$$T_{30} = \frac{4 \cdot (30\ \mathrm{m})}{V_{s30}} \tag{2.2}$$

Table 2.2 presents T_{30} values for the five V_{S30} categories. T_{30} ranges from approximately 0.2 to 0.55 sec for the five V_{S30} profiles considered.

Because the period is inversely proportional to V_S, T_S and T_{30} decrease as V_{S30} increases; therefore, stiffer sites have shorter site periods and shorter periods are affected most by site amplification. The T_S for each category of V_{S30} is greater than its corresponding T_{30} because T_S is associated with the entire depth of the profile and T_{30} with only the top 30m.

To further investigate the period range in which the detailed velocity structure in the top 30 m affects the response, one-dimensional (1D) frequency domain transfer functions were computed for different profiles. A transfer function describes the ratio of the FAS of acceleration at any two points in the soil column. Figure 2.4 plots the acceleration transfer functions between the surface and the bedrock outcrop for three selected velocity profiles in the V_{S30} = 225 and 450 m/sec categories. In calculating these transfer functions, the soil properties were assumed to be linear elastic. The transfer functions are plotted versus period in Figure 2.4 and the corresponding periods for T_{30} and T_S are indicated. For periods near T_S, the transfer functions of different profiles in the same V_{S30} category are very similar because the transfer function in this period range is controlled by the full V_S profile. Starting at periods around T_{30} and at periods shorter than $T_{30,}$ the transfer functions vary significantly between the different profiles even though they have the same V_{S30}. This variability in the transfer function illustrates the influence of the details of the top 30 m V_S profile in this period range. It can be concluded that the details of the top 30 m of a site are important at periods shorter than T_{30}. As a result, the period range influenced by the top 30 m depends on V_{S30} (since T_{30} is V_{S30} dependent). Because the transfer functions in Figure 2.4 are for linear-elastic conditions, an additional consideration will be the influence of input intensity and soil nonlinearity. As the input intensity increases the soil becomes more nonlinear, and both T_S and T_{30} will shift to long periods. As a result, the period range affected by the top 30 m will increase to longer periods as input intensity increases.

Table 2.2 T_S and T_{30} values for each V_{S30}.

V_{S30} (m/sec)	T_S (sec)	T_{30} (sec)
225	1.54	0.53
280	1.45	0.43
350	1.10	0.34
450	0.87	0.27
550	0.72	0.22

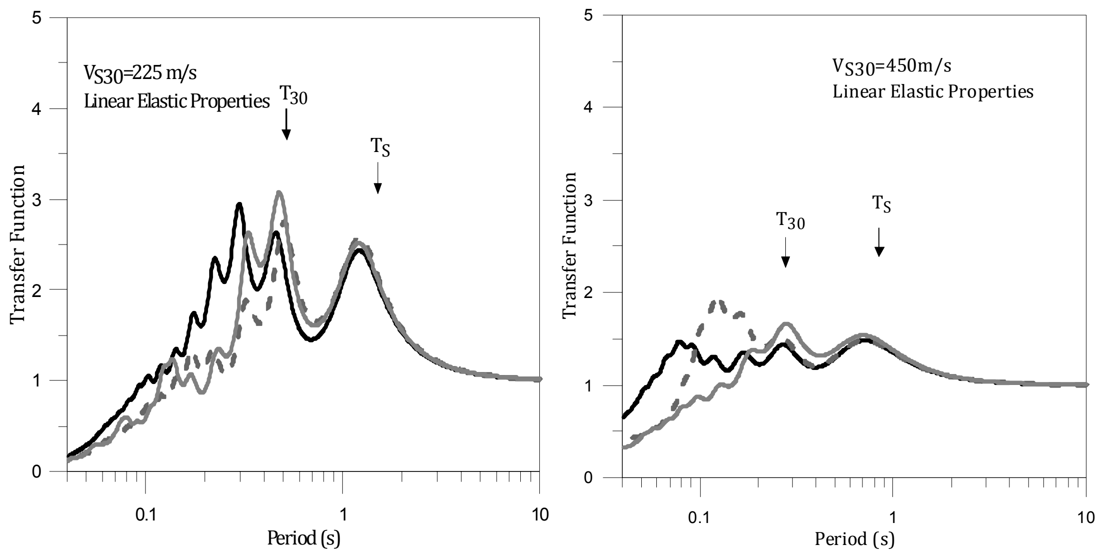

Figure 2.4 Linear-elastic transfer functions for select velocity profiles with $V_{S30.}$=.225 and 450 m/sec.

All the generated profiles in each category of V_{S30} had the same value of V_{S30} but a different V_S structure in the top 30 m. Several parameters were identified from the velocity profiles as candidates that affect the computed site amplification. These parameters are V_{min}, thV_{min}, depthV_{min}, MAXIR, and V_{ratio}. These parameters are defined as:

- V_{min} is the minimum shear wave velocity in the V_S profile
- thV_{min} is the thickness of the layer with the minimum shear wave velocity
- depthV_{min} is the depth to the top of the layer with V_{min}
- MAXIR is the maximum impedance ratio within the V_S profile as defined by the ratio of the V_S of two adjacent layers ($V_{s,upper}$ / $V_{s,lower}$)
- V_{ratio} is the ratio of the average shear wave velocity ($\overline{V}_s$) between 20 m and 30 m to the average shear wave velocity in top 10 m. V_{ratio} is defined as:
-

$$V_{ratio} = \frac{V_{S(20-30)}}{V_{S10}} \tag{2.3}$$

$$V_{S(20-30)} = \frac{10\text{ m}}{\Sigma\left(\frac{h_i}{V_{S,i}}\right)} \quad \text{over depths 20 to 30 m} \tag{2.4}$$

$$V_{S10} = \frac{10\text{ m}}{\Sigma\left(\frac{h_i}{V_{S,i}}\right)} \quad \text{over depths 0 to 10 m} \tag{2.5}$$

The concept of V_{ratio} is similar to the impedance ratio for MAXIR, except that it represents a more global impedance ratio in the top 30 m. It also has the advantage of using information from a significant portion of the top 30 m of a profile, and it indicates how much the shear wave velocity increases in top 30 m. V_{ratio} can also indicate if a large scale velocity inversion occurs in the top 30 m when it takes on values less than 1.0.

2.5 INFLUENCE OF SITE CHARACTERISTICS ON SITE AMPLIFICATION

2.5.1 Low Input Intensities

If V_{S30} and $Z_{1.0}$ are the dominant factors in explaining site amplification, sites with the same V_{S30} and $Z_{1.0}$ should have the very similar AFs. Figure 2.5 plots AF versus period for all of the generated sites for each of the V_{S30} categories subjected to the lowest input intensity (PGA_{rock} = 0.01*g*). The amplification factors for a given V_{S30} are not constant and in some instances show significant scatter. The amount of scatter (i.e., variability) varies with V_{S30} and period. At smaller V_{S30}, the variability in the AFs is more significant. The period range over which the variability in AF is most significant also depends on V_{S30}. As V_{S30} increases, this period range decreases. At periods greater than T_{30}, less variability is observed. The period at which the maximum variability in the AF occurs is also V_{S30} dependent. For V_{S30} = 225 m/sec, the maximum variability is observed at a spectral period of 0.3 sec. Stiffer sites (V_{S30} = 280 m/sec and 350 m/sec) display the maximum variability at a spectral period of 0.2 sec, and the stiffest sites (V_{S30} = 450 m/sec and 550 m/sec) display the maximum variability at a spectral period of 0.1 sec.

To quantify the variability in AF, the standard deviation of ln(AF) at each period for each category of V_{S30} was calculated. The standard deviation (σ_{lnAF}) is calculated for the ln(AF) because ground motions are commonly assumed to be log-normally distributed and to be consistent with its use in GMPEs. Figure 2.6 shows the σ_{lnAF} values computed from the data in Figure 2.5. σ_{lnAF} smaller than about 0.05 is considered small enough such that the variability is minimal. The data in Figure 2.6 show that σ_{lnAF} is greater than 0.05 at periods less than about T_{30} for each V_{S30}, which is consistent with the observations from the transfer functions. Additionally, the values of σ_{lnAF} are V_{S30} dependent, with sites with smaller V_{S30} producing larger values of σ_{lnAF}.

The identification of the site parameters that explain the variability in AF is initiated by relating the data in Figure 2.5 to various site parameters. The data in Figure 2.5 were used to compute the difference between each ln(AF) and the average ln(AF) for a given period, input intensity, and V_{S30} is considered. This difference represents the residual and is defined as:

$$\mathrm{Residual} = \ln(\mathrm{AF}) - \mu_{\ln\mathrm{AF}} \tag{2.6}$$

where ln(AF) represents the AF for a single V_S profile with a given V_{S30}, and μ_{lnAF} is the average ln(AF) for all sites with the same V_{S30}. Considering the periods that have larger σ_{lnAF} values, only periods of 0.1 sec, 0.2 sec, and 0.3 sec will be considered here.

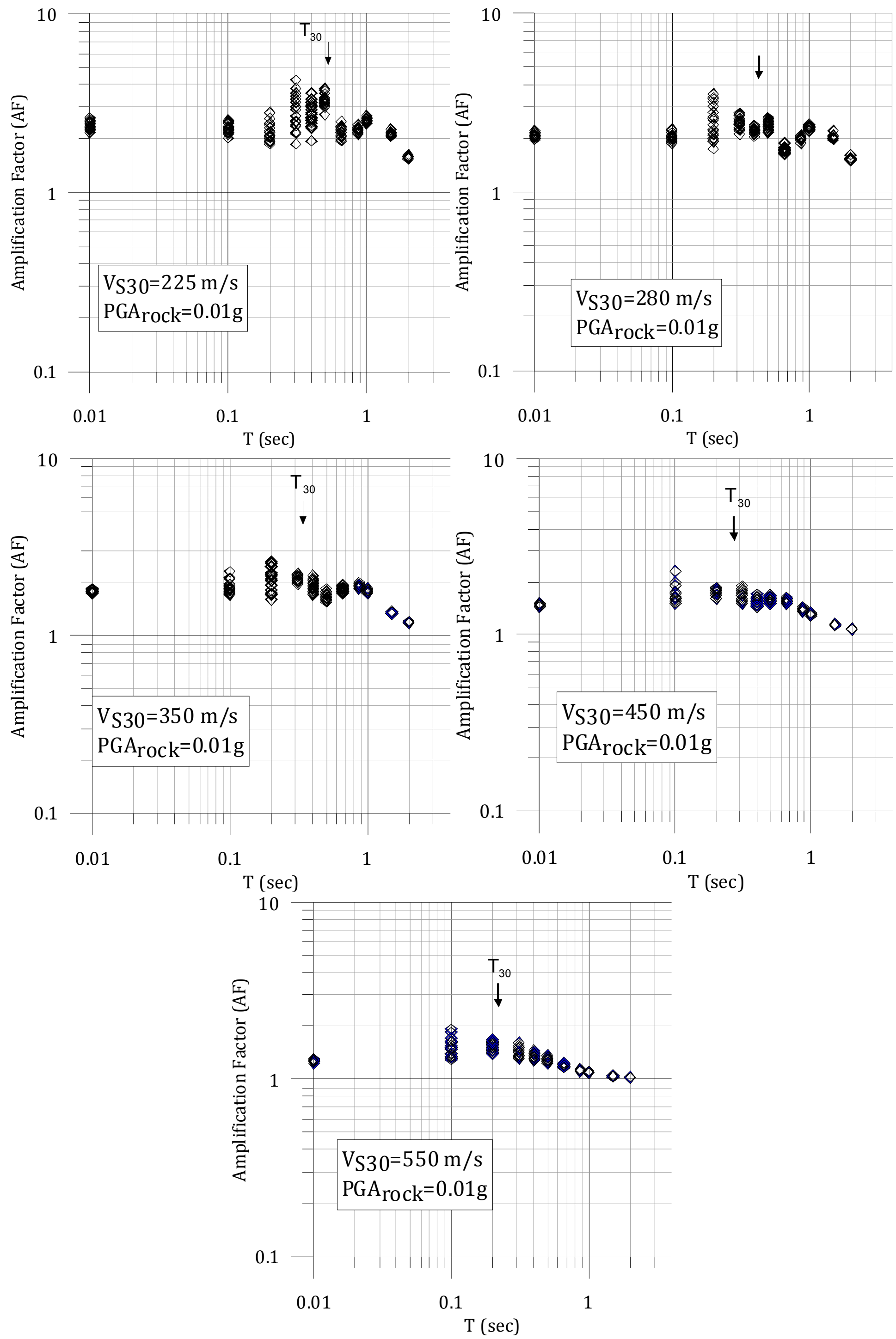

Figure 2.5 Amplification factor versus period for all generated profiles, PGA_{rock} = 0.01*g*.

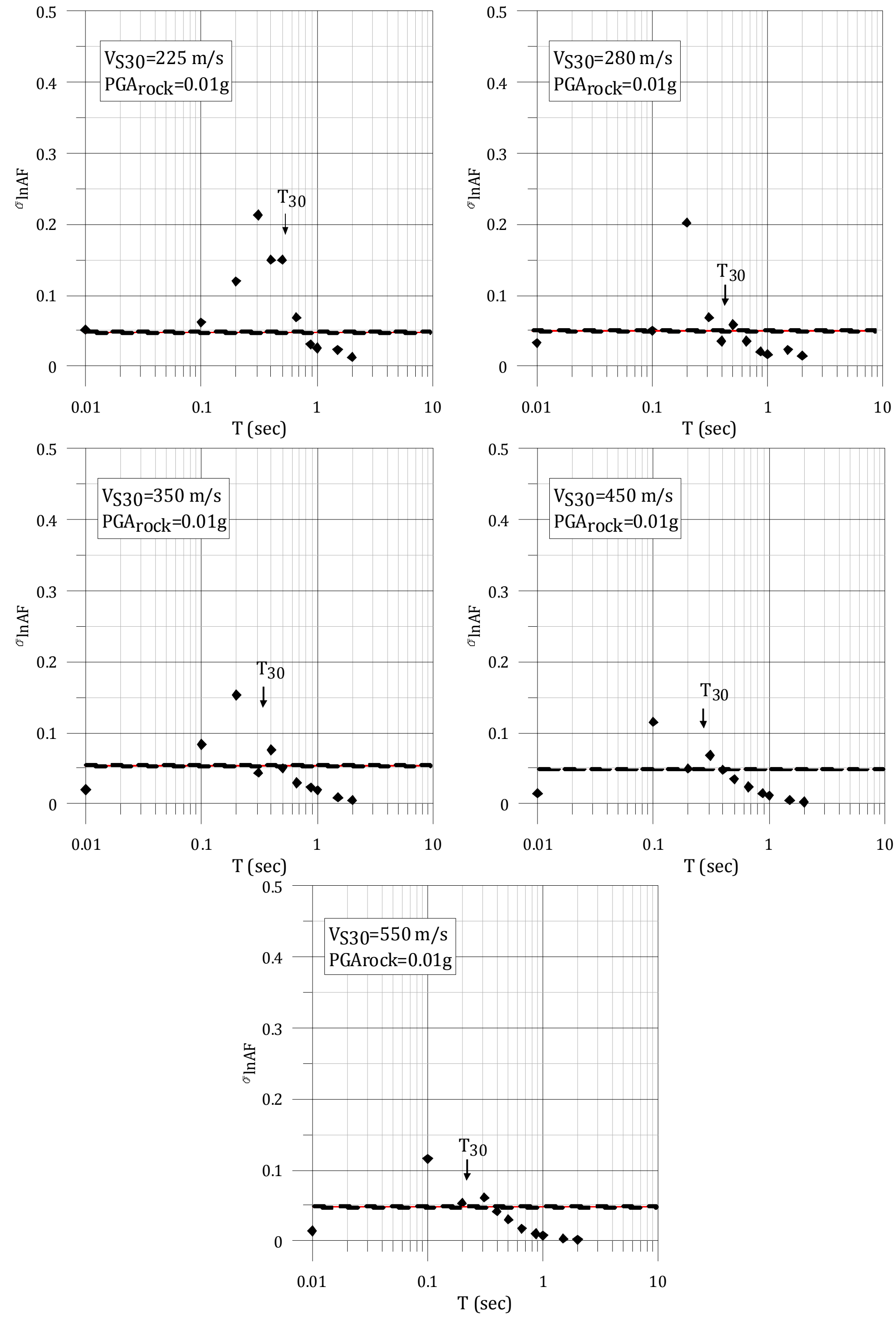

Figure 2.6 **σ_{lnAF} versus period for all generated profiles, PGA_{rock} = 0.01*g*.**

The residual measures the difference between a specific value of AF and the average value of AF for all sites with the same V_{S30} for a given period and input intensity. If a relationship is observed between the calculated residuals and a site parameter, then that parameter influences site amplification and potentially should be included in predictive models for AF to reduce its variability. As mentioned previously, the minimum velocity in the profile (V_{min}), the thickness of the layer with the minimum velocity (thV_{min}), the depth to the layer with the minimum velocity ($depthV_{min}$), the maximum impedance ratio (MAXIR), and V_{ratio} are the site characteristics considered.

The first candidate parameter is V_{min}. While the absolute value of V_{min} is important, its value relative to V_{S30} provides information about the range of velocities within the top 30 m. To consider the relative effect of V_{min}, residuals were plotted versus V_{S30}/V_{min} instead of V_{min}. The minimum value of V_{S30}/V_{min} is 1.0, which represents a site with constant velocity equal to V_{S30} in the top 30 m. Larger values of V_{S30}/V_{min} indicate smaller values of V_{min}. Figure 2.7 shows the residuals versus V_{S30}/V_{min} for all V_{S30} categories at a spectral period of 0.2 sec and PGA_{rock} = 0.01*g*. For $V_{S30} \leq 350$ m/sec the residuals generally increase with increasing V_{S30}/V_{min}, while there is little influence of V_{S30}/V_{min} on the residuals for V_{S30} = 450 and 550 m/sec. That said, as shown in Figure 2.6, there is little variability in AF for sites with V_{S30} = 450 and 550 m/sec at this period ($\sigma_{lnAF} \sim 0.05$).

Other parameters that may influence AF are thV_{min}, MAXIR, $depthV_{min}$, and V_{ratio}. In all the generated profiles in this study, the minimum velocity occurs at the ground surface, such that all profiles have $depthV_{min}$ equal to zero. Thus, this parameter cannot be considered with the present dataset. The residuals versus thV_{min}, MAXIR, and V_{ratio} for a spectral period of 0.2 sec and PGA_{rock} = 0.01*g* are plotted in Figures 2.8, 2.9, and 2.10, respectively. The relationship between the residuals and thV_{min} is quite weak (Figure 2.8). The relationship between the residuals and MAXIR (Figure 2.9) is stronger, particularly for V_{S30} = 280 m/sec and 350 m/sec, but the relationship is weak for V_{S30} = 225 m/sec. The relationship between the residuals and V_{ratio} (Figure 2.10) is very strong for V_{S30} = 280 m/sec and 350 m/sec, and moderately strong for V_{S30} = 225 m/sec.

Evaluating the relationship between the residuals and the four parameters, V_{ratio} best explains the variability in the AF at T = 0.2 sec as the relationship between that residual and V_{ratio} is stronger than the three other parameters. Generally a linear relationship between the residual and $\ln(V_{ratio})$ is observed. Consider σ_{lnAF} in Figure 2.6: the variability in AF is significant for periods of 0.1 sec, 0.2 sec, and 0.3 sec for most of the V_{S30} values. Residuals plotted for these periods also show a strong linear relationship between the residuals and $\ln(V_{ratio})$; however, the intercept and slope of the linear fit is V_{S30} and period dependent [Navidi 2012].

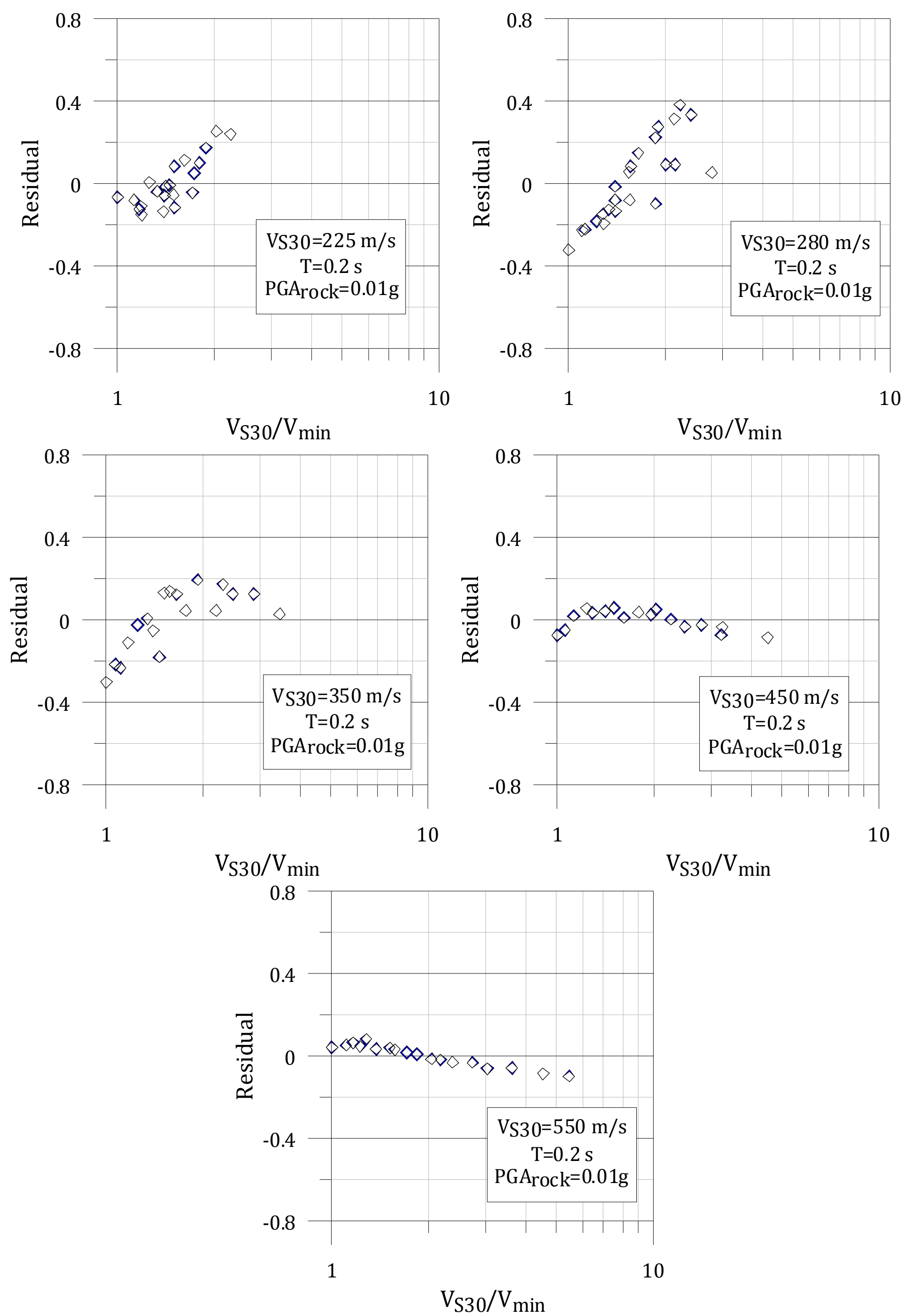

Figure 2.7 **Residual versus V_{S30}/V_{min} for spectral period of 0.2 sec and PGA_{rock} = 0.01*g*.**

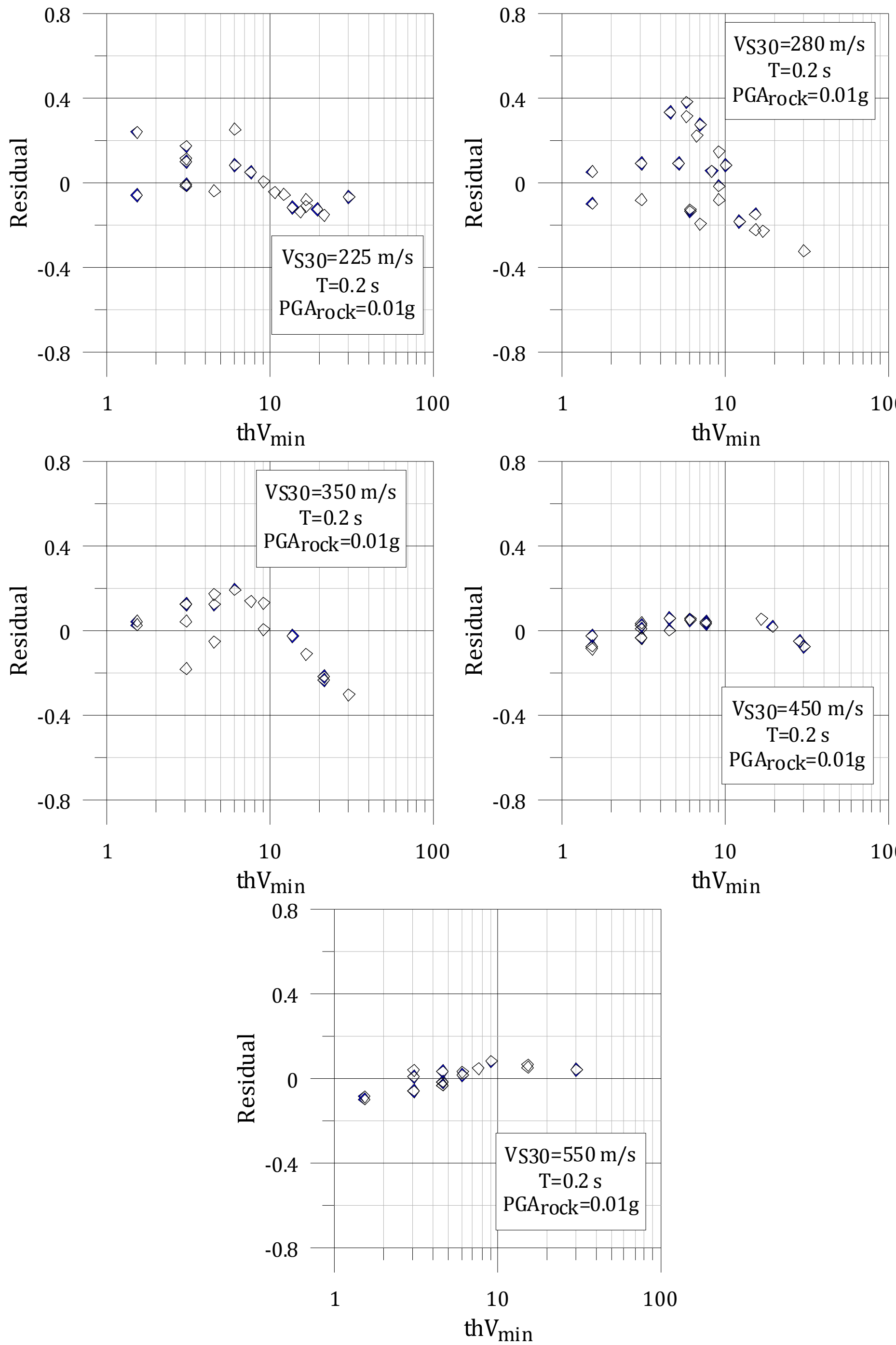

Figure 2.8 **Residual versus thV_{min} for spectral period of 0.2 sec and PGA_{rock} = 0.01*g*.**

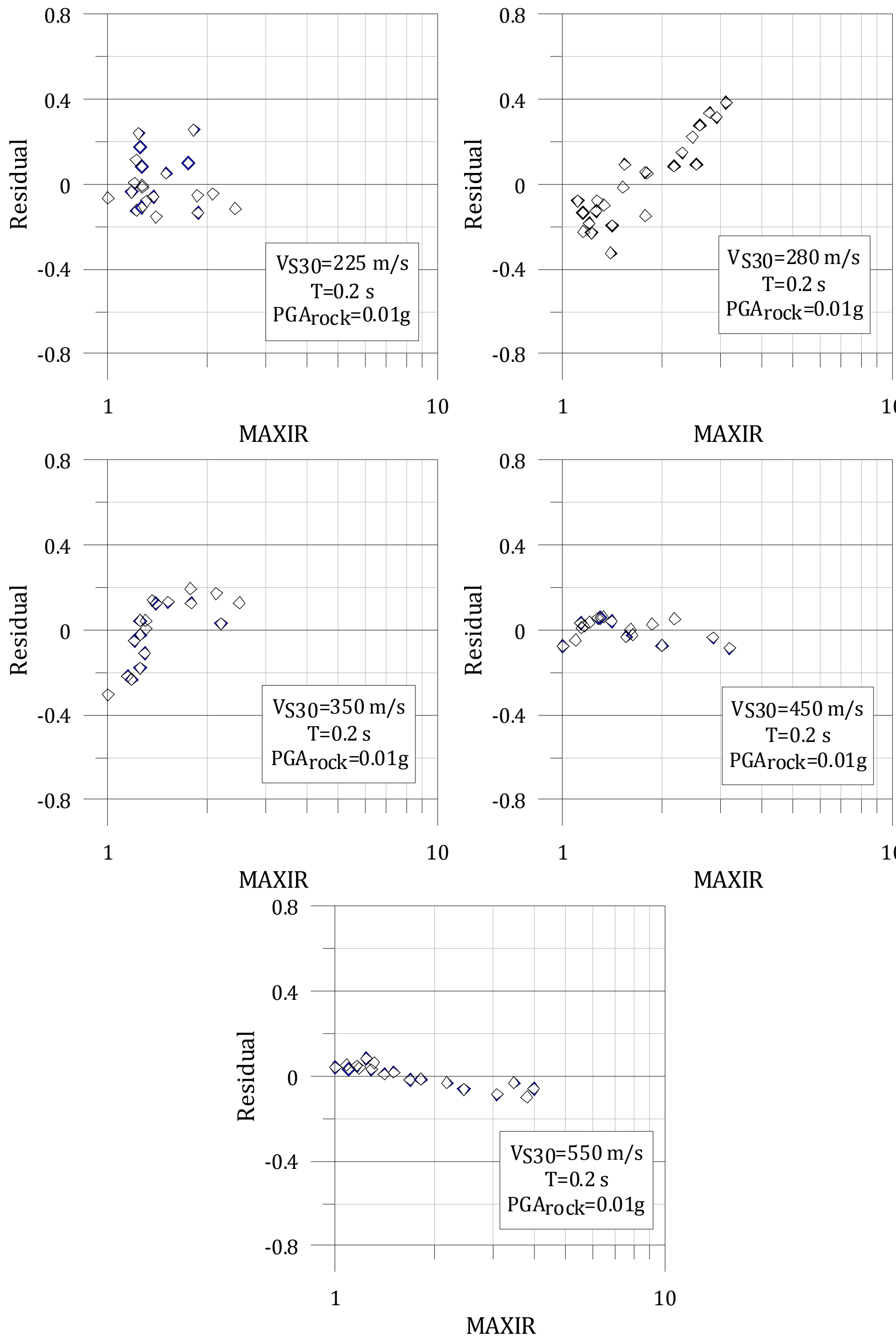

Figure 2.9 **Residual versus MAXIR for spectral period of 0.2 sec and PGA_{rock} = 0.01*g*.**

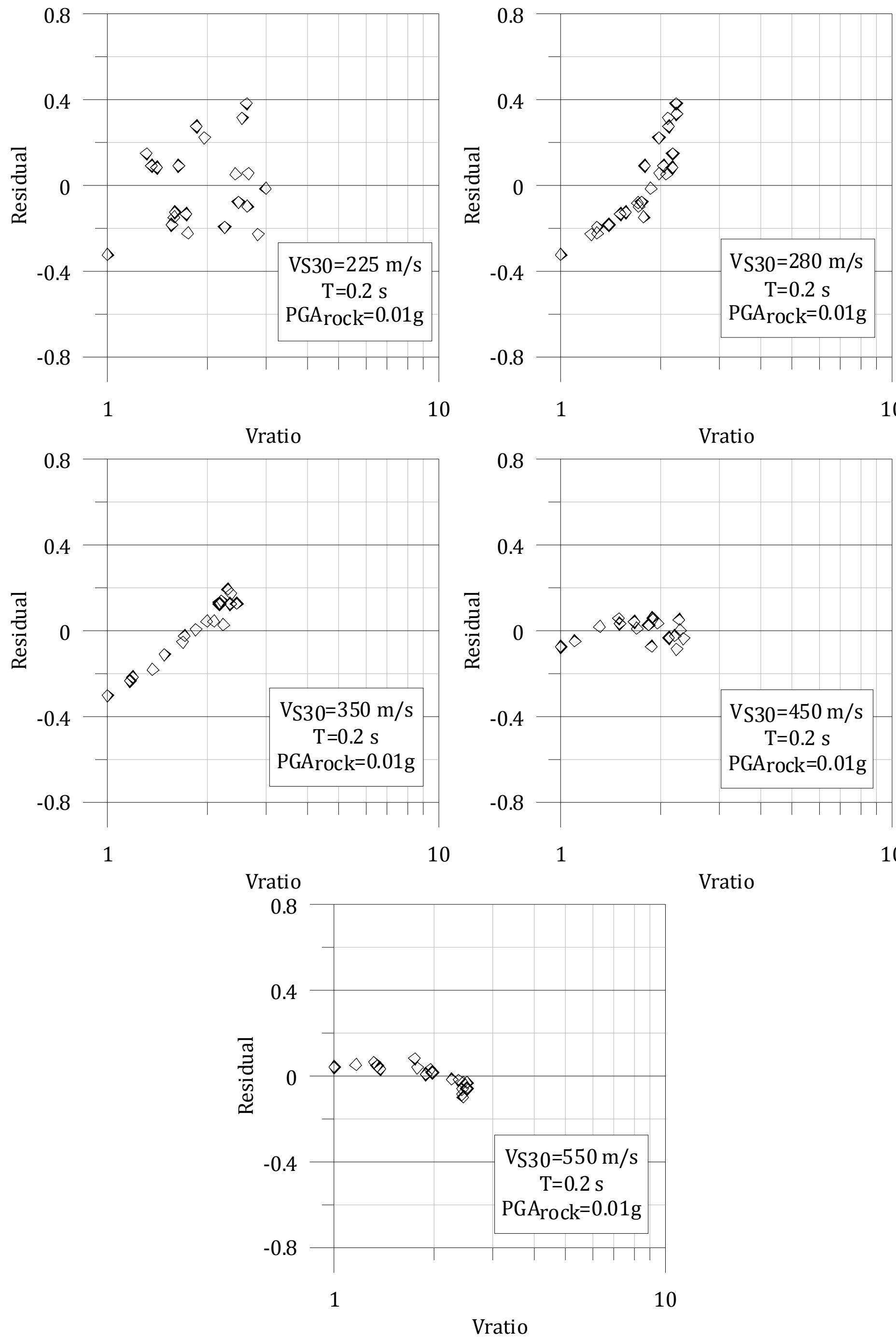

Figure 2.10 Residual versus V_{ratio} for a spectral period of 0.2 sec and PGA_{rock} = 0.01*g*.

2.5.2 Larger Input Intensities

Soil layers show nonlinear behavior at larger input intensities because larger strains are induced that soften the soil and increase the material damping. Therefore, amplification becomes a nonlinear function of input intensity at higher shaking levels. To investigate the variability in AF at moderate intensities, the results for $PGA_{rock} = 0.3g$ are presented.

In Figure 2.11, AF versus period is shown for all the generated sites at $PGA_{rock} = 0.3g$. Comparing the AFs at each spectral period in Figure 2.11 with those in Figure 2.6 for $PGA_{rock} = 0.0g$, it is clear that there is an increase in amplification variability. Figure 2.12 shows σ_{lnAF} versus period for each V_{S30} category for the AF results shown in Figure 2.11. The largest values of σ_{lnAF} are observed at $V_{S30} = 225$ m/sec. All the periods in this category of V_{S30} have significant variation in AF (i.e., $\sigma_{lnAF} > 0.05$). σ_{lnAF} is as large as 0.4 at T = 0.66 sec for this value of V_{S30}. For all sites with $V_{S30} \leq 350$ m/sec, σ_{lnAF} is significant at almost all periods considered ($\leq$ 2.0 sec). The maximum value of σ_{lnAF} occurs at longer periods as V_{S30} decreases. Comparing each V_{S30} category subjected to $PGA_{rock} = 0.3g$ to their corresponding profiles subjected to $PGA_{rock} = 0.01g$, the period range with σ_{lnAF} greater than 0.05 increases. The maximum σ_{lnAF} occurs generally at longer periods for $PGA_{rock} = 0.3g$ than for $PGA_{rock} = 0.01g$. These observations indicate that the period range that is affected by the detailed velocity structure in the top 30 m increases as the shaking level increases.

Considering the periods of maximum σ_{lnAF} in Figure 2.12, the residuals are investigated at periods of 0.2 sec (period of maximum σ_{lnAF} for $V_{S30} = 280$ and 450 m/sec) and a period of 0.66 sec (period of maximum σ_{lnAF} for $V_{S30} = 225$ m/sec).

Figure 2.13 plots the residuals for the AF results for $PGA_{rock} = 0.3g$ at a spectral period of 0.2 sec versus V_{ratio} in. Generally, a linear trend between the residuals and $\ln(V_{ratio})$ is observed, similar to the results for $PGA_{rock} = 0.01g$; however, the relationship appears to break down at small V_{S30} (i.e., 225 and 280 m/sec) and larger V_{ratio} (i.e., 2 to 3). Figure 2.14 plots the velocity profiles over the top 30 m for four sites with $V_{S30} = 225$ m/sec and with V_{ratio} around 2.5 but very high residuals (+0.4) and very low residuals (–0.4). The profiles with very low residuals have a thick soft layer (i.e., layer with $V_S \leq 160$ m/sec and thickness > 10 m) with a large impedance ratio (i.e., MAXIR) immediately below. The MAXIR is well above 2.0 for these profiles, while the profiles with large residuals have a MAXIR of between 1.5 and 1.7. The induced shear strains for the four profiles are also shown in Figure 2.14. The large MAXIR leads to significant shear strains—in excess of 2%—in the layers above the depth of MAXIR. The rapid increase in strain across the impedance contrast induces a rapid change in stiffness and damping that reduces the amplification at high frequencies. While the sites with large residuals also experience large strains (~ 1 to 1.5%), the increase in strain with depth is not as rapid, allowing for more wave motion to travel through the soil. The data in Figures 2.13 and 2.14 indicate that sites with very large MAXIR may experience very large strains at moderate input motion intensities, leading to smaller amplification.

The maximum value of σ_{lnAF} for $V_{S30} = 225$ m/sec occurs at T = 0.66 sec, while the value of σ_{lnAF} is also significant at a spectral period of 0.66 sec for $V_{S30} = 280$ m/sec (Figure 2.12). Figure 2.15 shows the residuals versus V_{ratio} for all the generated sites subjected to $PGA_{rock} =$

0.3g at spectral period of 0.66 sec. For $V_{S30} \geq 350$ m/sec, the residuals are almost zero because σ_{lnAF} is less than 0.05 (Figure 2.12). A linear trend is generally observed between the residuals and ln(V_{ratio}) for the softer profiles ($V_{S30} = 225$ and 280 m/sec); however, the data is scattered for $V_{S30} = 225$ m/sec and V_{ratio} greater than about 2.3. These are the same sites discussed in Figure 2.14, and the scatter is due to the large MAXIR and thick soft layers in the profiles. Generally at all periods where the variability in amplification is significant (i.e., $\sigma_{lnAF} > 0.05$), the calculated residuals for these AF have a linear trend with ln(V_{ratio}). That said, there are some profiles that break down this trend. These profiles tend to have a thick, very soft layer near the surface that may be unrealistic.

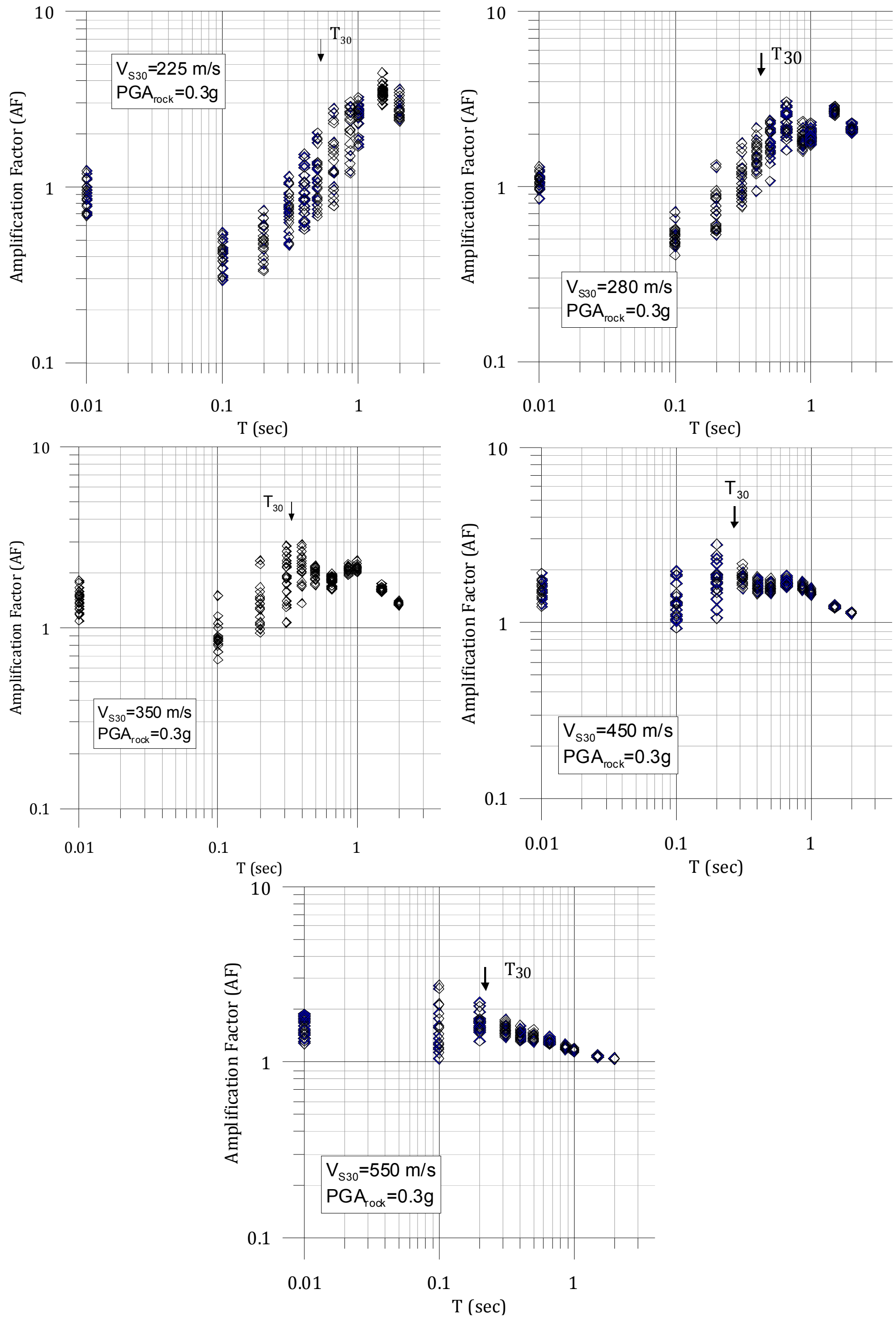

Figure 2.11 Amplification factor versus period for all generated profiles, PGA_{rock} = 0.3*g*.

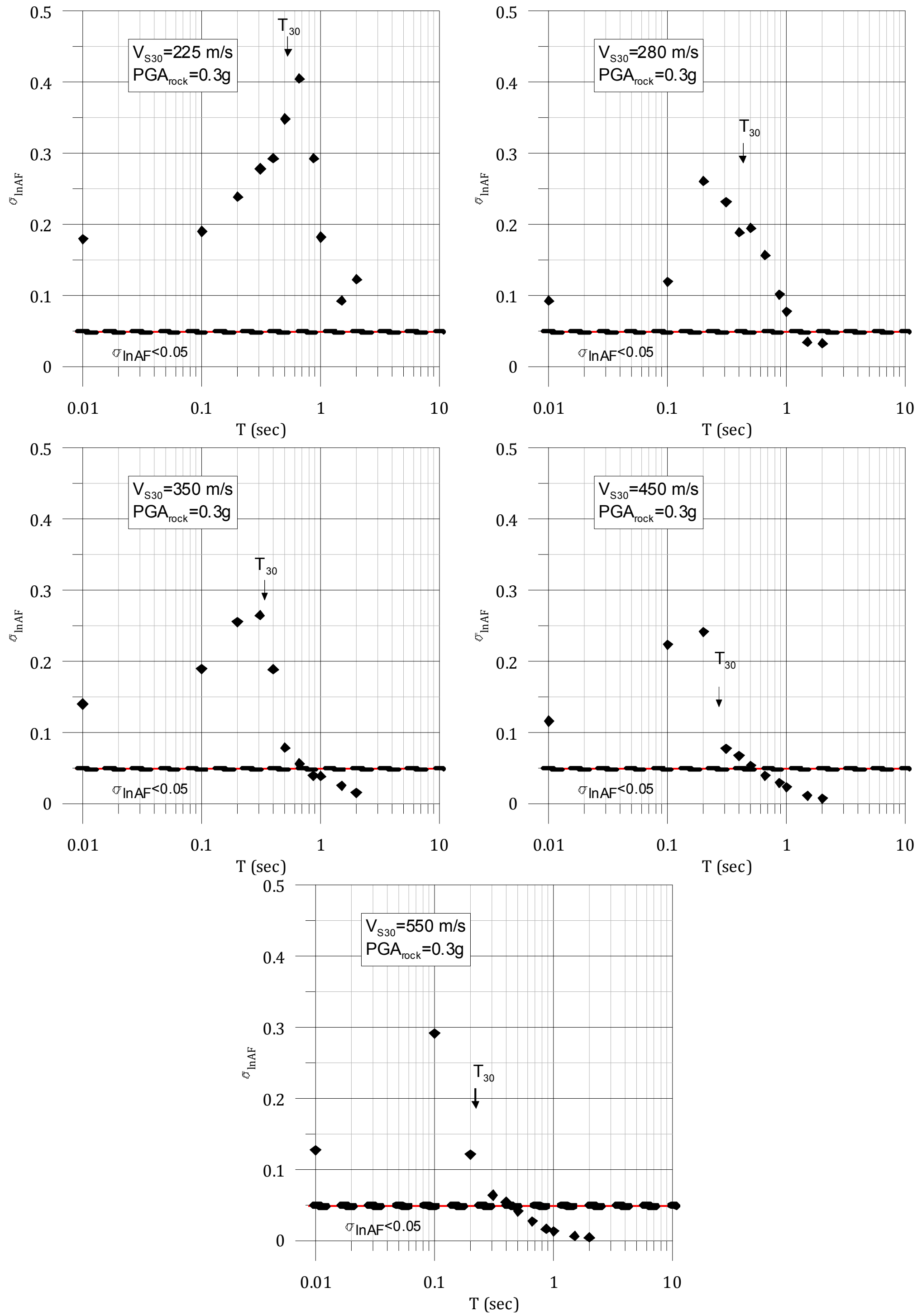

Figure 2.12 $\sigma_{\ln AF}$ **versus period for all generated profiles, PGA$_{rock}$ = 0.3*g*.**

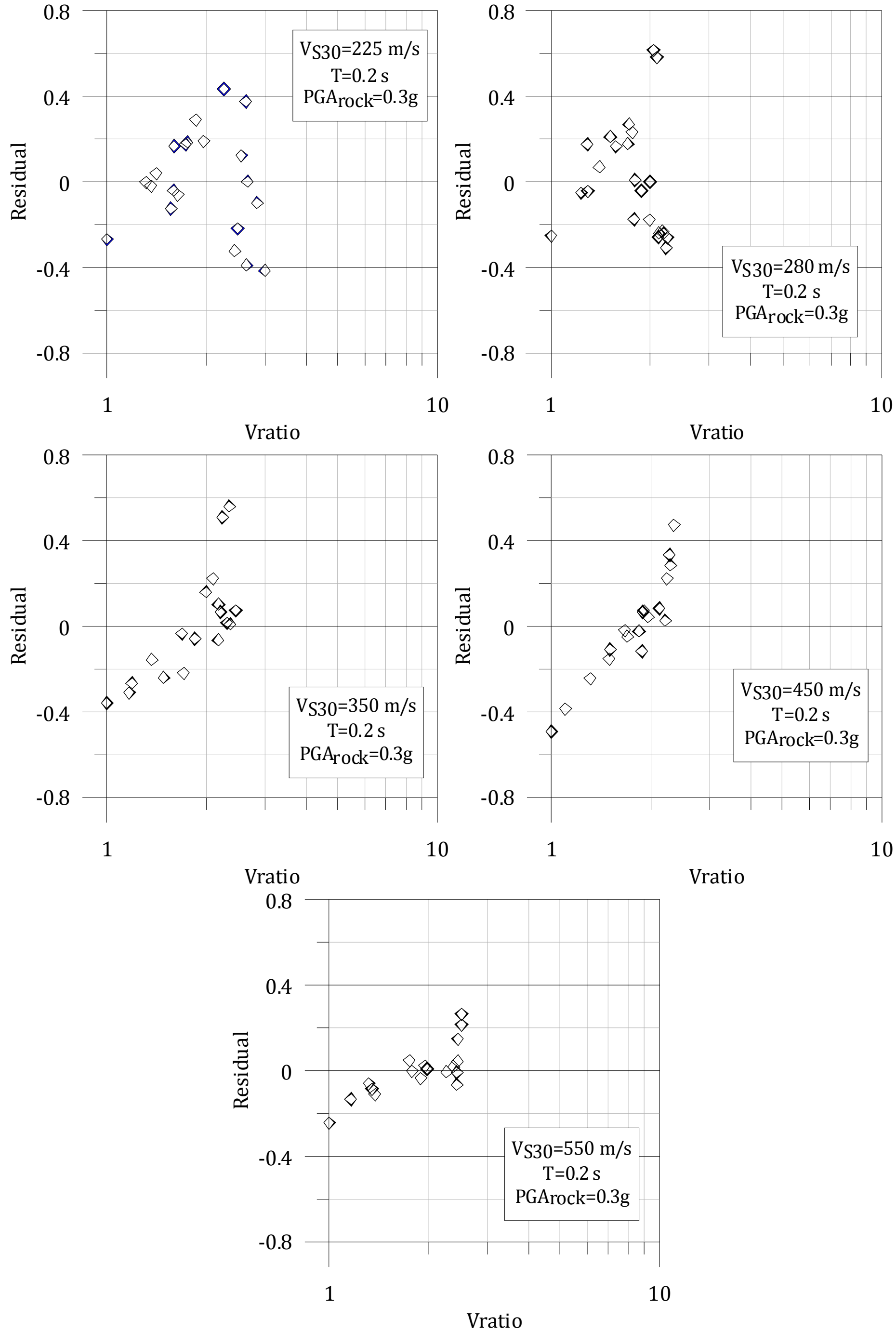

Figure 2.13 Residual versus V_{ratio} for spectral period of 0.2 s and PGA_{rock} = 0.3*g*.

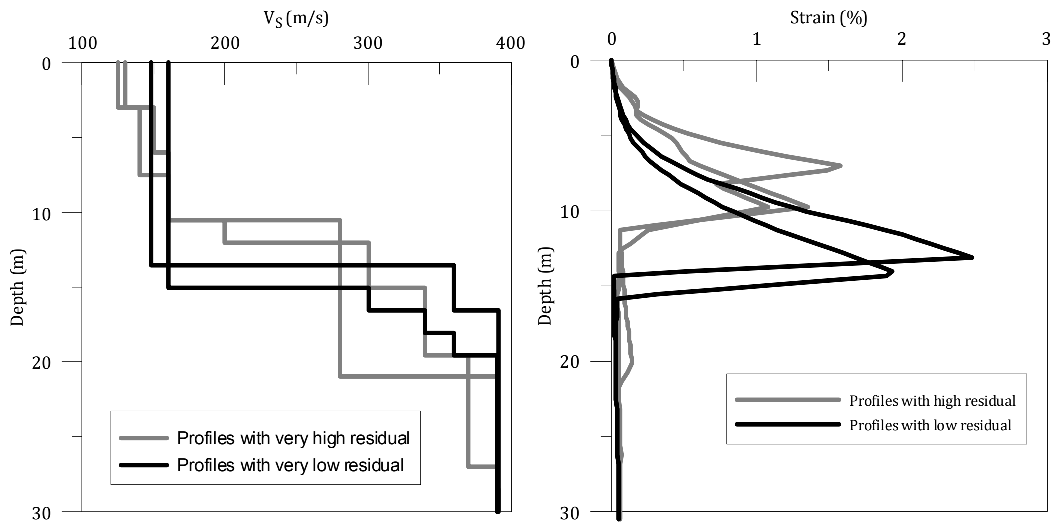

Figure 2.14 V_S profiles and induced shear strains for sites with V_{ratio} ~ 2.5.

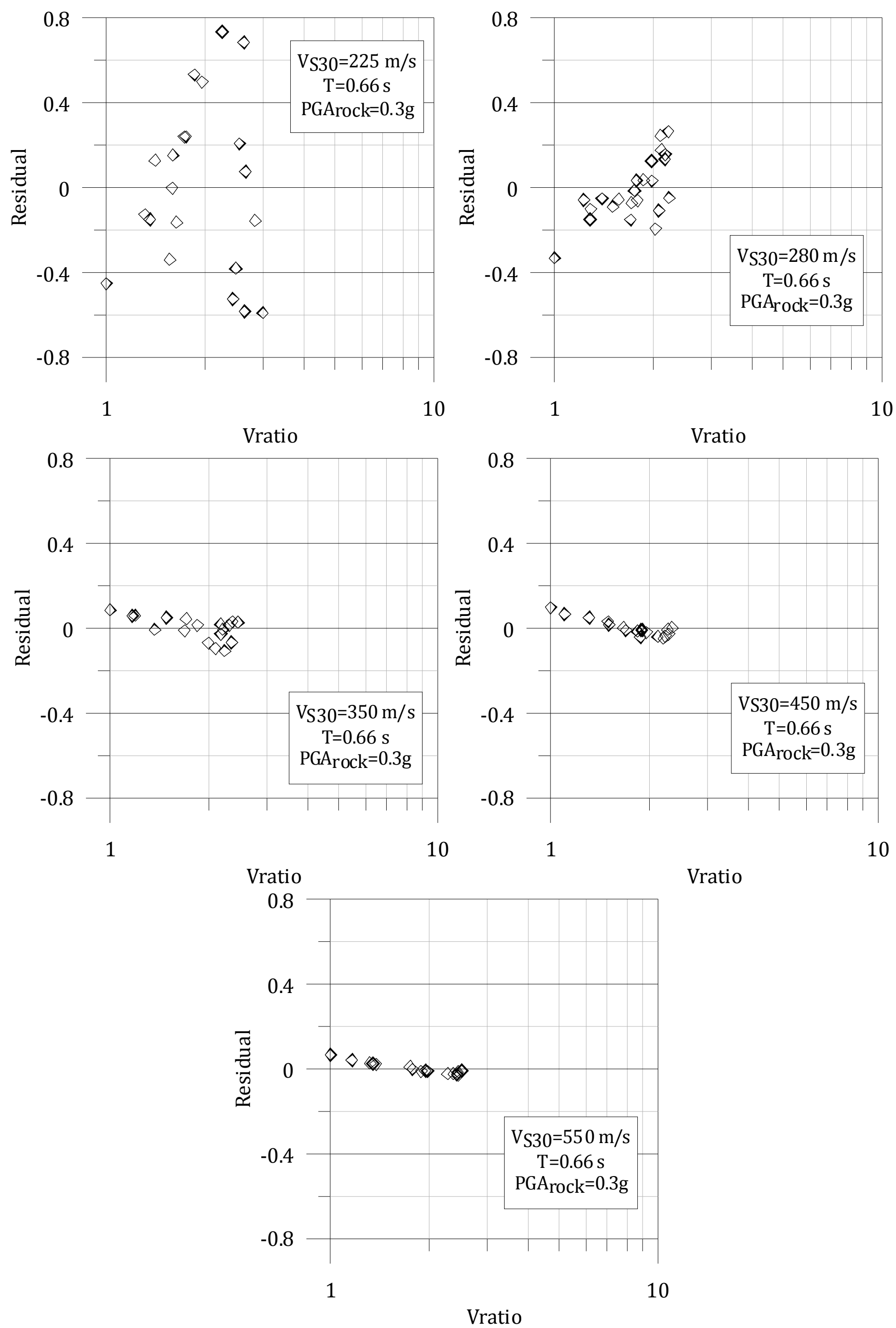

Figure 2.15 Residual versus V_{ratio} for spectral period of 0.66 s and PGA_{rock} = 0.3*g*.

2.6 SUMMARY

To investigate the site parameters beyond V_{s30} that influence site amplification, 99 profiles were manually generated using five baseline profiles. The generated profiles from each baseline profile had the same average shear wave velocity in top 30 m, the same velocity structure at depths greater than 30 m, and the same depth to bedrock. Equivalent-linear site response analyses were performed and the site AFs computed for the profiles were studied.

At multiple input intensities, sites with the same average shear wave velocity and depth to rock but a different structure in the V_S profile in the top 30 m display different AFs at some periods. These periods are correlated to T_{30}. The variability in the AFs at these periods indicates that the detailed velocity structure in the top 30 m of a V_S profile influences the computed AF. As input intensity increased, the period range affected by the top 30 m increased.

The parameters V_{min}, thV_{min}, depthV_{min}, MAXIR, and V_{ratio} were considered to explain the variability in AFs. The parameter V_{ratio} was identified as the parameter that most strongly influenced the computed amplification. A linear relationship was observed between residuals and $\ln(V_{ratio})$. Residuals versus $\ln(V_{ratio})$ plots for different V_{S30} and at different periods show that the effect of V_{ratio} on amplification is V_{S30} and period dependent.

3 Approach to Development of Site Amplification Model

3.1 INTRODUCTION

To develop a site amplification model that includes the effects V_{ratio}, the seismic response of sites with a wide range of velocity profiles is assessed and the computed AFs used in the statistical analysis. Hypothetical velocity profiles are developed using Monte Carlo simulations in which soil layer thickness, shear wave velocity, and depth to the bedrock are statistically varied. This chapter describes the generation of the velocity profiles and the statistical analyses to be performed, while the next chapters describe the development of the site amplification model.

3.2 STATISTICAL GENERATION OF VELOCITY PROFILES

A soil profile consists of discrete layers that describe the variation of soil properties with depth. Seismic site response analysis characterizes each soil layer by a thickness, mass density, shear wave velocity, and nonlinear properties (i.e., G/G_{max} versus shear strain, and D versus shear strain).

The site response program *Strata* [Kottke and Rathje 2008] uses Monte Carlo simulations to develop different potential realizations of site properties. The goal of a Monte Carlo simulation is to estimate the statistical properties of the response of a complex system. To achieve this goal, each of the properties of the system is selected from defined statistical distributions, and the response of the system is computed. The calculated response from each realization is then used to estimate the statistical properties of the system's response. Monte Carlo simulations require that each of the components in the system has a complete statistical description.

The Monte Carlo randomization feature in *Strata* can randomize layer thickness, shear wave velocity of a layer, nonlinear soil properties of a layer, and depth to bedrock. In this study layer thicknesses, shear wave velocity, and depth to bedrock were randomized; but nonlinear properties were not. *Strata* uses the statistical models developed by Toro [1995] to randomize the layer thicknesses and associated shear wave velocities. In this approach, layer thicknesses are first generated and then shear wave velocities are assigned to each layer.

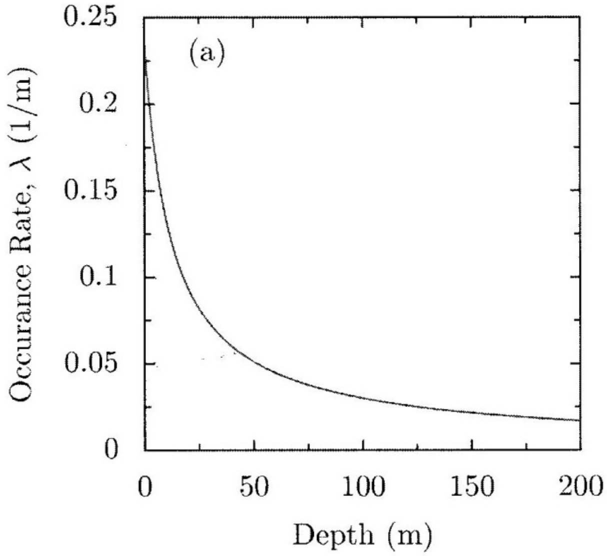

Figure 3.1 Variation of layer interface occurrence rate with depth [Toro 1995].

Layering is modeled as a Poisson process, which is a stochastic process with the event occurring at a given rate (λ). For a homogeneous Poisson process this rate is constant, while for a non-homogeneous Poisson process the rate of occurrence varies. For the layering problem, the event is a layer interface, and its rate is defined in terms of the number of layer interfaces per meter. The rate of interface occurrence is depth dependent (i.e., thinner layers tend to occur near the surface, while thicker layers tend to occur at depth), thus a non-homogeneous Poisson process is used. Toro [1995] developed a depth-dependent layering rate model using the layer thicknesses measured at 557 sites, mostly from California. The resulting model of depth-dependent layering rate is shown in Figure 3.1. Note that the rate varies from 0.22 1/m at the ground surface (i.e., average layer thickness = $1/\lambda$ = 4.5 m) to 0.05 1/m at a depth 50 m (i.e., average layer thickness = 20 m) to 0.02 1/m at a depth of 200 m (i.e., average layer thickness = 50 m).

After developing the layering profile (i.e., layer thicknesses) using the non-homogeneous Poisson process, a shear wave velocity is assigned to each layer. The Toro [1995] model describes the shear wave velocity at mid-depth of the layer by the log-normal distribution, and the use of this distribution is based on statistical investigation of shear wave velocity data from the same 557 sites used in developing the layering model. The log-normal distribution is described by the median shear wave velocity [i.e., the average of $\ln(V_s)$] at mid-depth of the layer and the standard deviation of the natural logarithm of the shear wave velocity ($\sigma_{\ln V_s}$). The median shear wave velocity for the layer is taken from a user-specified baseline velocity profile for the site, at the depth of the layer. The $\sigma_{\ln V_s}$ is assigned by the user to model a specific amount of variability. Given the baseline shear wave velocity for layer i [$V_{s,o}(i)$, assumed to represent the mean in logarithmic space], the standard deviation of the natural logarithm of V_s ($\sigma_{\ln V_s}$), and a random standard normal variable for layer i (Z_i), the shear wave velocity of layer i [$V_s(i)$] can be computed as [Toro 1995]:

$$V_S(i) = \exp\left(\ln[V_{s,o}(i)] + Z_i \cdot \sigma_{\ln Vs}\right) \tag{3.1}$$

The key issue is then the selection of the values of Z_i for each layer. Some researchers have assumed that Z_i values are perfectly correlated between layers [McGuire 1989; Toro et al. 1992), while others have assumed zero correlation [Costantino 1991]. Neither of these assumptions is consistent with velocity data, and they represent extreme conditions (i.e., perfect correlation versus statistical independence). Toro [1995] developed a model for the interlayer correlation of Z_i based on analysis of the same 557 shear wave velocity profiles previously discussed. In this model the standard normal variable for the surface layer (Z_1, i = 1) is independent of all other layers and defined as:

$$Z_1 = \varepsilon_1 \tag{3.2}$$

where ε_1 is a random normal variable with zero mean and unit standard deviation. Z_i is correlated with the layer above it using [Toro 1995]:

$$Z_i = \rho_{IL} \cdot Z_{i-1} + \varepsilon_i \cdot \sqrt{1 - \rho_{IL}^2} \tag{3.3}$$

where Z_{i-1} is the standard normal variable of the previous layer, ε_i is a new normal random variable with zero mean and unit standard deviation, and ρ_{IL} is the interlayer correlation coefficient. Toro [1995] modeled the interlayer correlation as depth (d) and layer thickness (t) dependent:

$$\rho_{IL}(d,t) = [1 - \rho_d(d)] \cdot \rho_t(t) + \rho_d(d) \tag{3.4}$$

where $\rho_d(d)$ is the depth-dependent component of the correlation coefficient and $\rho_t(t)$ is the thickness-dependent component of the correlation coefficient. These correlation coefficients are defined as [Toro 1995]:

$$\rho_d(d) = \begin{cases} \rho_{200} \cdot \left[\dfrac{d + d_o}{200 + d_o}\right]^b & , d \leq 200 \text{ m} \\ \rho_{200} & , d > 200 \text{ m} \end{cases} \tag{3.5}$$

$$\rho_t(t) = \rho_o \cdot exp\left(\frac{-t}{\Delta}\right) \tag{3.6}$$

where ρ_{200}, d_o, b, ρ_0, and Δ are model parameters.

Toro [1995] developed median shear wave velocity profiles for different site classes (i.e., ranges in V_{S30} that are incorporated in the building code) for use in developing randomized velocity profiles for generic site conditions. Toro [1995] also developed estimates of $\sigma_{\ln Vs}$ and interlayer correlation coefficient model parameters for site classes of V_{S30} > 760 m/sec, 360–760 m/sec, 180–360 m/sec, and < 180 m/sec. The depth to bedrock can be modeled using either a uniform, normal, or log-normal distribution. The statistical properties of the distribution are entered by the user.

3.3 GENERATED VELOCITY PROFILES

The Monte Carlo simulation feature in the program *Strata* is used to generate generic site profiles for use in site response analysis. As discussed in the previous section, Monte Carlo simulations require a median shear wave velocity profile and $\sigma_{\ln Vs}$. The median shear wave velocity profiles are called baseline profiles in this study. Four baseline profiles with V_{S30} equal to 200, 250, 400, and 550 m/sec are used to generate a total of four hundred soil profiles. Figure 3.2 shows the developed baseline shear wave velocity profiles.. These baseline velocity profiles were developed based on the velocity profiles presented by Toro [1995] for different site classes, which were then modified in this study to achieve the desired V_{S30} for each baseline profile. The minimum velocity at the surface varies between about 175 and 400 m/sec in the baseline profiles. The baseline profiles with V_{S30} of 200 and 250 m/sec reach their maximum shear wave velocities of 750 m/sec and 890 m/sec, respectively, at a depth of 400 m. The stiffer baseline profiles reach V_S equal to 1000 m/sec at shallower depths (150 m for V_{S30} of 550 m/sec and 300 m for V_{S30} of 400 m/sec). The site class dependent values of $\sigma_{\ln Vs}$ developed by Toro [1995] were used in generating the velocity profiles (see Table 3.1).

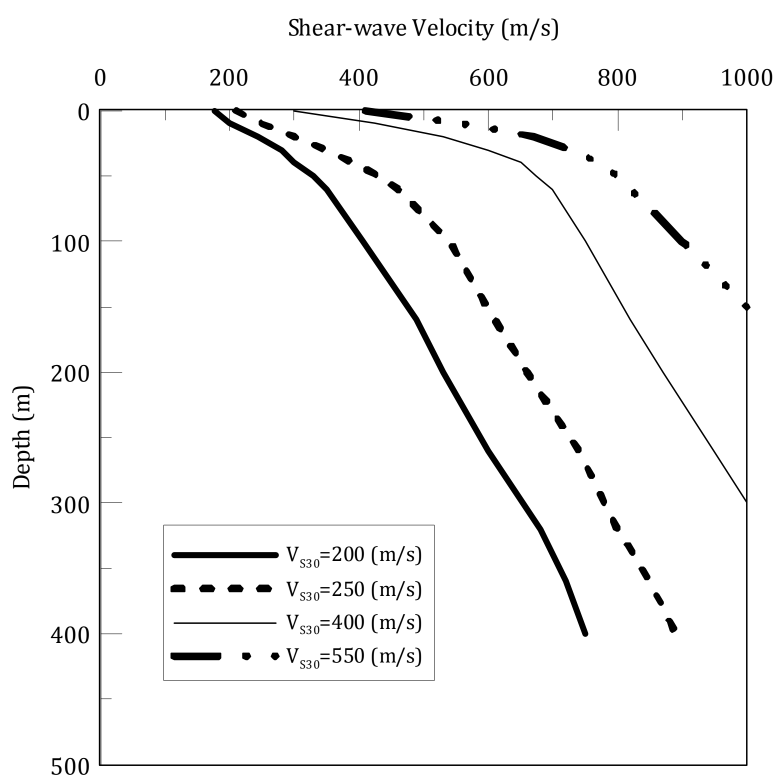

Figure 3.2 Baseline shear wave velocity profiles.

Generic layering was developed for the site profiles using the non-homogenous layering model of Toro [1995]. Depth to bedrock was varied using a uniform distribution. The minimum and maximum depths used for the uniform distribution were specified differently for each baseline velocity profile because each profile encounters rock-like velocities (~ 750 to 1000 m/sec) at different depths. The minimum and maximum depths used are listed in Table 3.1 for each baseline profile. The shear wave velocity of the half-space below the velocity profile was specified as 1000 m/sec. Velocities were assigned to each layer using Toro's interlayer correlation model and depth and thickness-dependent model for ρ_{IL}.. The predicted ρ_{IL} from Toro [1995] is plotted versus depth for thicknesses of 5 m, 20 m, and 50 m in Figure 3.3 for site class V_{S30} = 180–360 m/sec. This is the site class that is associated with the V_{S30} values of two of the baseline profiles. As shown in Figure 3.3, the interlayer correlation increases with depth for a given thickness; at the depth of 200 m approaches 1.0 for this site class. Note that thicker layers generally have a smaller interlayer correlation coefficient. In generating the velocity profiles, the shear wave velocity of layers is not allowed to exceed 1000 m/sec nor go below 100 m/sec.

While the nonlinear properties are not varied in the Monte Carlo simulation, modulus reduction and damping curves are assigned to each layer. The Darendeli [2001] model was used to develop the modulus reduction and damping curves as a function of mean effective stress (σ'_m), PI, and OCR. In this study PI and OCR are taken to be 10 and 1.0, respectively, for all layers. To model the stress dependence, nonlinear property curves were generated for σ'_0 equal to 0.6 atm, 1.4, atm, 2.7 atm, 4.9 atm, 8.0 atm, 15.7 atm, and 33.5 atm. The appropriate curves were assigned to each layer of the baseline profile based on the depth and a computed mean effective stress at the middle of each layer.

Examples of generated profiles from each baseline profile are shown in Figures 3.4 and 3.5. Note that the V_{S30} for each generated profile is different than the V_{S30} for the baseline profile. Each profile generated from a single baseline profile has different layering and a different shear wave velocity profile. While the baseline velocity profiles (Figure 3.2) vary smoothly with depth, the generated profiles vary more irregularly (Figures 3.4 and 3.5). In some profiles, an inversion in the shear wave velocity occurs (i.e., the velocity decreases with depth). The irregular pattern is more representative of a real site, while the smooth baseline profiles represent the average over many different sites. The average velocity profile for the generated profiles for a given baseline profile varies smoothly and matches the baseline profile well.

For each generated velocity profile, site characteristics such as the minimum shear wave velocity, V_{S30}, and the depth to bedrock are different. Various site parameters, including the average shear wave velocity in top 30 m (V_{S30}), the depth to engineering rock ($Z_{1.0}$), and V_{ratio} [i.e., $V_{ratio} = V_{S(20\text{-}30)} / V_{S10}$, where $V_{S(20\text{-}30)}$ is the average shear wave velocity between depths 20 m and 30 m and V_{S10} is the average shear wave velocity in top 10 m] are calculated for each generated profile. Histograms showing the distribution of each of these site parameters are given in Figure 3.6. V_{S30} in the generated profiles varies between 118 m/sec and 818 m/sec. The V_{S30} values of the generated profiles are evenly distributed between 150 m/sec and 750 m/sec, with fewer values less than 150 m/sec or greater than 750 m/sec. This range indicates that the generated sites include a representative range of soft to stiff soil profiles. The $Z_{1.0}$ values of the generated profiles range from 16 m to 640 m. Because softer sites with small V_{S30} tend to be found in deeper alluvial valleys, there is a relationship between V_{S30} and $Z_{1.0}$. As shown in Figure 3.7 for the generated profiles in this study, the softest sites are associated with the largest values of $Z_{1.0}$. The histograms in Figure 3.6 show that V_{ratio} varies from 0.56 to 2.76 in the generated profiles. Profiles with V_{ratio} less than 1.0 have V_{S10} greater than $V_{S20\text{-}30}$, indicating that the shear wave velocity generally does not increase with depth in the top 30 m. In these cases an inversion in the velocity occurs. In 11% of the generated profiles V_{ratio} is less than one. Large values of V_{ratio} indicate a significant increase in shear wave velocity within the top 30 m.

Table 3.1 **σ_{lnVs} and minimum and maximum rock depths used in generating velocity profiles.**

V_{S30} (m/sec)	σ_{lnVs}	Minimum Rock Depth (m)	Maximum Rock Depth (m)
200	0.31	150	650
250	0.31	100	600
400	0.27	30	550
550	0.27	15	300

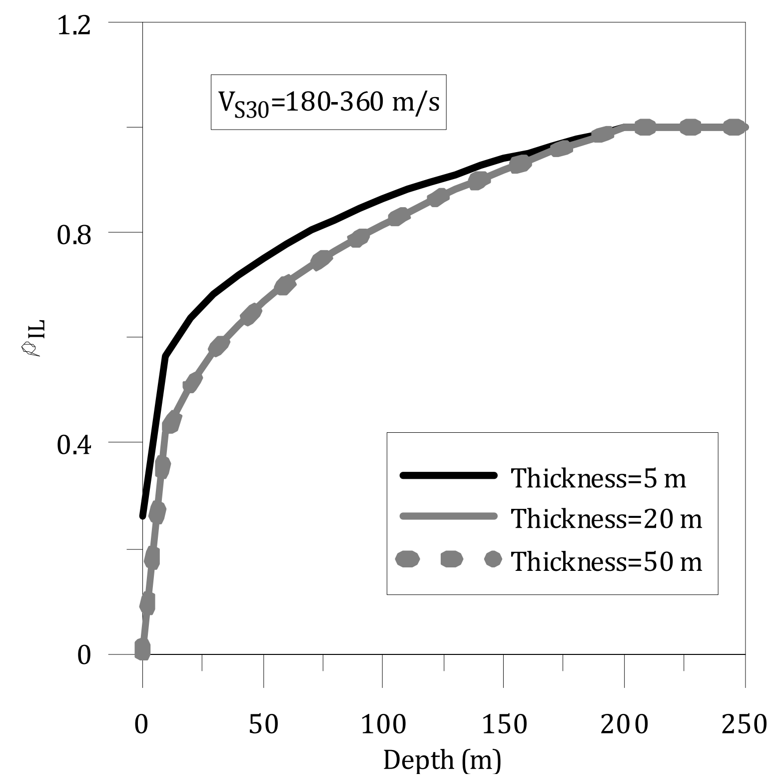

Figure 3.3 **The predicted ρ_{IL} from Toro [1995] as a function of depth for layer thicknesses of 5 m, 20 m, and 50 m and for site classV_{S30} = 180–360 m/sec.**

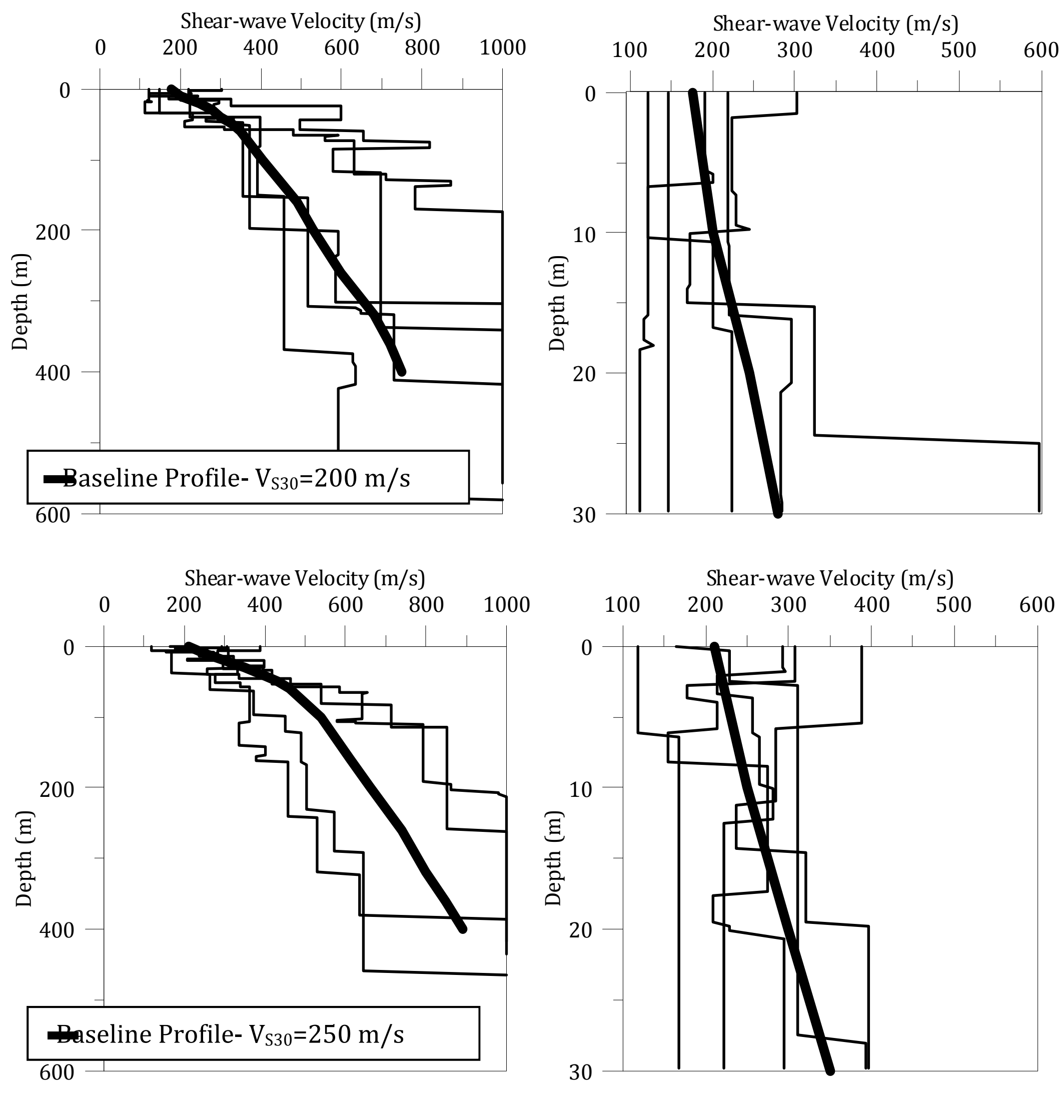

Figure 3.4 **Examples of generated velocity profiles for V_{S30} = 200 and 250 m/sec baseline profiles.**

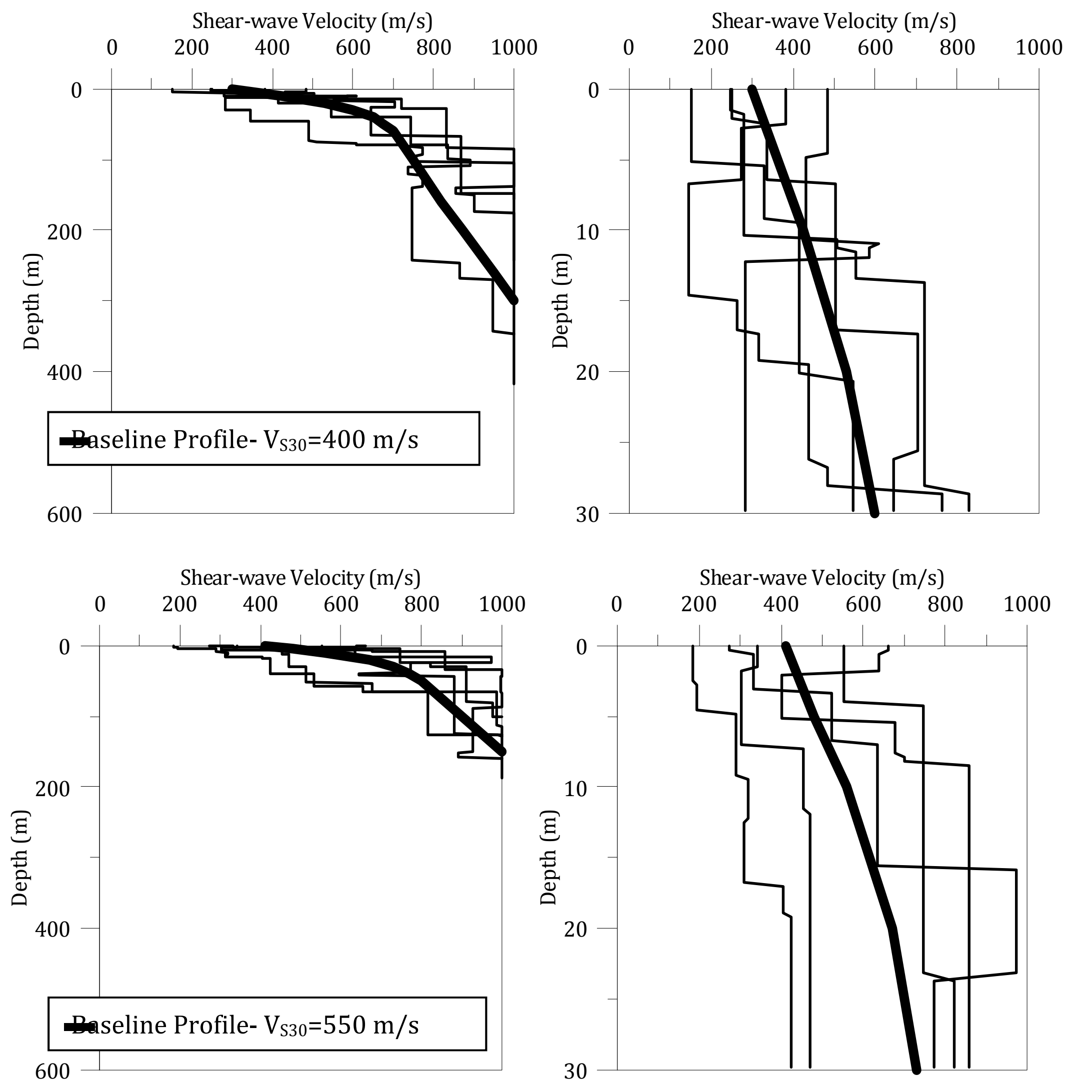

Figure 3.5 **Examples of generated velocity profiles for V_{S30} = 400 and 550 m/sec baseline profiles.**

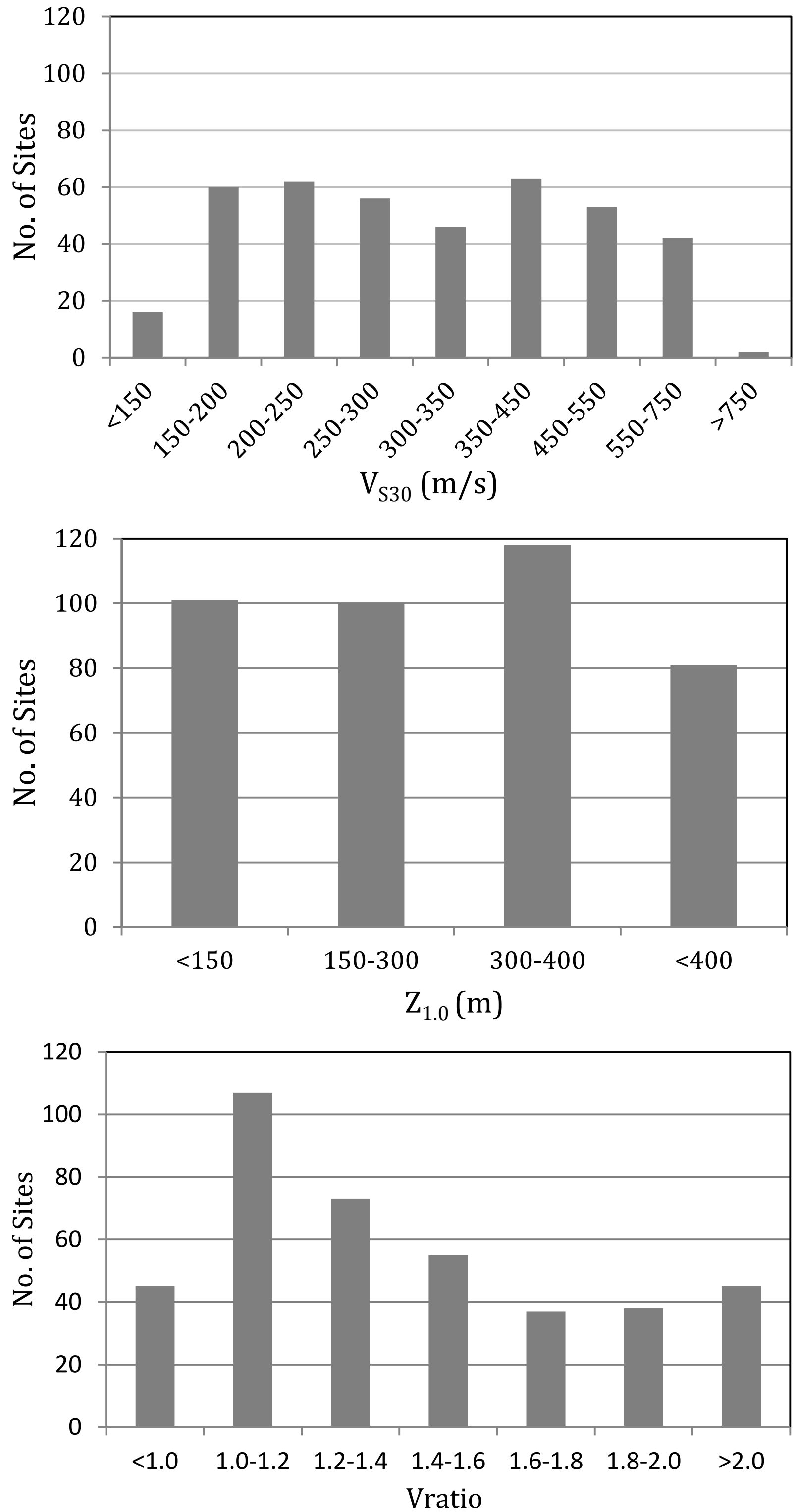

Figure 3.6 Distiribution of V_{S30}, $Z_{1.0}$, and V_{ratio} of the generated soil profiles.

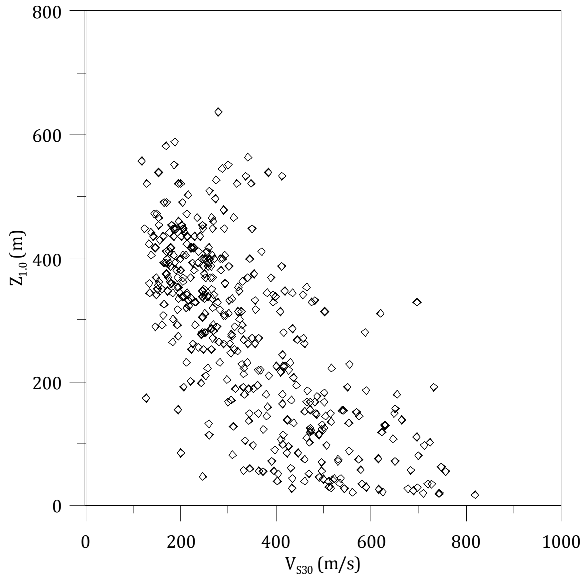

Figure 3.7 Relationship between $Z_{1.0}$ and V_{S30} for the generated profiles.

3.4 MODEL DEVELOPMENT

An empirical site amplification models typically includes two components: a linear elastic component and a nonlinear component. The linear elastic component represents amplification under linear elastic soil conditions (i.e., low intensity shaking), while the nonlinear component includes the effects of soil nonlinearity at high intensity shaking. These AFs are generally multiplicative (additive in logarithmic space), which can be written as:

$$\ln(\mathrm{AF}) = \ln(\mathrm{AF})_{\mathrm{lin}} + \ln(\mathrm{AF})_{\mathrm{nl}} \tag{3.7}$$

The linear elastic component is derived from the computed amplification for low intensity input motions. In this study AFs from input motions with a rock input PGA of 0.01g were used to develop the linear elastic AF model. Computed AFs from larger intensity input motions were used to develop the nonlinear component of the AF model. As discussed earlier, equivalent-linear analysis using the RVT approach was used to compute the seismic response of the generated profiles under a wide range of input intensities. In the RVT approach, the input motion is described by a response spectrum, this response spectrum is converted to an FAS, the FAS is propagated to the ground surface using the site frequency domain transfer function, and the surface FAS is converted to an acceleration response spectrum. The ratio of the surface response spectrum to the input response spectrum at each period defines the AF for each period. The input motions are defined using seismological source theory and are essentially the same as those described in Chapter 3.

After computing AFs for a range of sites subjected to a range of input intensities, the AF values are used to develop the empirical amplification model. A functional form for the model is developed and the model coefficients are determined through maximum likelihood regression.

4 Models for Linear Elastic Site Amplification

4.1 INTRODUCTION

This chapter presents the development of the linear elastic component of the site amplification model. The functional form is developed separately for shorter periods ($T < 1.0$ sec) and longer periods ($T \geq 1.0$ sec). At short periods the amplification model includes the effects of V_{S30} and V_{ratio}, while at long periods the amplification model includes the effects of V_{S30} and $Z_{1.0}$.

4.2 V_{S30} COMPONENT OF LINEAR ELASTIC SITE AMPLIFICATION MODEL

Figures 4.1 and 4.2 show the computed AFs versus V_{S30} for spectral periods shorter and longer than 1.0 sec, respectively. The data in Figures 4.1 and 4.2 generally show that a decrease in V_{S30} corresponds with an increase in amplification, results that are consistent with previous studies. At shorter periods (i.e., $T \leq 0.5$), amplification increases over the full V_{S30} range. At longer periods ($T = 5.0$ and 10.0 sec in Figure 5.2), the amplification stays close to 1.0 for a range of larger V_{S30} values before beginning to increase at smaller V_{S30}. The V_{S30} below which amplification starts to increase is called V_{ref}, which generally decreases as the period increases

Linear elastic AF models developed previously and used in most GMPEs incorporate a linear dependence between lnAF and $\ln(V_{S30}/V_{ref})$ using:

$$\ln(\mathrm{AF})_{\mathrm{lin}} = \begin{cases} a_1 \cdot \ln\left(\dfrac{V_{S30}}{V_{ref}}\right) & \text{if } V_{S30} < V_{ref} \\ 0 & \text{if } V_{S30} \geq V_{ref} \end{cases} \tag{4.1}$$

A maximum likelihood regression is used to fit Equation (4.1) to the AF data at each spectral period. V_{ref} is fixed, based on visual identification from the data (Table 5.1) because regressed values of V_{ref} using the maximum likelihood method were not consistent with the data. Figures 4.3 and 4.4 show the AF data again, along with a linear fit from Equation (4.1). The model parameters (a_1 and V_{ref}) and the resulting standard deviation of the regression (σ_{lnAF}) are shown in Table 4.1. As shown in Table 4.1, V_{ref} is equal to 1000 m/sec at short periods and then decreases as spectral periods increase beyond 0.5 sec. Slope a_1 is almost the same for shorter periods (~ -0.45 for $T \leq 0.3$ sec), increases in the middle periods (~ -0.5 to -0.7 for $T = 0.5$ to 2.0 sec), and then becomes smaller at long periods greater than 2.0 sec. σ_{lnAF} ranges from 0.11 at

PGA, then increases to 0.2 to 0.25 for T = 0.2 to 1.0 sec, and then decreases at the longest periods. Comparing the model predictions to the data in Figures 4.3 and 4.4, it appears that a linear fit does not match the data appropriately, particularly at shorter periods and smaller V_{S30}. In these cases, a second-order polynomial may fit the AF data better.

A second-order polynomial is considered for the relationship between lnAF and $\ln(V_{S30}/V_{ref})$ and is described as:

$$\ln(\mathrm{AF})_{\mathrm{lin}} = \begin{cases} a_1 \cdot \ln\left(\frac{V_{S30}}{V_{ref}}\right) + a_2 \cdot \left[\ln\left(\frac{V_{S30}}{V_{ref}}\right)\right]^2 & \text{if } V_{S30} < V_{ref} \\ 0 & \text{if } V_{S30} \geq V_{ref} \end{cases} \tag{4.2}$$

A maximum likelihood regression is used to fit Equation (4.2) to the data at each period. The same V_{ref} values previously identified are used. The values of V_{ref}, a_1, a_2, and $\sigma_{\ln AF}$ for each period are listed in Table 4.2. The resulting second order polynomials are shown in Figures 4.5 and 4.6, along with the linear fit and the AF data. As compared with the linear fit, the second order polynomial better fits the data, particularly at smaller V_{S30}. At periods longer than 1.0 sec, the parameter a_2 is close to zero, indicating that a linear fit best represents the data. Comparing the $\sigma_{\ln AF}$ of polynomial and linear fits, the polynomial fit decreases $\sigma_{\ln AF}$ by 15 to 25% at periods shorter than about 0.5 sec but does not significantly decrease it at longer periods. Therefore, the linear fit appears to be appropriate for periods greater than 0.5 sec.

Table 4.1 Regression coefficients and $\sigma_{\ln AF}$ for Equation (4.1).

T (sec)	a_1	V_{ref} (m/sec)	$\sigma_{\ln AF}$
PGA	-0.49	1000	0.11
0.05	-0.47	1000	0.12
0.1	-0.44	1000	0.15
0.2	-0.42	1000	0.24
0.3	-0.46	1000	0.24
0.5	-0.52	1000	0.20
1.0	-0.62	850	0.20
2.0	-0.72	600	0.19
5.0	-0.46	500	0.18
10.0	-0.21	500	0.06

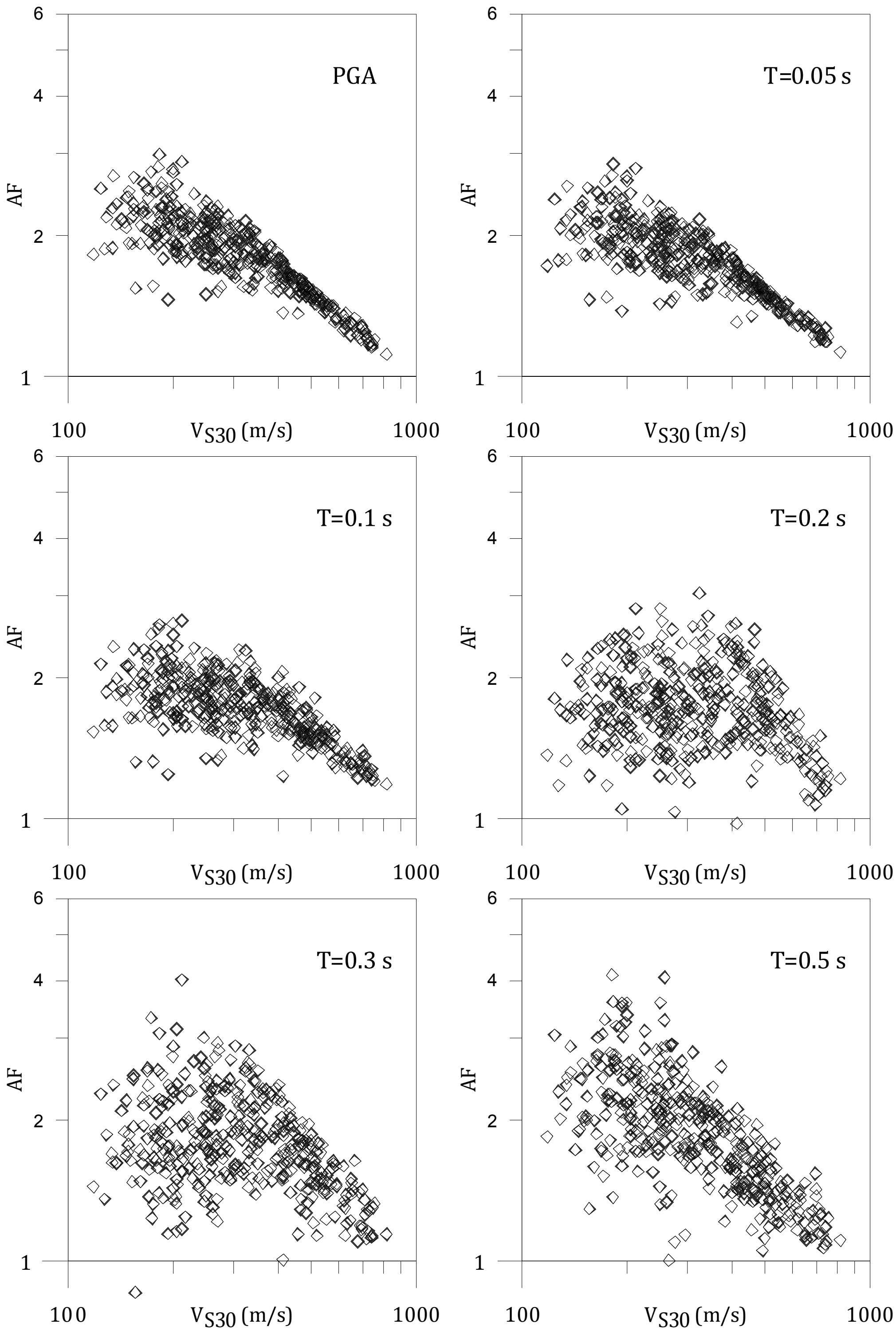

Figure 4.1 Amplification factor versus V_{S30} for all generated profiles at short periods (T ≤ 0.5 sec).

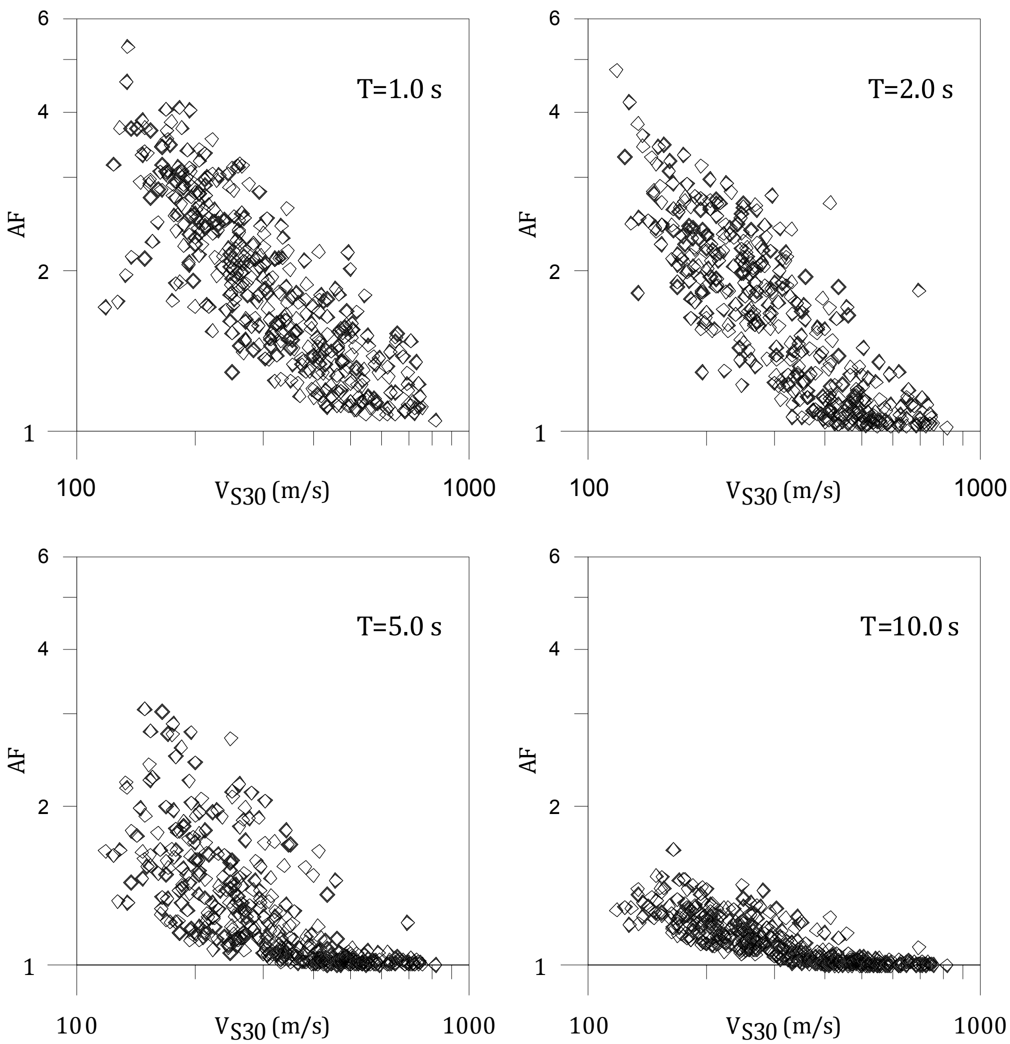

Figure 4.2 **Amplification factor versus V_{S30} for all generated profiles at long periods (T ≥ 1.0 sec).**

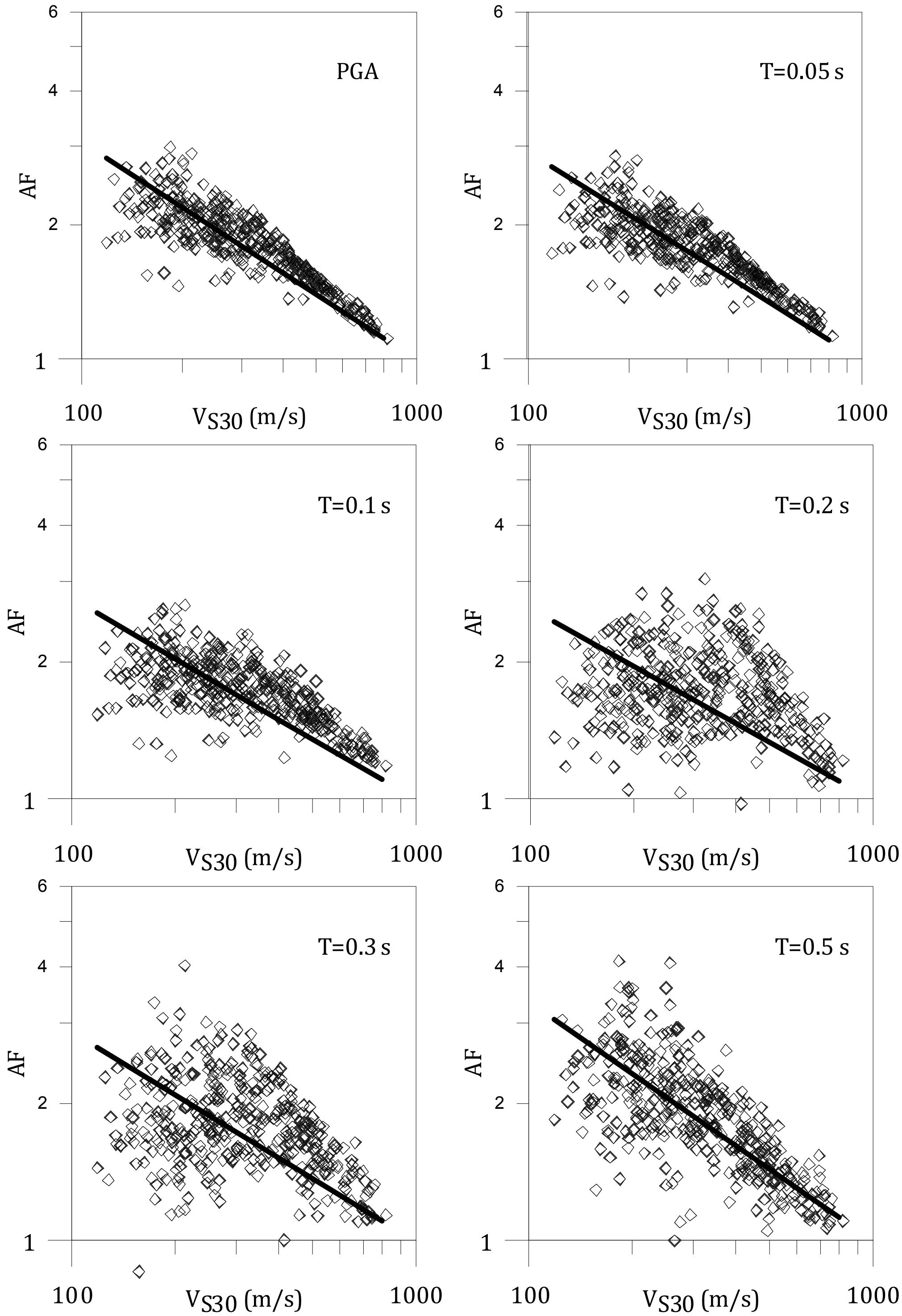

Figure 4.3 **Linear fit to amplification factor versus V_{S30} data for all generated profiles at short periods (T ≤ 0.5 sec).**

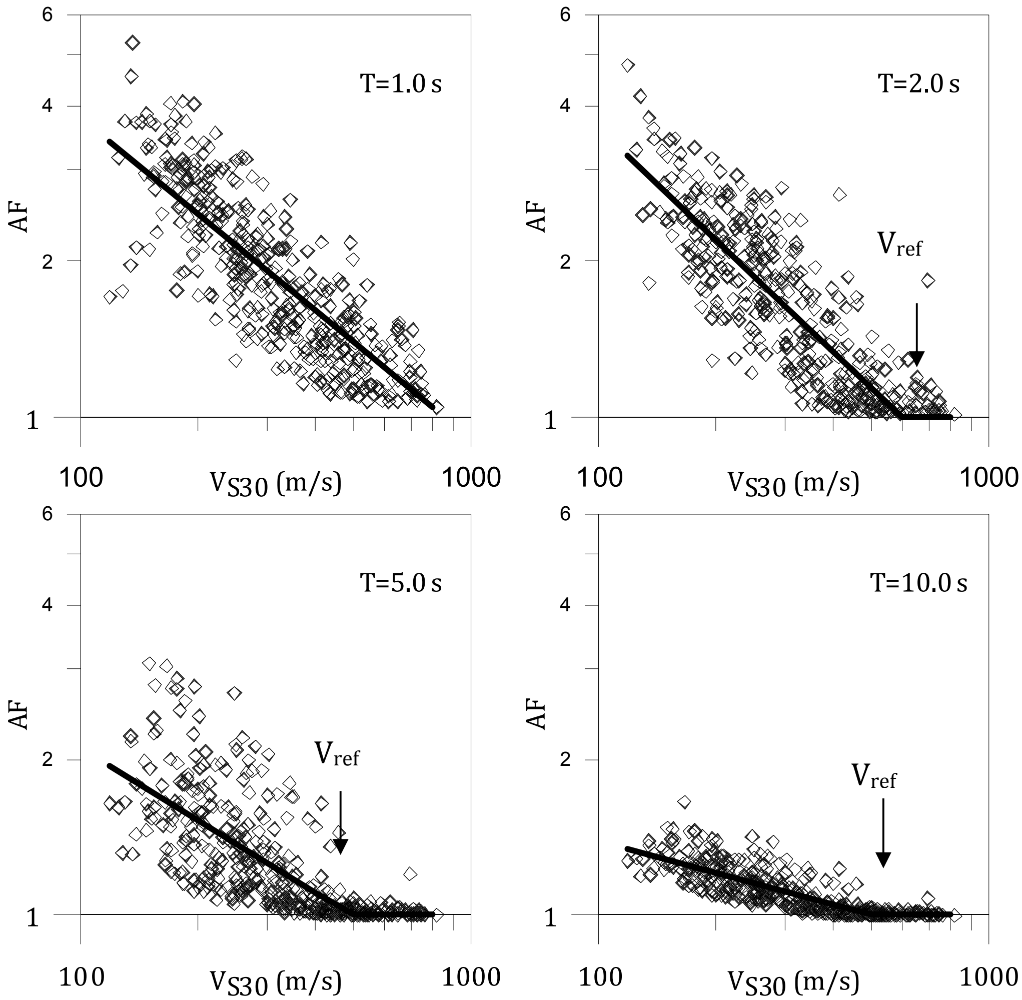

Figure 4.4 **Linear fit to amplification factor versus V_{S30} data for all generated profiles at long periods (T ≥ 1.0 sec).**

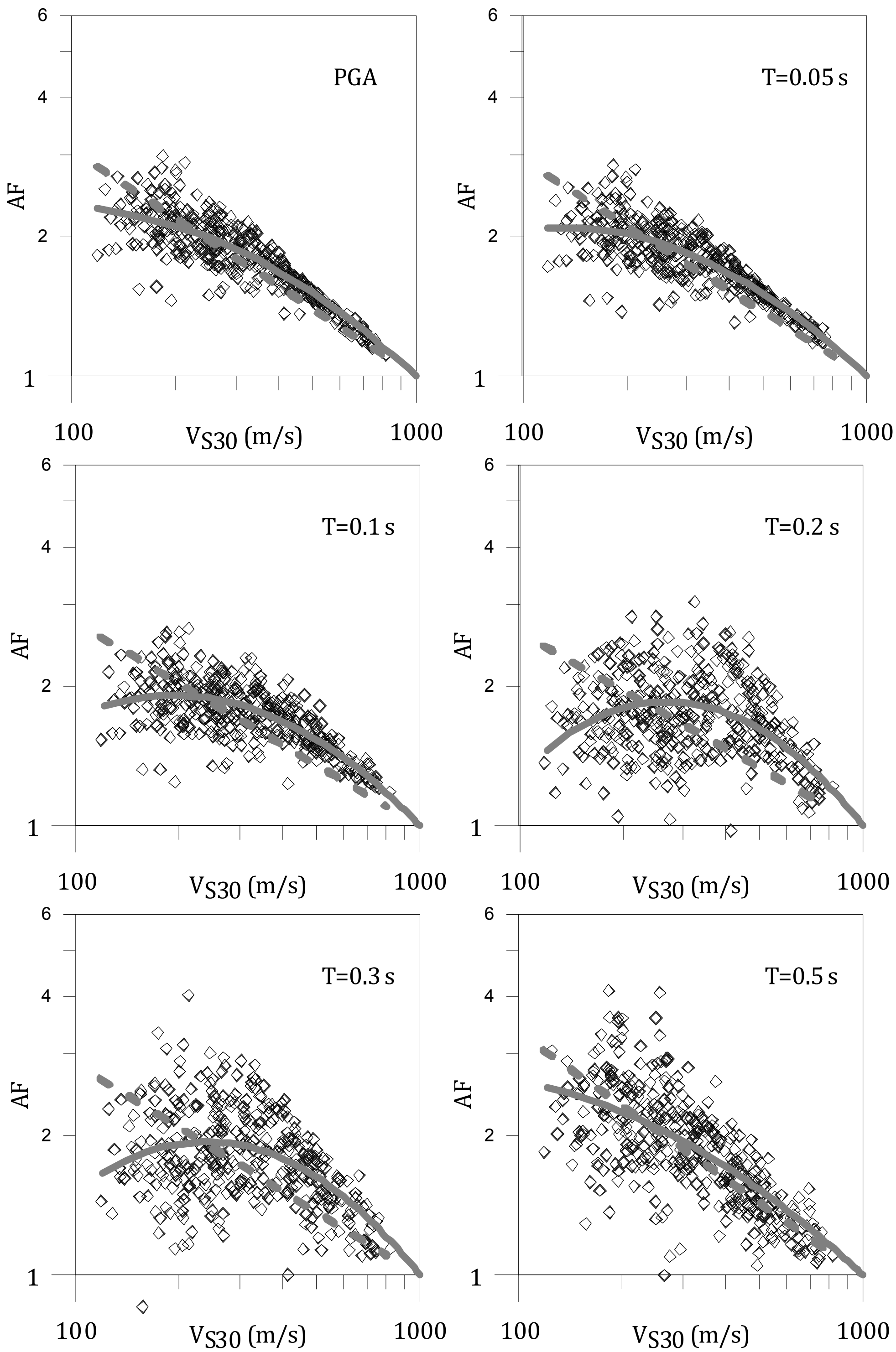

Figure 4.5 Linear and nonlinear fits to amplification factor versus V_{S30} data for all generated profiles at short periods ($T \leq 0.5$ sec).

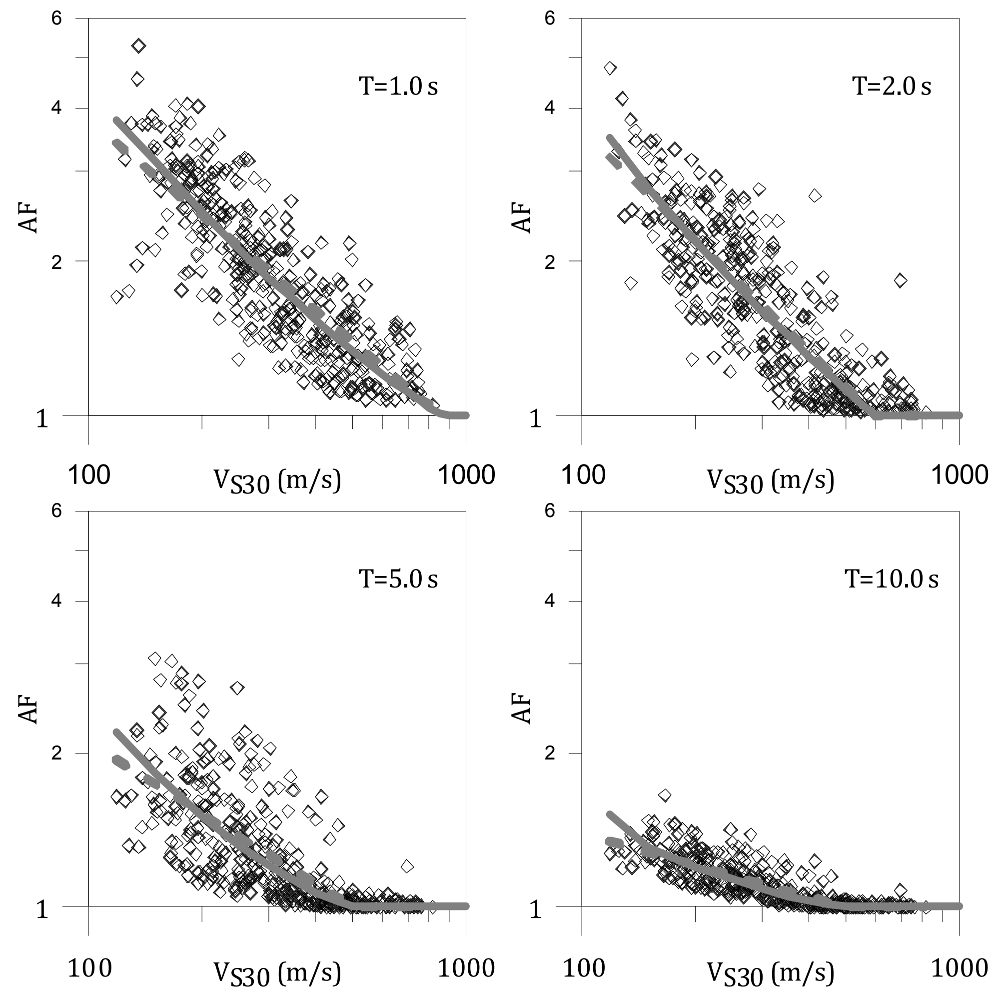

Figure 4.6 **Linear and nonlinear fits to amplification factor versus V_{S30} data for all generated profiles at long periods (T ≥ 1.0 sec).**

Table 4.2 Regression coefficients and σ_{lnAF} for Equation (4.2).

T (sec)	a_1	a_2	V_{ref} (m/sec)	σ_{lnAF} [Eq. (4.2])	σ_{lnAF} [Eq. (4.1)]	% Reduction
PGA	-0.7	-0.15	1000	0.09	0.11	18
0.05	-0.72	-0.17	1000	0.10	0.12	17
0.1	-0.79	-0.24	1000	0.11	0.15	27
0.2	-0.94	-0.36	1000	0.19	0.24	21
0.3	-0.93	-0.33	1000	0.20	0.24	17
0.5	-0.70	-0.12	1000	0.19	0.20	5
1.0	-0.49	0.09	850	0.19	0.20	5
2.0	-0.62	0.09	600	0.19	0.19	1
5.0	-0.26	0.08	500	0.20	0.18	-11
10.0	-0.12	0.09	500	0.07	0.06	-17

4.3 V_{ratio} COMPONENT OF LINEAR ELASTIC SITE AMPLIFICATION MODEL

To define the functional form describing the variation in AF with V_{ratio}, the residual of each data point relative to the predicted value from the model is computed and plotted versus V_{ratio}. The residual is calculated as:

$$\text{Residual} = [\ln(\text{AF})]_{\text{Data}} - [\ln(\text{AF})]_{\text{Predicted}} \tag{4.3}$$

where $[\ln(AF)]_{Predicted}$ is calculated using Equation (4.2) for periods shorter than 1.0 sec (short periods) and Equation (4.1) for $T \geq 1.0$ sec (long periods). $[\ln(AF)]_{Data}$ is the computed AF for the soil profile. The calculated residuals are plotted versus V_{ratio} in Figures 4.7 and 4.8 for short and long periods, respectively. There is a strong positive trend between the residuals and V_{ratio} at all six short periods. In these cases, sites with larger V_{ratio} experience larger amplification. At long periods, the trend between the residuals and V_{ratio} is not significant, indicating that the AF at long periods is not significantly influenced by V_{ratio}.

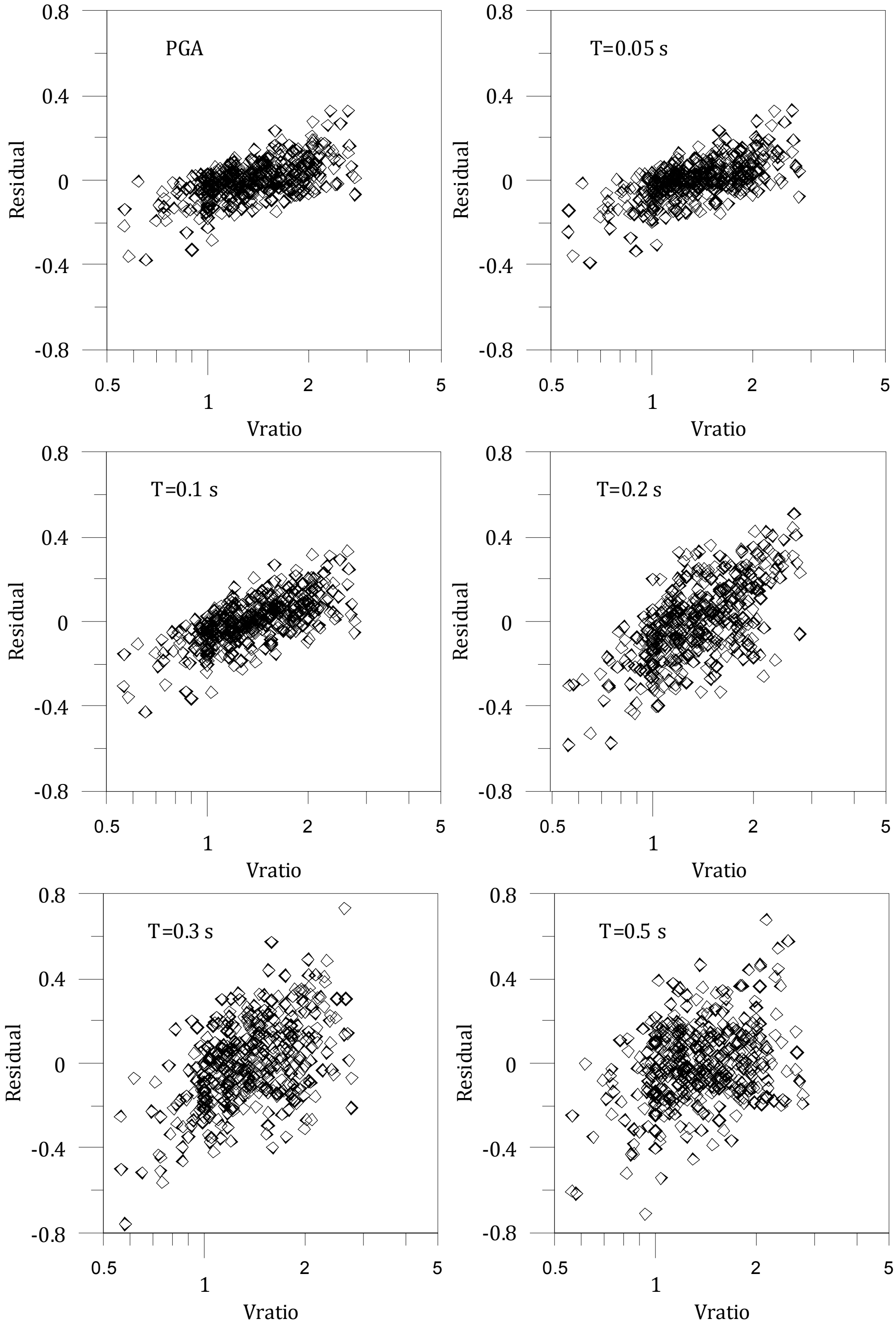

Figure 4.7 Residuals versus V_{ratio} at short periods (T ≤ 0.5 sec).

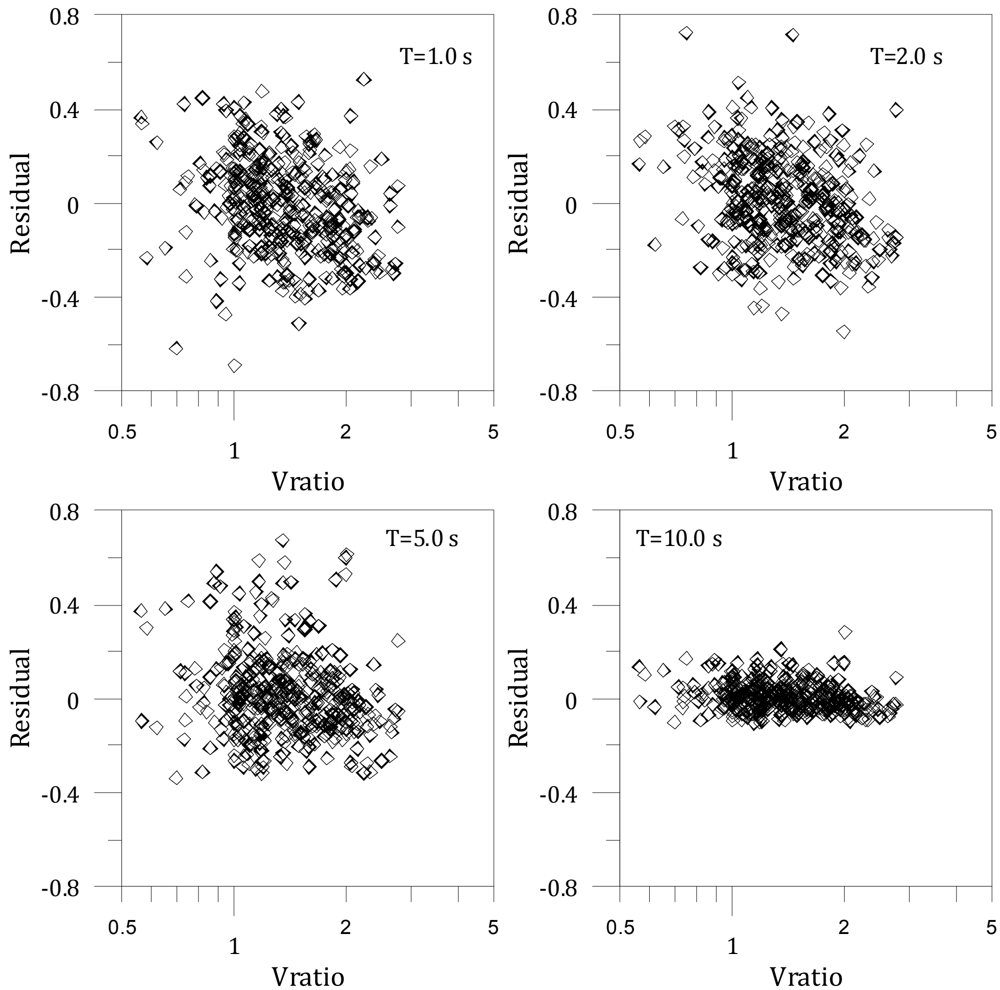

Figure 4.8 Residuals versus V_{ratio} at long periods (T > 1.0 sec).

As previously discussed, AF is V_{S30} dependent, and thus it is likely that the influence of V_{ratio} on site amplification is also V_{S30} dependent. To identify the functional form that describes the dependence of AF on V_{S30} and V_{ratio}, residuals were plotted versus V_{ratio} for different bins of V_{S30}. Soil profiles were separated into 8 V_{S30} bins as follows: V_{S30}<150 m/sec, 150 m/sec <V_{S30}<200 m/sec, 200 m/sec <V_{S30}<250 m/sec, 250 m/sec <V_{S30}<300 m/sec, 300 m/sec <V_{S30}<350 m/sec, 350 m/sec <V_{S30}<450 m/sec, 450 m/sec <V_{S30}<550 m/sec, and 550 m/sec <V_{S30}<750 m/sec. To normalize the effect of V_{ratio} on AF in a manner similar to V_{ref}, V_{ratio} was normalized by a V_{ratio} value of 1.4, which is the average V_{ratio} of all four hundred generated profiles. Residuals were plotted versus $\ln\left(\frac{V_{ratio}}{1.4}\right)$ in Figures 4.9, 4.10, and 4.11 for periods PGA, 0.2 sec, and 0.5 sec, respectively. Because the other short periods show similar trend as these periods, only these three periods are shown.

For PGA (Figure 4.9), there is a linear relationship between the residual and $\ln\left(\frac{V_{ratio}}{1.4}\right)$ for all V_{S30} bins. This relationship that can be described as:

$$\text{Residual} = a_3 \cdot \ln\left(\frac{V_{ratio}}{1.4}\right) \tag{4.4}$$

Equation (4.4) is fit to the residuals within each V_{S30} bin, and the slope of each fit (i.e., a_3) is shown in Figure 4.9. The slope a_3 is different for each V_{S30} bin, with the largest values occurring at smaller V_{S30}. The slope decreases with increasing V_{S30}, and for V_{S30} greater than about 450 m/sec the slope is essentially zero.

For periods of 0.2 sec (Figure 4.10), a linear trend between the residual and $\ln\left(\frac{V_{ratio}}{1.4}\right)$ is also observed, but the scatter is more significant. Again, Equation (4.4) is fit to the data within each V_{S30} bin. The slope of the linear fit (a_3) varies across V_{S30} bins with larger V_{S30} values, displaying smaller slopes. For T = 0.5 sec (Figure 4.11), a similar trend is observed with the slope decreasing with increasing V_{S30}; for this period the slope even becomes negative for larger V_{S30} (although significant scatter in the data exists). Figure 4.12 plots the derived values of a_3 versus the median V_{S30} of each bin for periods of PGA, 0.2 sec, and 0.5 sec. The data for PGA clearly shows a_3 as a constant at smaller V_{S30}, and then a_3 decreases as V_{S30} increases. At V_{S30} of about 500 m/sec, a_3 becomes zero. The other periods show similar trends, although not as clearly.

Using the trends shown in Figure 4.12, an expression that describes the slope a_3 as a function of V_{S30} is developed. This expression models a_3 as decreasing linearly between V_{S30} values of V_a and V_b, and remaining constant outside of these values. The V_{S30} below which a_3 stays constant is V_a, and the V_{S30} value above which a_3 is zero is V_b. a_0 is the value of the slope for V_{S30} less than V_a. The resulting expression is given by:

$$a_3 = \begin{cases} a_0, V_{S30} \le V_a \\ a_0 - \dfrac{a_0}{(V_b - V_a)} \cdot (V_{S30} - V_a), V_a < V_{S30} \le V_b \\ 0, V_{S30} > V_b \end{cases} \tag{4.5}$$

where V_a, V_b, and a_0 are period dependent.

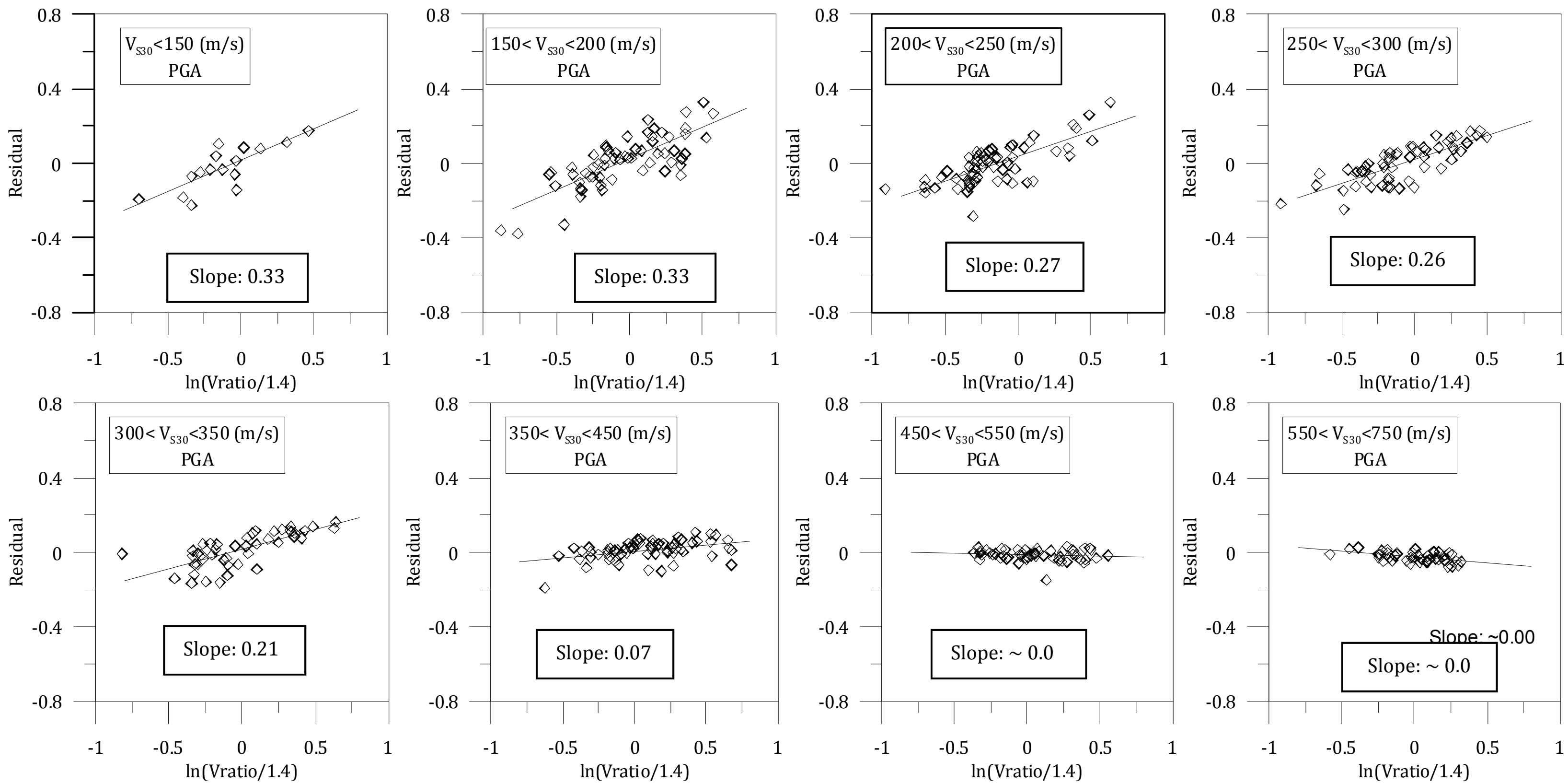

Figure 4.9 Residuals versus ln(V_{ratio}/1.4) for different V_{S30} bins at PGA.

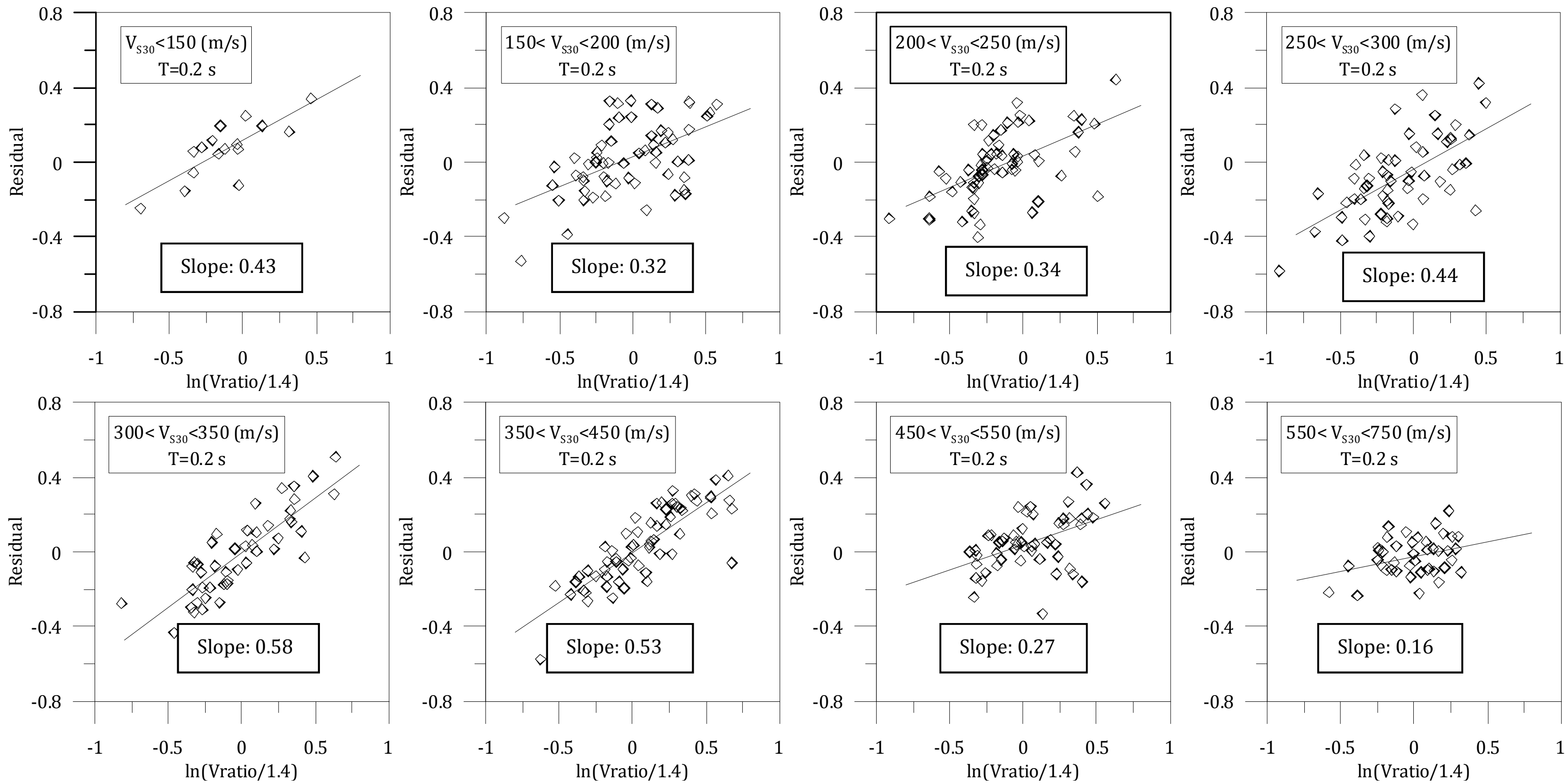

Figure 4.10 Residuals versus ln(V_{ratio}/1.4) for different V_{S30} bins at T = 0.2 sec.

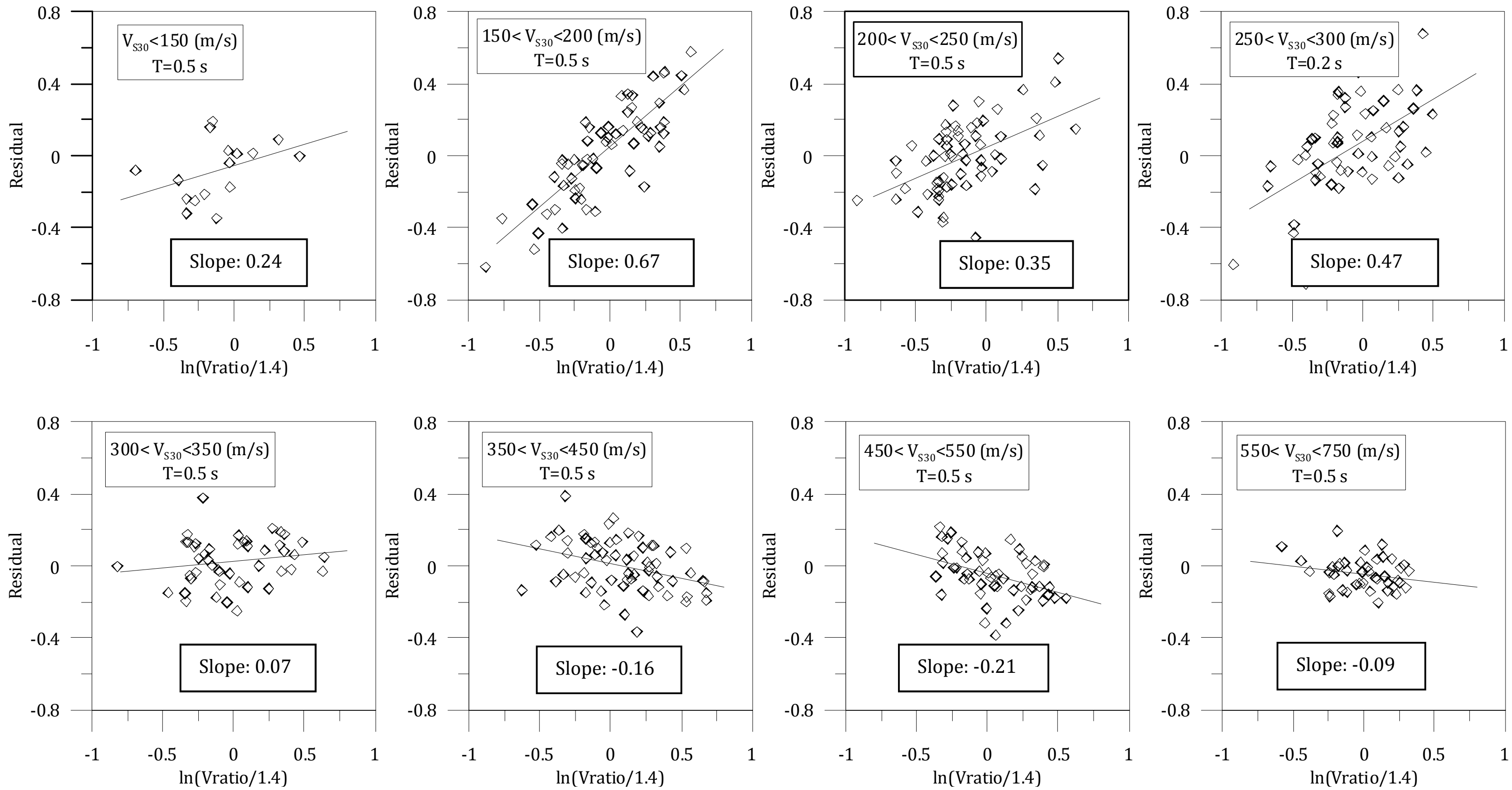

Figure 4.11 Residuals versus ln(V_{ratio}/1.4) for different V_{S30} bins at T = 0.5 sec.

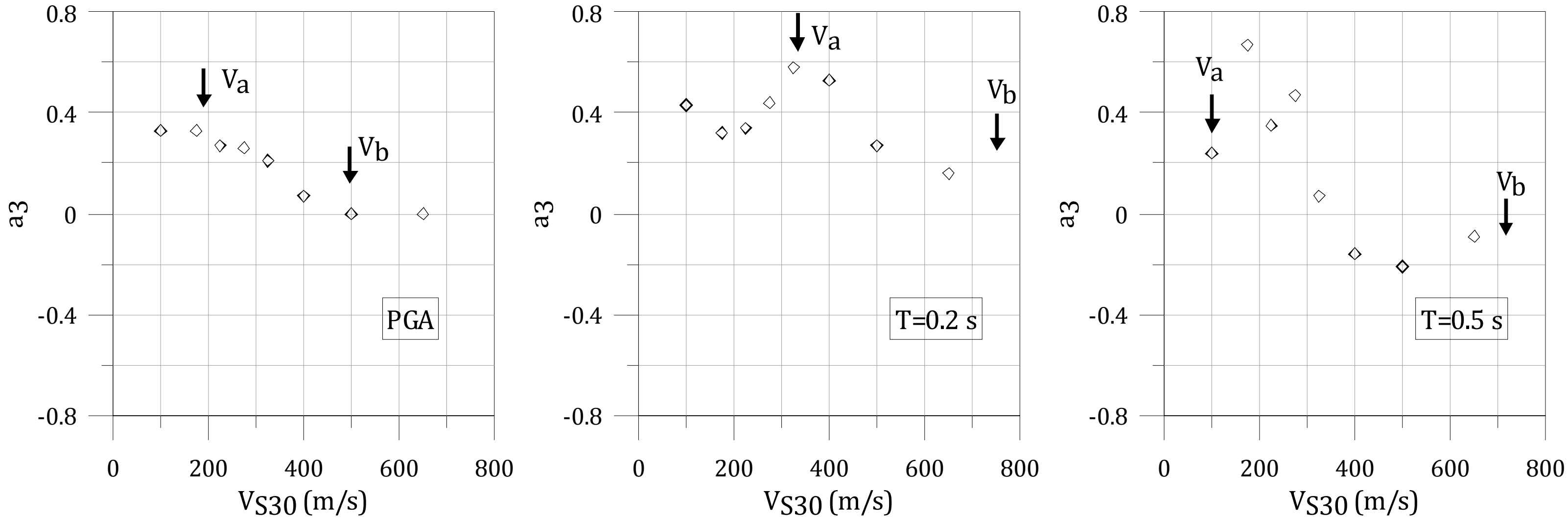

Figure 4.12 Computed a_3 for each V_{S30} bin versus the median V_{S30} of each bin for PGA, T = 0.2 sec and 0.5 sec.

Considering the influence of V_{ratio} identified above and the functional forms that model this influence, the following model is proposed for linear elastic amplification for spectral accelerations at $T \leq 0.5$ sec:

$$\ln(AF)_{lin} = \begin{cases} a_1 \cdot \ln\left(\frac{V_{S30}}{V_{ref}}\right) + a_2 \cdot \left[\ln\left(\frac{V_{S30}}{V_{ref}}\right)\right]^2 + a_3 \cdot \ln\left(\frac{V_{ratio}}{1.4}\right) & \text{if } V_{S30} < V_{ref} \\ 0 & \text{if } V_{S30} \geq V_{ref} \end{cases} \quad (4.6)$$

In Equation (4.6) a_3 is defined by Equation (4.5). The parameters a_1, a_2, a_0, V_a, and V_b are estimated by a maximum likelihood regression on the complete AF dataset for an input PGA_{rock} of 0.01*g*. Table 4.3 lists the model parameters for all six short periods.

To evaluate the effect of adding V_{ratio} to the linear elastic amplification model, the standard deviation of the data relative to different models is computed. The standard deviation (σ_{lnAF}) is computed as the standard deviation of the ln residuals (i.e., $\ln(AF)_{Data} - \ln(AF)_{predicted}$), and it is computed for both the model that does not incorporate V_{ratio} [Equation (4.2)] and the model that includes V_{ratio} [Equation (4.6)]. The computed values of σ_{lnAF} are listed in Table 4.4 for each period considered. At shorter periods, the inclusion of V_{ratio} decreases the standard deviation by more than 30% while the decrease is about 10% at T = 0.5 sec.

The variation of amplification with V_{S30} for different values of V_{ratio} for the developed model [i.e., Equation (4.6)] is shown in Figure 4.13 for the six periods considered. The curves demonstrate that amplification is larger for larger values of V_{ratio}, and this effect is larger at smaller values of V_{S30}.

Table 4.3 **Regression coefficients of the linear elastic amplification model [Equations (4.5) and (4.6)].**

T (sec)	a_1	a_2	a_0	V_a (m/sec)	V_b (m/sec)	V_{ref} (m/sec)
PGA	-0.69	-0.13	0.34	176	481	1000
0.05	-0.70	-0.15	0.37	147	512	1000
0.1	-0.76	-0.21	0.38	110	737	1000
0.2	-0.90	-0.32	0.44	414	726	1000
0.3	-0.89	-0.28	0.57	100	750	1000
0.5	-0.67	-0.1	0.39	100	750	1000

Table 4.4 **σ_{lnAF} of linear elastic amplification models with and without V_{ratio}.**

T (sec)	σ_{lnAF} (without V_{ratio})	σ_{lnAF} (with V_{ratio})	% Reduction
PGA	0.09	0.06	33
0.05	0.10	0.06	40
0.1	0.11	0.08	27
0.2	0.19	0.14	26
0.3	0.20	0.16	20
0.5	0.19	0.17	10

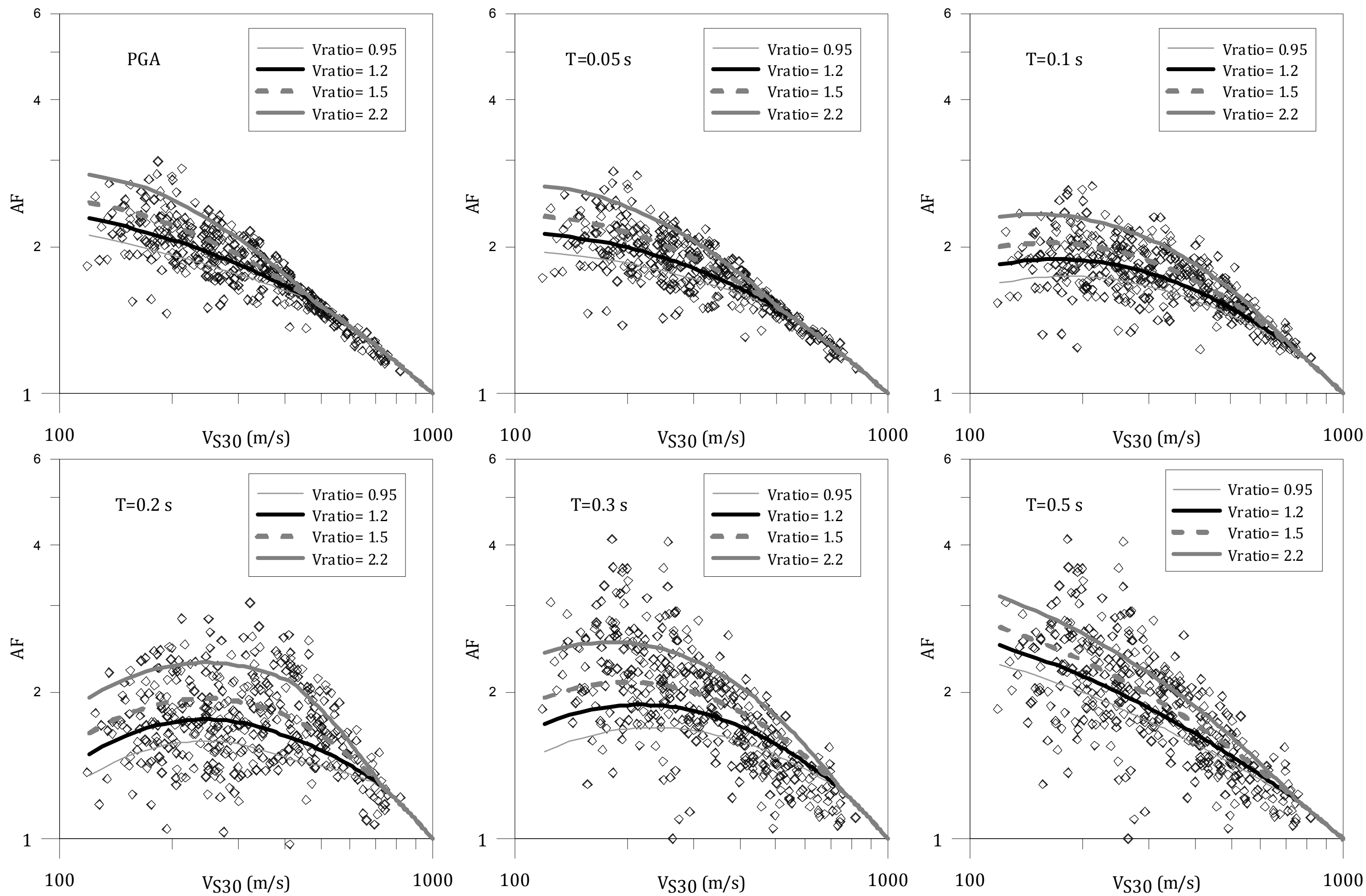

Figure 4.13 Model predictions for different values of V_{ratio}.

4.4 $Z_{1.0}$ COMPONENT OF LINEAR ELASTIC SITE AMPLIFICATION MODEL

As discussed above, a linear trend between ln(AF) and ln(V_{S30}/V_{ref}) best fits the amplification data for periods greater than or equal to 1.0 sec. As shown, AF is not strongly dependent on V_{ratio} for these periods. Amplification at long periods is controlled predominantly by the depth of soil, such that $Z_{1.0}$ is an important parameter to include in the amplification model. To consider the appropriate functional form for the amplification model that includes $Z_{1.0}$, the amplification data are separated into 4 bins of $Z_{1.0}$, and AF is plotted versus V_{S30}/V_{ref} for each bin. Figure 4.14 plots AF versus V_{S30}/V_{ref} for a spectral period of 2.0 sec. The slope of the linear fit of AF versus V_{S30} varies for different bins of $Z_{1.0}$ and generally increases with increasing $Z_{1.0}$, indicating that the slope of the linear fit is $Z_{1.0}$ dependent. The AF data for the other long periods show a similar relationship with $Z_{1.0}$ [Navidi 2012].

A model for this relationship has been proposed by Kottke [2011] and is adopted in this study. This model is described as:

$$\ln(\mathrm{AF})_{lin} = \begin{cases} \mathrm{a}_1 \cdot \alpha \cdot \ln\left(\dfrac{\mathrm{V_{S30}}}{\mathrm{V_{ref}}}\right) & \text{if } \mathrm{V_{S30}} < \mathrm{V_{ref}} \\ 0 & \text{if } \mathrm{V_{S30}} \geq \mathrm{V_{ref}} \end{cases} \tag{4.7}$$

$$\alpha = \left(\frac{\min(Z^*, Z_{1.0}) + 1}{Z^* + 1}\right)^b \tag{4.8}$$

Z^* is the depth (in meters) above which $Z_{1.0}$ no longer influences the amplification, and a_1 is the slope of the ln(AF) versus ln(V_{S30}/V_{ref}) relationship. In the model proposed by Kottke [2011], Z^* is defined as a function of frequency, and b is constant at all periods. In this study, Z^* and b are estimated using the maximum likelihood regression method for each period.

The parameters a_1, Z^*, and b computed via the maximum likelihood regression for the four long periods are listed in Table 4.5 along with the standard deviation of the model with and without considering the $Z_{1.0}$ effect. Small values of Z^* at periods of 1.0 and 2.0 sec indicate that a smaller range of depth to bedrock influences amplification at these periods. Larger values of $Z_{1.0}$ do not influence amplification at T = 1.0 sec and 2.0 sec because these larger values of $Z_{1.0}$ generate amplification at much longer periods. The larger Z^* values for periods of 5.0 and 10.0 sec indicates that all values of $Z_{1.0}$ influence amplification at these periods. Figure 4.15 shows the variation of α with $Z_{1.0}$ for each long period. At T = 1.0 sec, α approaches 1.0 for $Z_{1.0}$ greater than 100 m. While for T = 10.0 sec, α does not reach 1.0 until $Z_{1.0}$ is equal to 1000 m.

The variation of amplification with V_{S30} for different values of $Z_{1.0}$ for the developed model in Equations (4.7) and (4.8) is shown in Figure 4.16 for the four periods considered. Relationships are shown for four values of $Z_{1.0}$ that represent the range in the data. The influence of $Z_{1.0}$ at T = 1.0 sec is not significantly different because the derived value of Z^* is relatively small. The influence of different values of $Z_{1.0}$ is more readily apparent in the data for periods of

5.0 and 10.0 sec. Nonetheless, the reduction in σ_{lnAF} when $Z_{1.0}$ is included is relatively modest (Table 4.5).

Table 4.5 Regression coefficients of the linear elastic amplification model [Equation (4.7)].

T (sec)	a_1	Z^* (m)	b	σ_{lnAF} (without $Z_{1.0}$)	σ_{lnAF} (with $Z_{1.0}$)
1.0	-0.63	121	0.70	0.20	0.20
2.0	-0.75	292	0.71	0.19	0.17
5.0	-0.63	490	1.16	0.18	0.16
10.0	-0.44	1000	0.76	0.06	0.05

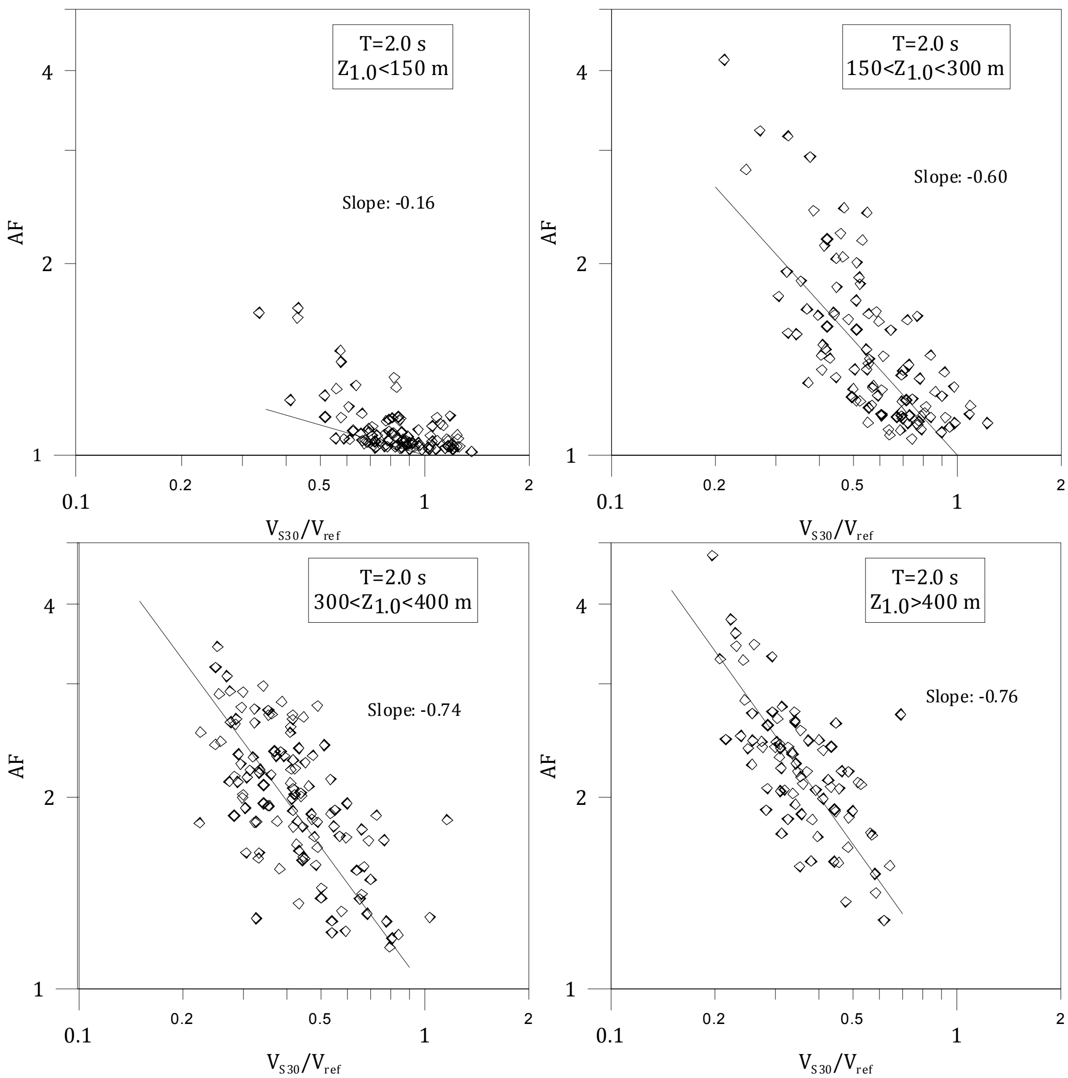

Figure 4.14 Amplification factor versus V_{S30}/V_{ref} at T = 2.0 sec for four different bins of $Z_{1.0}$.

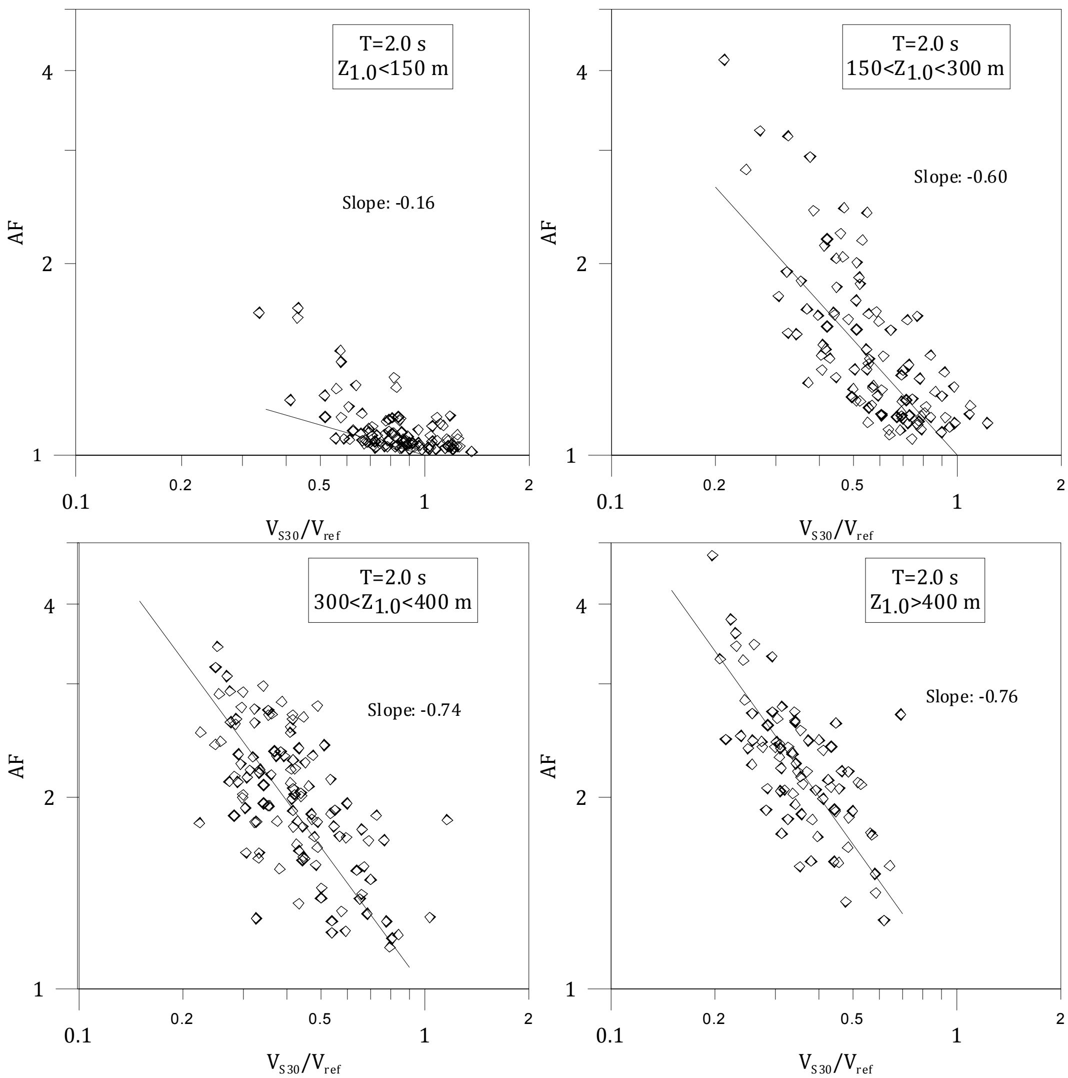

Figure 4.14 Amplification factor versus V_{S30}/V_{ref} at T = 2.0 sec for four different bins of $Z_{1.0}$.

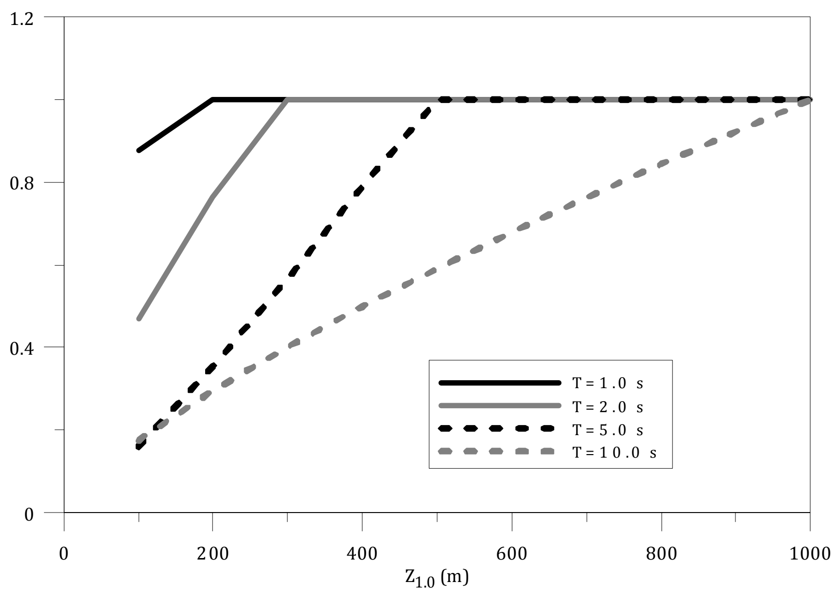

Figure 4.15 Variation of α with $Z_{1.0}$ for different periods.

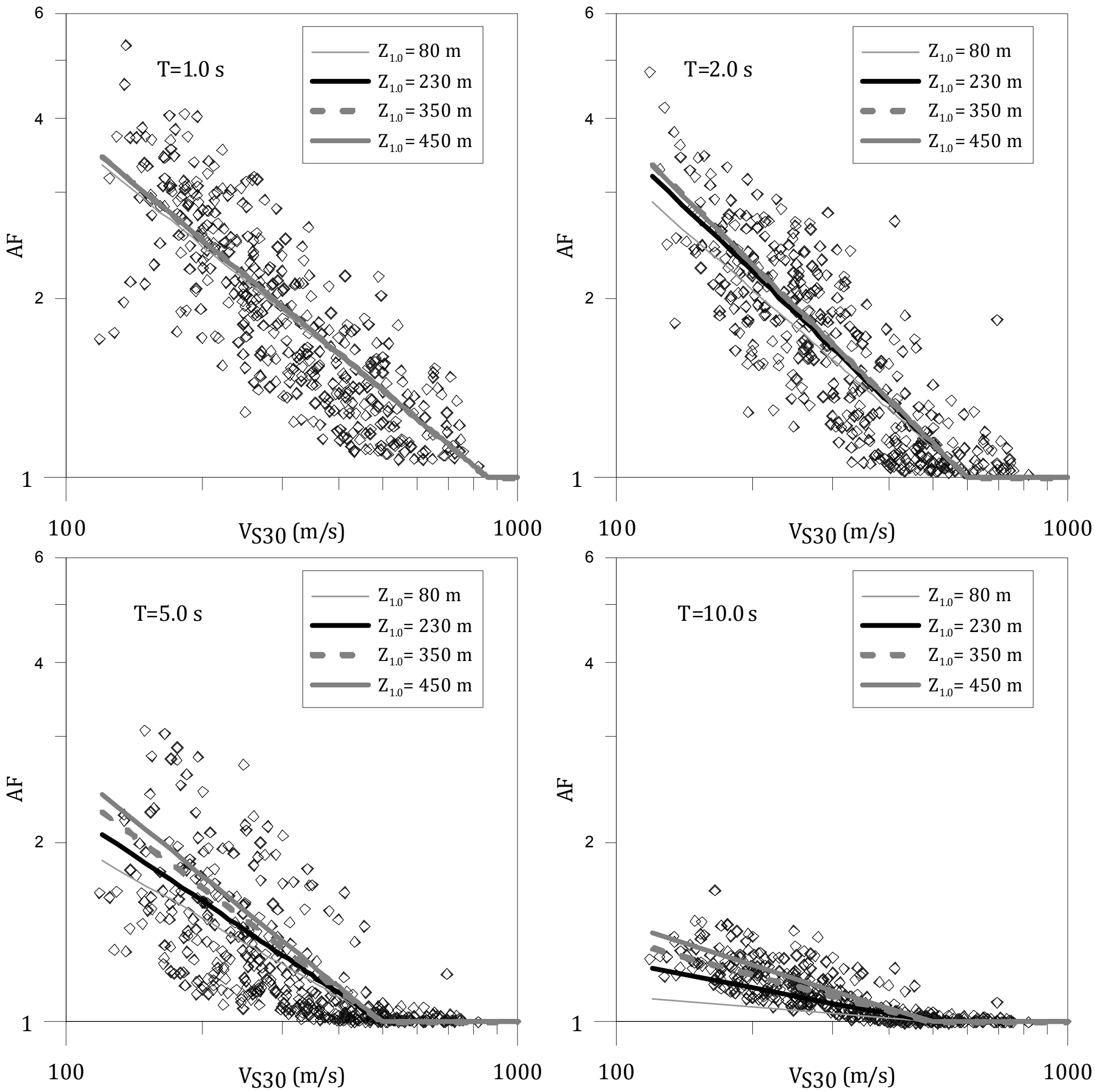

Figure 4.16 Model predictions for different values of $Z_{1.0}$.

5 Models for Nonlinear Site Amplification

5.1 INTRODUCTION

Next, we develop the nonlinear component of the site amplification models. A functional form for shorter periods that includes the effects of V_{S30}, V_{ratio}, and $S_{a,rock}$ will be presented, and a functional form for longer periods will be presented that includes V_{S30} and $S_{a,rock}$.

5.2 V_{S30} COMPONENT OF THE NONLINEAR SITE AMPLIFICATION MODEL

The nonlinear component of the soil amplification model includes the effects of soil nonlinearity at high intensity shaking such that the amplification changes with increasing input shaking intensity. The nonlinear effect can be modeled using a functional form represented by:

$$\ln(\mathrm{AF})_{nl} = b_1 \cdot \ln\left(\frac{S_{a,rock} + c}{c}\right) \tag{5.1}$$

where $S_{a,rock}$ is the spectral acceleration for rock conditions at the spectral period of interest, and b_1 and c are regression coefficients. This functional form was used by Chiou and Youngs [2008] in their GMPE.

It is helpful to consider how parameters b_1 and c control the variation of AF with shaking intensity (i.e., $S_{a,rock}$). Coefficient c essentially represents the $S_{a,rock}$ level in the middle of transition from linear behavior (i.e., where AF does not vary with $S_{a,rock}$) to nonlinear behavior (i.e., where AF does vary with $S_{a,rock}$). Coefficient b_1 represents the degree of nonlinearity in terms of the logarithmic change in AF with a logarithmic increase in the level of shaking. Generally, b_1 is negative such that an increase in $S_{a,rock}$ results in a decrease in AF. A more negative value of b_1 indicates a stronger reduction in AF with $S_{a,rock}$ (i.e., more nonlinearity), and as b_1 approaches zero the site amplification approaches the linear elastic condition. The degree of nonlinearity is a function of the stiffness of the site; with softer sites experiencing more nonlinearity. Therefore, b_1 is a function of V_{S30}.

Figure 5.1 shows AF versus $S_{a,rock}$ as predicted by the Chiou and Youngs [2008] model at periods of PGA, 0.2 sec, and 0.5 sec, and for three different V_{S30} values (150 m/sec, 300 m/sec and 500 m/sec). Also shown are the locations of coefficient c for each period (c is not taken V_{S30} dependent in the Chiou and Youngs [2008] model) and a representative slope (b_1) at larger $S_{a,rock}$.

At each of the spectral periods, nonlinearity is stronger at smaller values of V_{S30}. At large values of V_{S30} (e.g., V_{S30} = 500 m/sec in Figure 5.1), the reduction of AF with increasing $S_{a,rock}$ is insignificant, indicating more linear behavior for stiff sites. The coefficient c, which is the shaking level where there is a transition from linear to nonlinear behavior, is close to 0.1*g* at PGA and 0.5 sec, while it is higher (0.25*g*) at a spectral period of 0.2 sec.

To investigate the dependency of AF on $S_{a,rock}$ and the factors that influence this relationship, the computed AF values for the randomized site profiles subjected to 10 different input intensities were considered. Amplifications of the soil profiles at short and long periods are considered separately in the next sections.

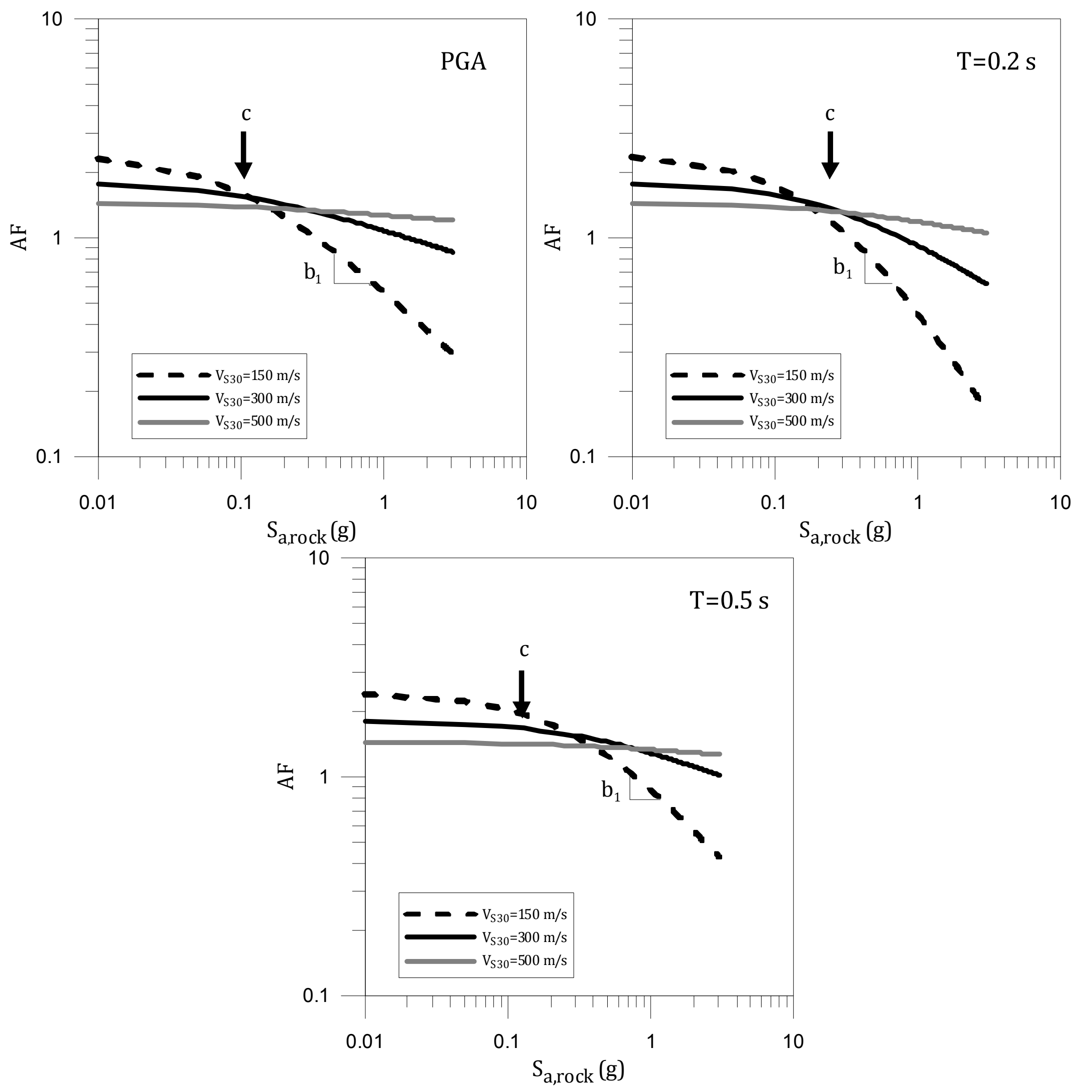

Figure 5.1 Amplification versus $S_{a,rock}$ as predicted by the Chiou and Youngs [2008] GMPE.

Building upon previous work, the nonlinear AF model was developed from Equation (5.1). The dependence of the slope b_1 on V_{S30} was investigated by separating the AF data into the same eight V_{S30} bins used in Chapter 4 (V_{S30}<150 m/sec, 150 m/sec<V_{S30}<200 m/sec, 200 m/sec <V_{S30}<250 m/sec, 250 m/sec <V_{S30}<300 m/sec, 300 m/sec <V_{S30}<350 m/sec, 350 m/sec <V_{S30}<450 m/sec, 450 m/sec <V_{S30}<550 m/sec, and 550 m/sec <V_{S30}<750 m/sec). Figure 4.2 shows plots of AF versus $S_{a,rock}$ for PGA for the eight bins of V_{S30}. At the smaller V_{S30} values, amplification almost immediately starts to decrease as $S_{a,rock}$ increases from 0.01*g*. At larger V_{S30} (i.e., greater than about 300 m/sec) AF remains relatively constant at $S_{a,rock}$ levels less than about 0.1*g* but then decreases as $S_{a,rock}$ increases beyond 0.1*g*. At the largest V_{S30} values, AF does not vary significantly over the $S_{a,rock}$ values analyzed.

To identify the variation of b_1 with V_{S30}, a linear relationship is fit between the logarithm of AF in each V_{S30} bin and the logarithm of $S_{a,rock}$, using only AF data from $S_{a,rock}$ >0.1*g* in each bin. Only data with $S_{a,rock}$ larger than 0.1*g* is considered because b_1 represents the slope at larger input intensities. The slope of the linear relationship (b_1) is shown in Figure 5.2 and varies across the V_{S30} bins, with larger V_{S30} values displaying smaller slopes. For T = 0.2 sec and 0.5 sec (Figures 4.3 and 4.4, respectively) a similar trend is observed with the slope decreasing with increasing V_{S30}. Figure 4.5 plots the derived values of b_1 versus the median V_{S30} of each bin for periods of PGA, 0.2, and 0.5 sec. The data for all three periods show b_1 as approximately constant at smaller V_{S30} and then decreasing towards zero as V_{S30} increases. Above some value of V_{S30}, b_1 tends to remains constant.

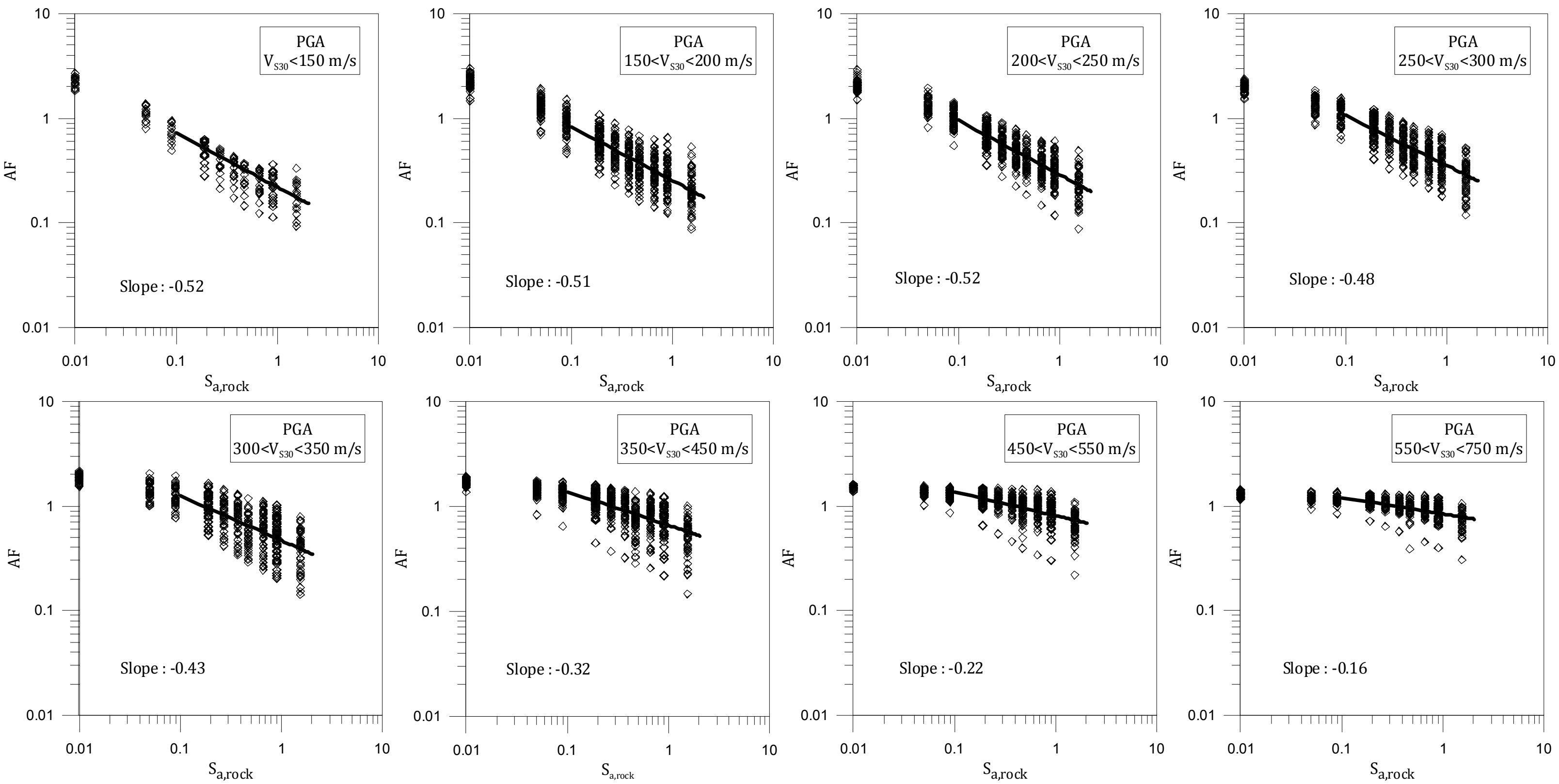

Figure 5.2 Amplification factor for PGA versus $S_{a,rock}$ for different V_{S30} bins.

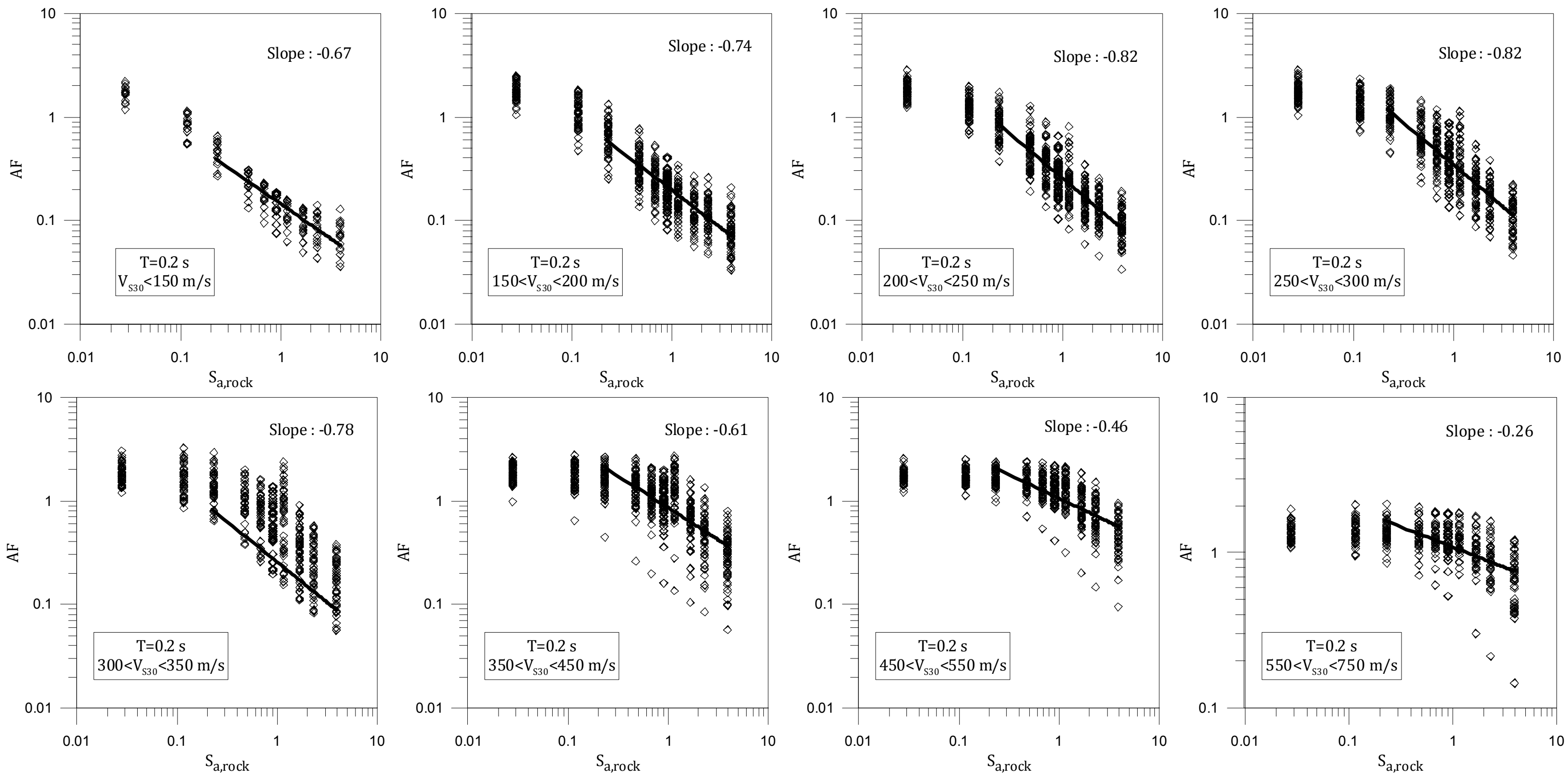

Figure 5.3 **Amplification factor for T = 0.2 sec versus $S_{a,rock}$ for different V_{S30} bins.**

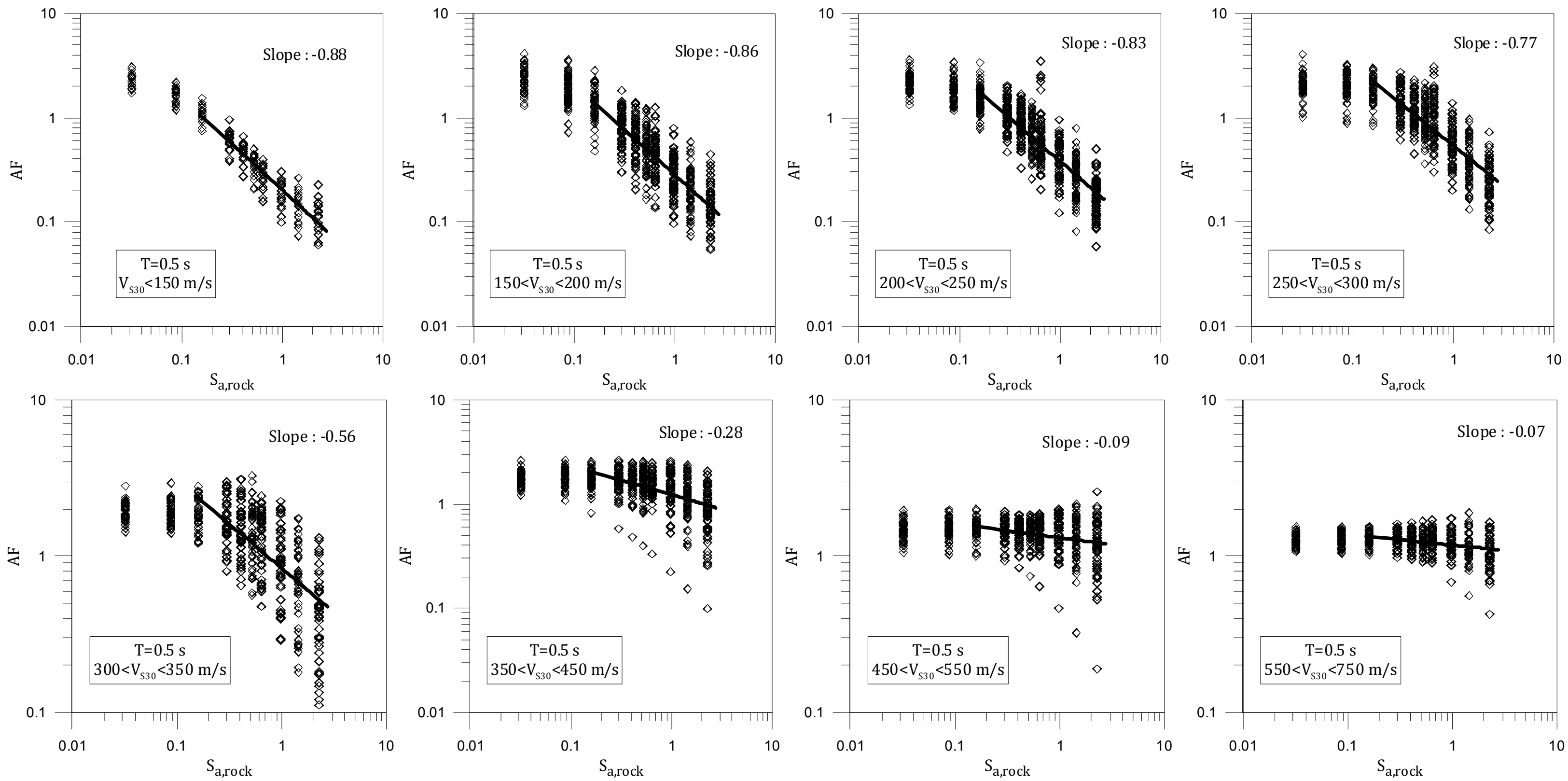

Figure 5.4 Amplification factor for T = 0.5 sec versus $S_{a,rock}$ for different V_{S30} bins.

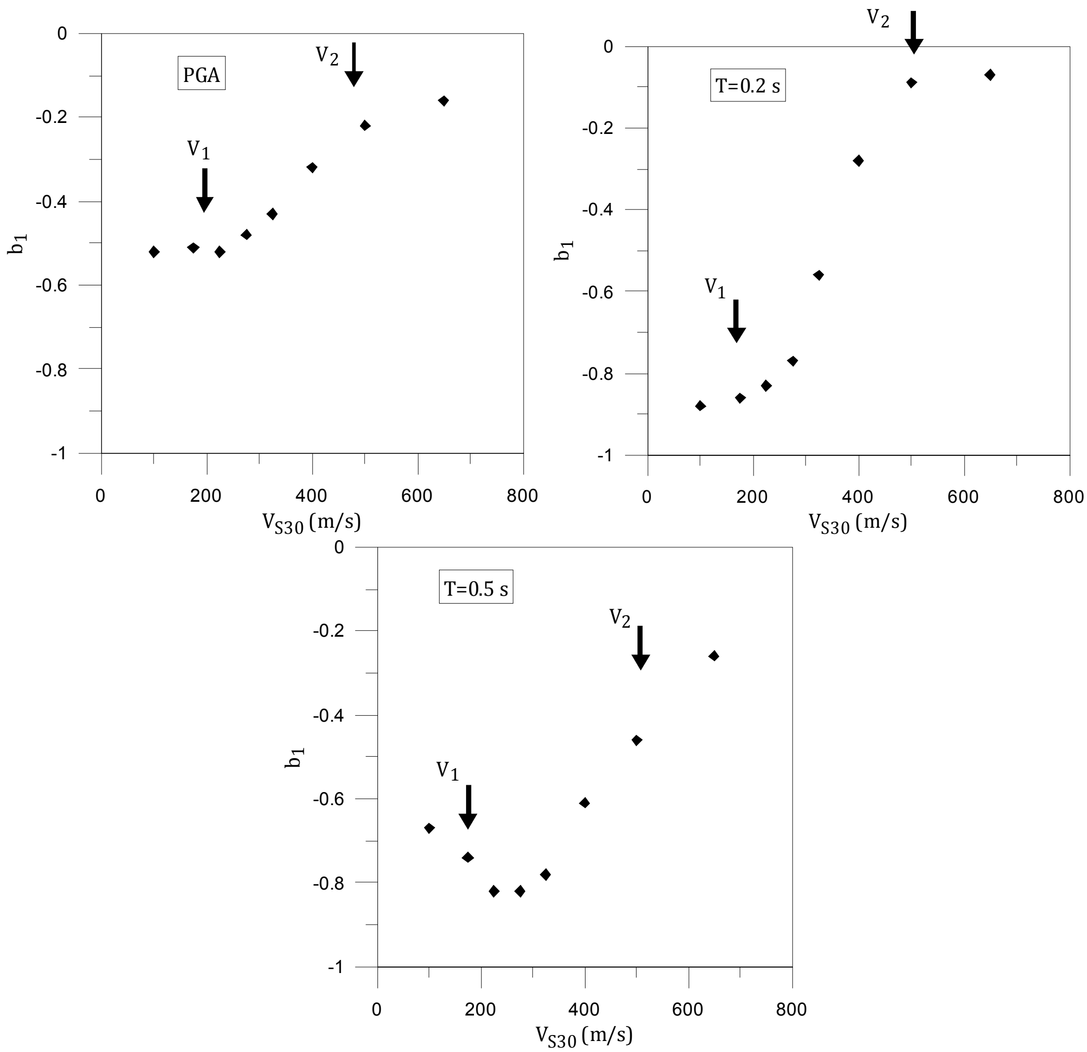

Figure 5.5 Computed b_1 for eachV_{S30} bin versus median V_{S30} of each bin (PGA, T = 0.2 sec and 0.5 sec).

Using the trends in Figure 5.5, an expression is developed that describes the slope b_1 as a function of V_{S30}. This expression models b_1 as decreasing log-linearly between V_{S30} values of V_1 and V_2, remaining constant outside of these values. The V_{S30} below which b_1 stays constant is V_1, and the value above which b_1 stays constant is V_2. b_{o1} and b_{o2} are the values of the slope for V_{S30} less than V_1 and greater than V_2 , respectively. The resulting expression is given by:

$$b_1 = \begin{cases} b_{o1}, V_{S30} \leq V_1 \\ b_{o1} + \dfrac{b_{o2} - b_{o1}}{\ln\left(\dfrac{V_2}{V_1}\right)} \cdot \ln\left(\dfrac{V_{S30}}{V_1}\right), V_1 < V_{S30} \leq V_2 \\ b_{o2}, V_{S30} > V_2 \end{cases} \tag{5.2}$$

V_1, V_2, b_{o1}, and b_{o2} are regression coefficients that are period dependent. This expression is incorporated into the final form of the nonlinear amplification model.

5.3 V_{ratio} COMPONENT OF THE NONLINEAR SITE AMPLIFICATION MODEL

Chapter 4 demonstrated that V_{ratio} influences the linear-elastic amplification of soil sites at shorter periods. Including V_{ratio} into the linear-elastic model reduced the standard deviation by 10 to 30%. The V_{ratio} effect modeled in the linear elastic amplification model will be present at larger intensities, but V_{ratio} may also influence the nonlinear amplification. The AF data in Figures 5.2 through 5.4 clearly show that the scatter in the AF data increases as input intensity increases. Based on the observations at small input intensities, it is likely that V_{ratio} influences the computed values of AF at large input intensities.

To investigate the influence of V_{ratio} on the nonlinear component of the site amplification model, AF is plotted versus the normalized V_{ratio} (V_{ratio} /1.4) for each bin of V_{S30} and input intensity. A linear relationship is fit to the ln(AF) versus ln(V_{ratio} /1.4) for each $S_{a,rock}$ to identify if the slope of this relationship (i.e., regression parameter a_3 from Chapter 4) changes with $S_{a,rock}$. Figures 5.6 through 5.8 show plots of PGA amplification versus V_{ratio} /1.4 for V_{S30} bins of <150 m/sec, 250–350 m/sec and 550–750 m/sec, respectively. The slope of the log-linear fit for each of the V_{S30} bins generally increases with $S_{a,rock}$. The slope, which indicates how strongly V_{ratio} affects AF for a given V_{S30}, can increase by more than a factor of two as $S_{a,rock}$ increases from 0.01*g* to 0.9*g*. For the larger V_{S30} values (Figure 5.8), the slope increases from 0.0 (i.e., no V_{ratio} effect) at $S_{a,rock} = 0.01g$ to 0.4 at $S_{a,rock} = 0.9g$.

The slope of the linear fit between ln(AF) and ln(V_{ratio} /1.4), which represents parameter a_3 in the linear-elastic model of Chapter 4, is plotted versus normalized -$S_{a,rock}$ (i.e., $S_{a,rock}/S_{a,rock\text{-}min}$, where $S_{a,rock\text{-}min}$ is the smallest input rock intensity considered) in Figure 5.9 for all eight V_{S30} bins. Since a_3 is V_{S30} dependent; Figure 5.9 allows us to investigate whether the increase in a_3 with $S_{a,rock}$ is also V_{S30} dependent. The data in Figure 5.9 show that a_3 increases linearly with $\ln(S_{a,rock}/S_{a,rock\text{-}min})$ for all V_{S30} bins at PGA. The linear trend between a_3 and ln ($S_{a,rock}/S_{a,rock\text{-}min}$) is quite strong, and the slope of that relationship varies between 0.05 and 0.15, with most of the values between 0.07 and 0.09. The computed slopes are plotted versus V_{S30} in Figure 5.10. The variation of the slope with V_{S30} is not systematic; therefore, the slope is considered to be independent of V_{S30}.

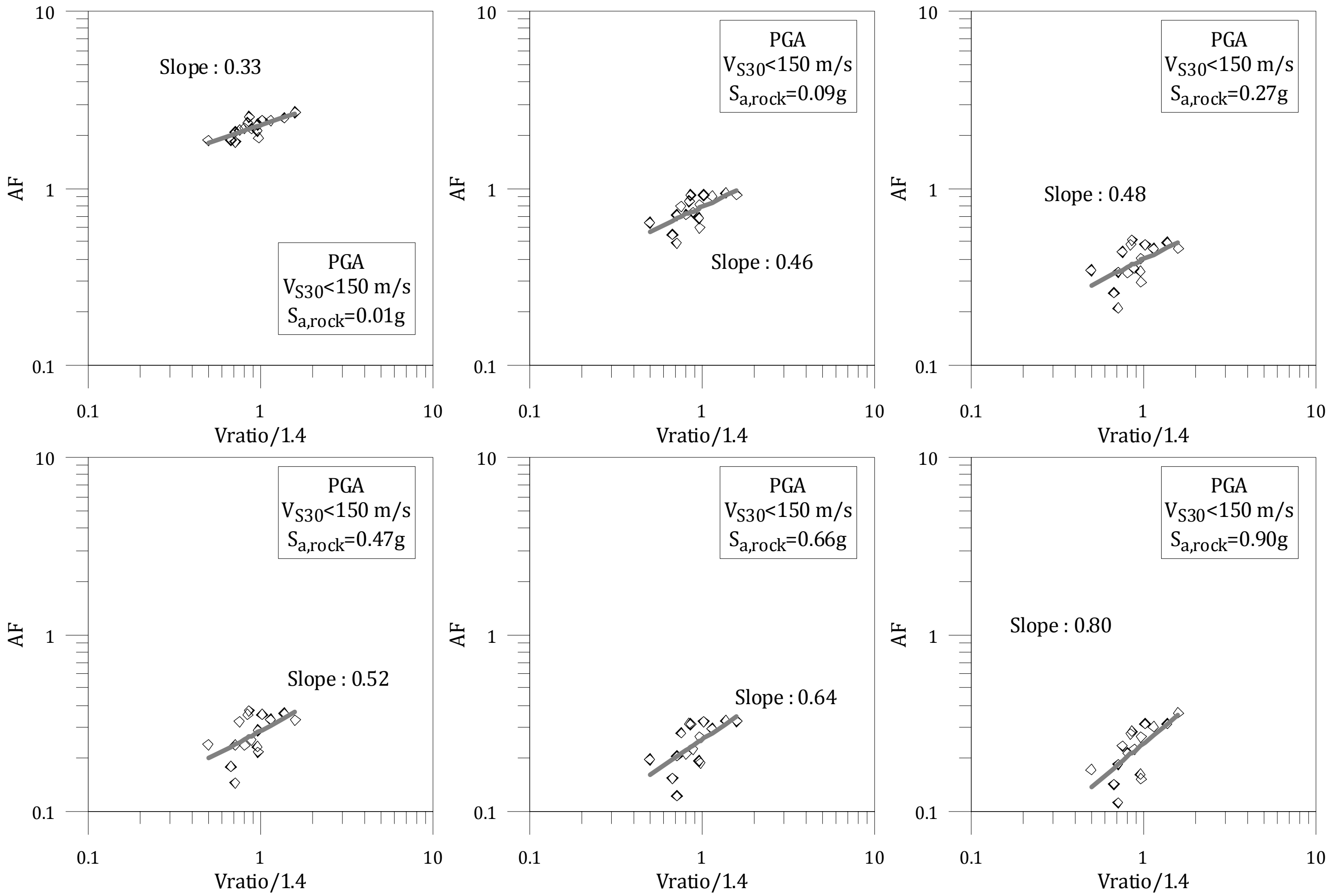

Figure 5.6 Amplification factor for PGA versus normalized V_{ratio} for V_{S30} < 150 m/sec.

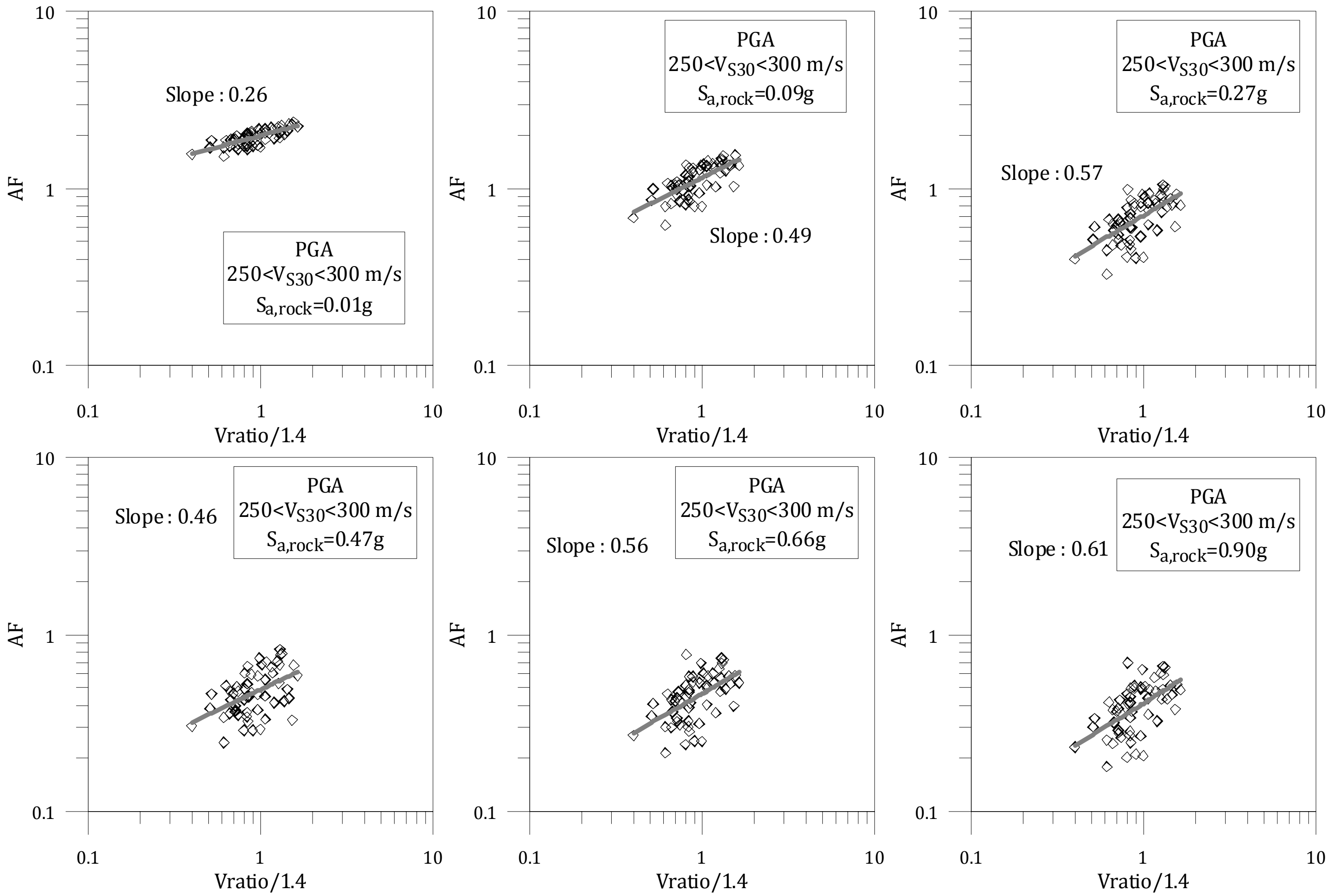

Figure 5.7 Amplification factor for PGA versus normalized V_{ratio} for 250 < V_{S30} < 300 m/sec.

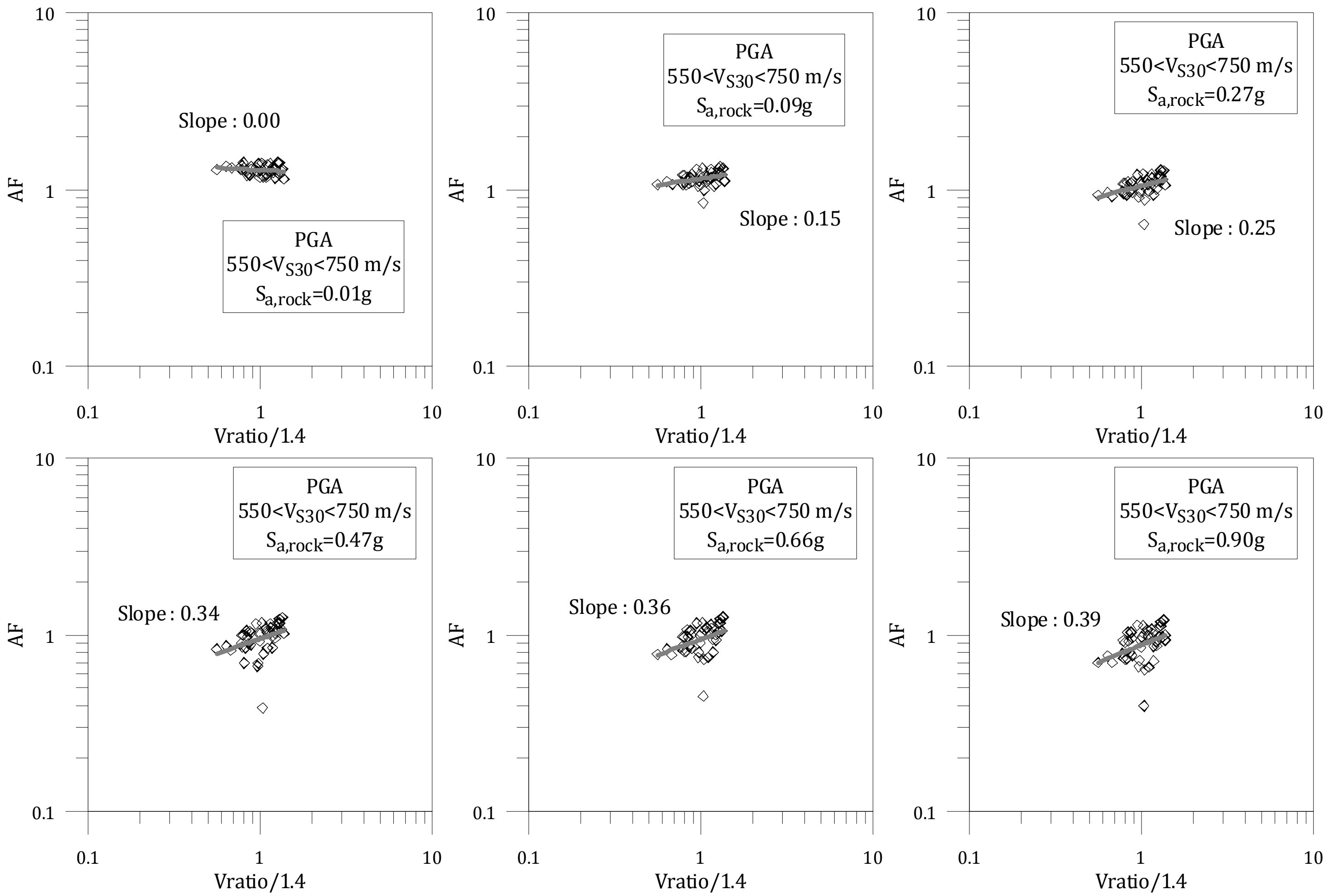

Figure 5.8 Amplification factor for PGA versus normalized V_{ratio} for 550 < V_{S30} < 750 m/sec.

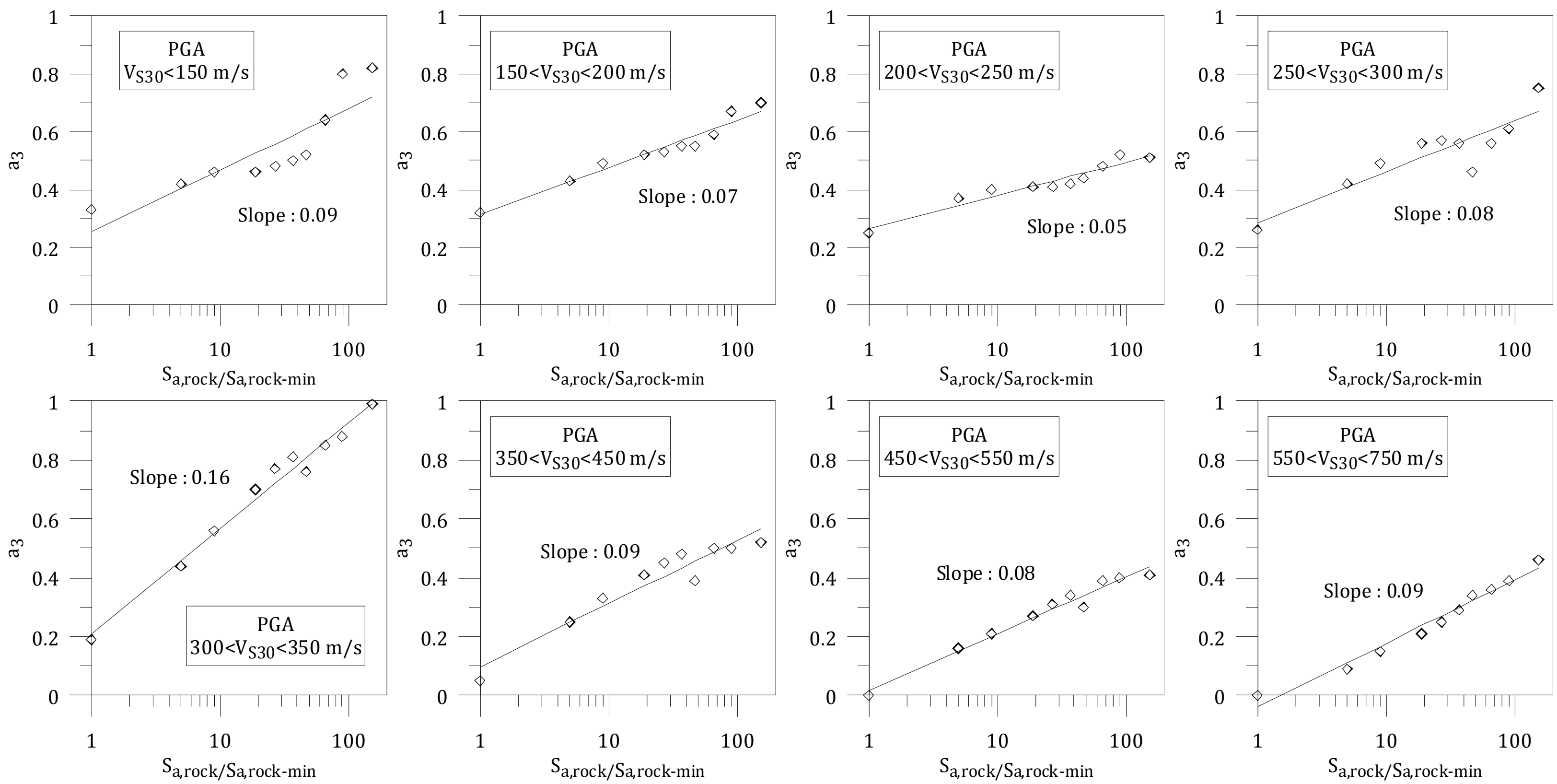

Figure 5.9 The slope of linear fit between ln(AF) and ln(V_{ratio}/1.4) versus ln($S_{a,rock}$ /$S_{a,rock\text{-}min}$) for PGA.

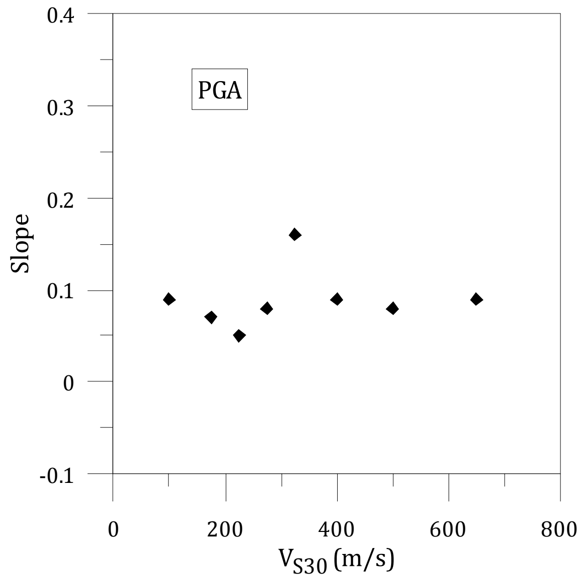

Figure 5.10 The slope of the relationship between a_3 and $\ln(S_{a,rock}/S_{a,rock\text{-}min})$ versus V_{S30} for PGA.

Generally, the trends shown for PGA are similar for other short periods (i.e., ≤ 0.5 sec), Figure 5.11 plots the slope of the a_3 versus $\ln(S_{a,rock}/S_{a,rock\text{-}min})$ relationship versus V_{S30} for these other periods. Again, the slope varies with V_{S30} but not in a systematic manner; therefore, the slope is modeled as V_{S30} independent for all of the short periods.

The data presented indicate that the V_{ratio} effect, previously modeled in the linear elastic case as $a_3 \cdot \ln(V_{ratio}/1.4)$ with a_3 being V_{S30} dependent, is intensity dependent. The full V_{ratio} effect can be written as:

$$\ln(\mathrm{AF})_{V_{ratio}} = \left[a_3 + b_2 \cdot \ln\left(\frac{S_{a,rock}}{S_{a,rock-min}}\right)\right] \cdot \ln\left(\frac{V_{ratio}}{1.4}\right) \tag{5.3}$$

Where a_3 represents the V_{ratio} effect under linear elastic conditions, as presented in Chapter 4, and $b_2 \cdot \ln\left(\frac{S_{a,rock}}{S_{a,rock-min}}\right)$ models the effect of input intensity on the V_{ratio} effect. The parameter b_2 represents the slopes shown in Figures 5.9; this parameter does not vary with V_{S30} based on the data shown in Figures 5.10 and 5.11. To maintain the separation of AF under linear elastic conditions from the AF under nonlinear conditions, the second component in Equation (5.3) is added to the nonlinear amplification model. Additionally, to ensure that the nonlinear amplification model disappears at small input intensities, the smallest $S_{a,rock}$ that can be used in Equation (5.3) is $S_{a,rock\text{-}min}$. Based on the above considerations, the nonlinear component of the site amplification model can be written as:

$$\ln(\mathrm{AF})_{nl} = b_1 \cdot \ln\left(\frac{S_{a,rock} + c}{c}\right) + b_2 \cdot \ln\left[\frac{\max(S_{a,rock}, S_{a,rock-min})}{S_{a,rock-min}}\right] \cdot \ln\left(\frac{V_{ratio}}{1.4}\right) \tag{5.4}$$

where b_1 is V_{S30} dependent, as described by Equation (5.2), and the coefficient b_2 is V_{S30} independent.

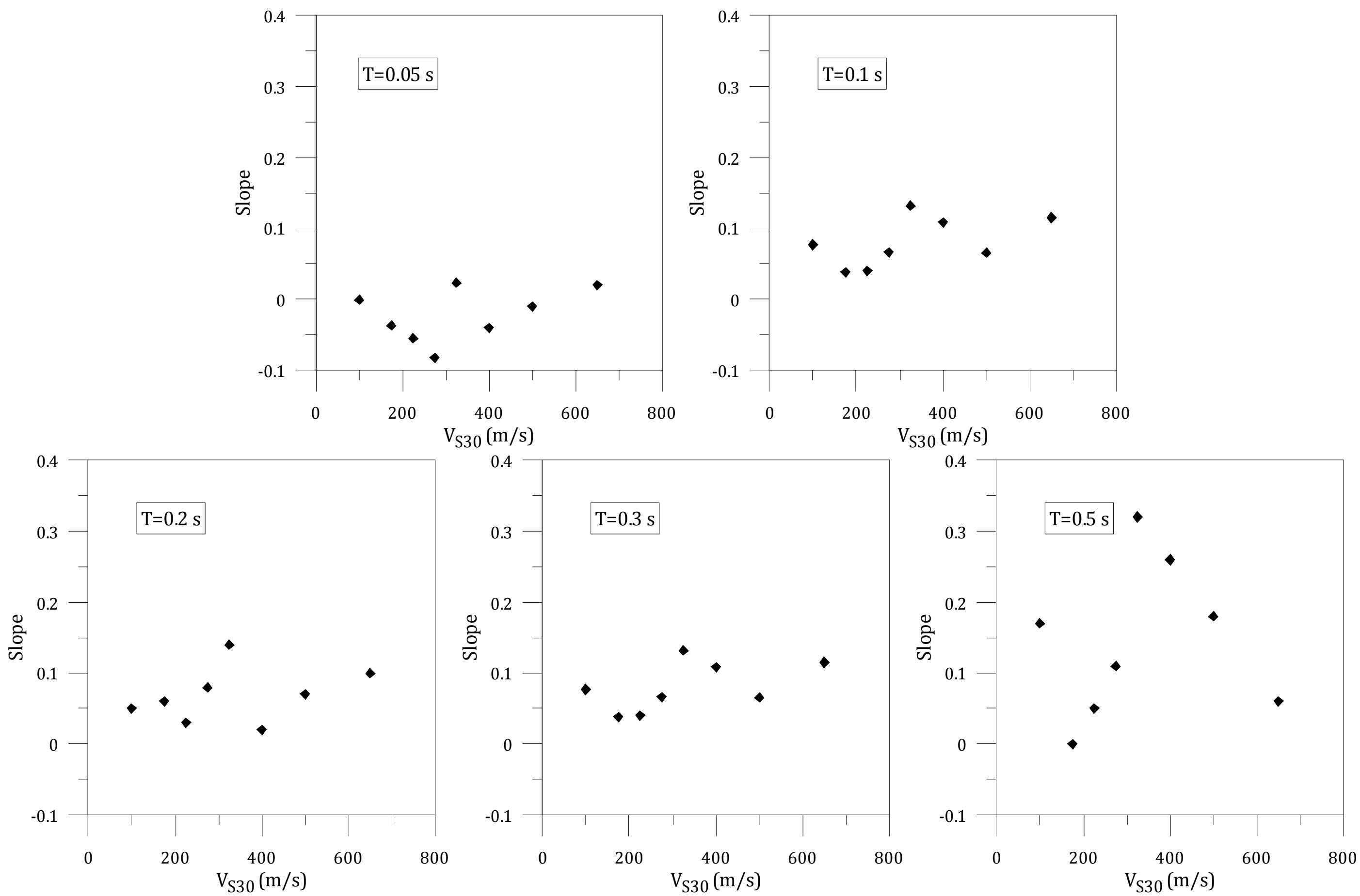

Figure 5.11 The variation of the slope of the linear fit between a_3 and $\ln(S_{a,rock}/S_{a,rock\text{-}min})$ with V_{S30} at T = 0.05, 0.1, 0.2, 0.3, and 0.5 sec.

5.4 NONLINEAR SITE AMPLIFICATION AT LONG PERIODS

To investigate the dependency of amplification on input intensity at long periods, AF is plotted versus $S_{a,rock}$ for bins of V_{S30} at the four long periods considered. Figures 5.12 and 5.13 show AF versus $S_{a,rock}$ for two select representative periods: T = 1.0 sec and 5.0 sec, respectively. At T = 1.0 sec, AF decreases with increasing input intensity ($S_{a,rock}$) for smaller V_{S30} but the AF remains constant or slightly increases for larger V_{S30} (i.e., greater than about 350 m/sec in Figure 5.12). At T = 5.0 sec (Figure 5.13), amplification generally increases as $S_{a,rock}$ increases for smaller V_{S30}, indicating that the b_1 slope may be positive at long periods. At larger values of V_{S30}, the amplification becomes insensitive to input intensity (slope ~ 0.0) similar to the results for T = 1.0 sec. A positive value of b_1 is technically justified for T = 5.0 sec because most sites have natural periods shorter than 5.0 sec, and the soil nonlinearity induced by large input intensities will cause period lengthening towards 5.0 sec. This lengthening will cause an increase in amplification with increasing input intensity at this period. Sites with larger V_{S30} tend to have natural periods much shorter than 5.0 sec and they strain less as $S_{a,rock}$ increases, making the effect of period lengthening minimal.

The slope of the ln(AF)-ln($S_{a,rock}$) relationship at larger values of $S_{a,rock}$ (which represents b_1) are computed for each V_{S30} bin and are shown in Figures 5.12 and 5.13. Figure 5.14 plots the derived values of b_1 versus the median V_{S30} of each bin for periods of 1.0 sec and 5.0 sec. Figure 5.14 shows that b_1 is constant at smaller V_{S30}; it varies linearly with increasing V_{S30}, and then becomes constant again at larger V_{S30}. For T = 1.0 sec, b_1 is equal to –0.8 at smaller V_{S30} and approaches 0.0 at V_{S30} greater than about 400 m/sec. For T = 5.0 sec, b_1 is about 0.2 for smaller V_{S30} and approaches 0.0 at V_{S30} greater than about 500 m/sec. A positive value of b_1 indicates that AF increases with increasing $S_{a,rock}$, and positive values are observed for periods greater than and equal to 2.0 sec.

Based on the data presented in Figure 5.14, the same functional form that is used at short periods to describe the variation b_1 with V_{S30} can be used at longer periods (Equation 5.2). This relationship defines regions of constant b_1 at smaller and larger V_{S30} values, and a linear relationship with ln(V_{S30}) at V_{S30} values in between. The parameters to be determined by regression are the V_{S30} values above and below which b_1 is a constant (V_2 and V_1), and the b_1 values above and below these values (b_{o2} and b_{o1}).

Chapter 4 demonstrated that the site amplification at long periods is not influenced by V_{ratio}, but that it is influenced by $Z_{1.0}$. The effect of $Z_{1.0}$ on soil amplification is not affected by soil nonlinearity; therefore the model for the effect of $Z_{1.0}$ does not include input intensity (i.e., $S_{a,rock}$). Additionally, the NGA models that include $Z_{1.0}$ [Abrahamson and Silva 2008; Chiou and Youngs 2008] also found the influence of $Z_{1.0}$ to be intensity independent.

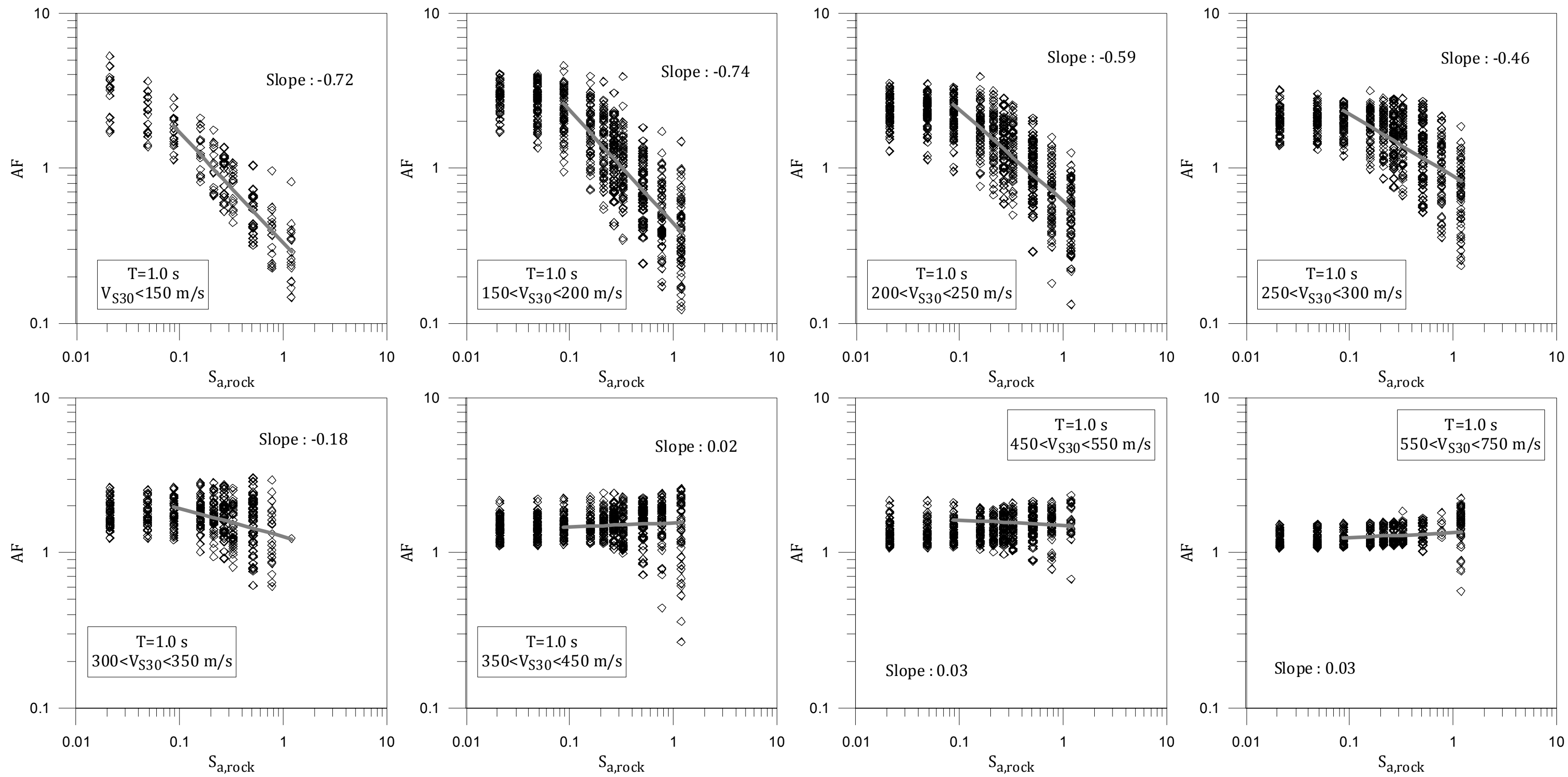

Figure 5.12 Amplification for T = 1.0 sec versus $S_{a,rock}$ for different V_{S30} bins.

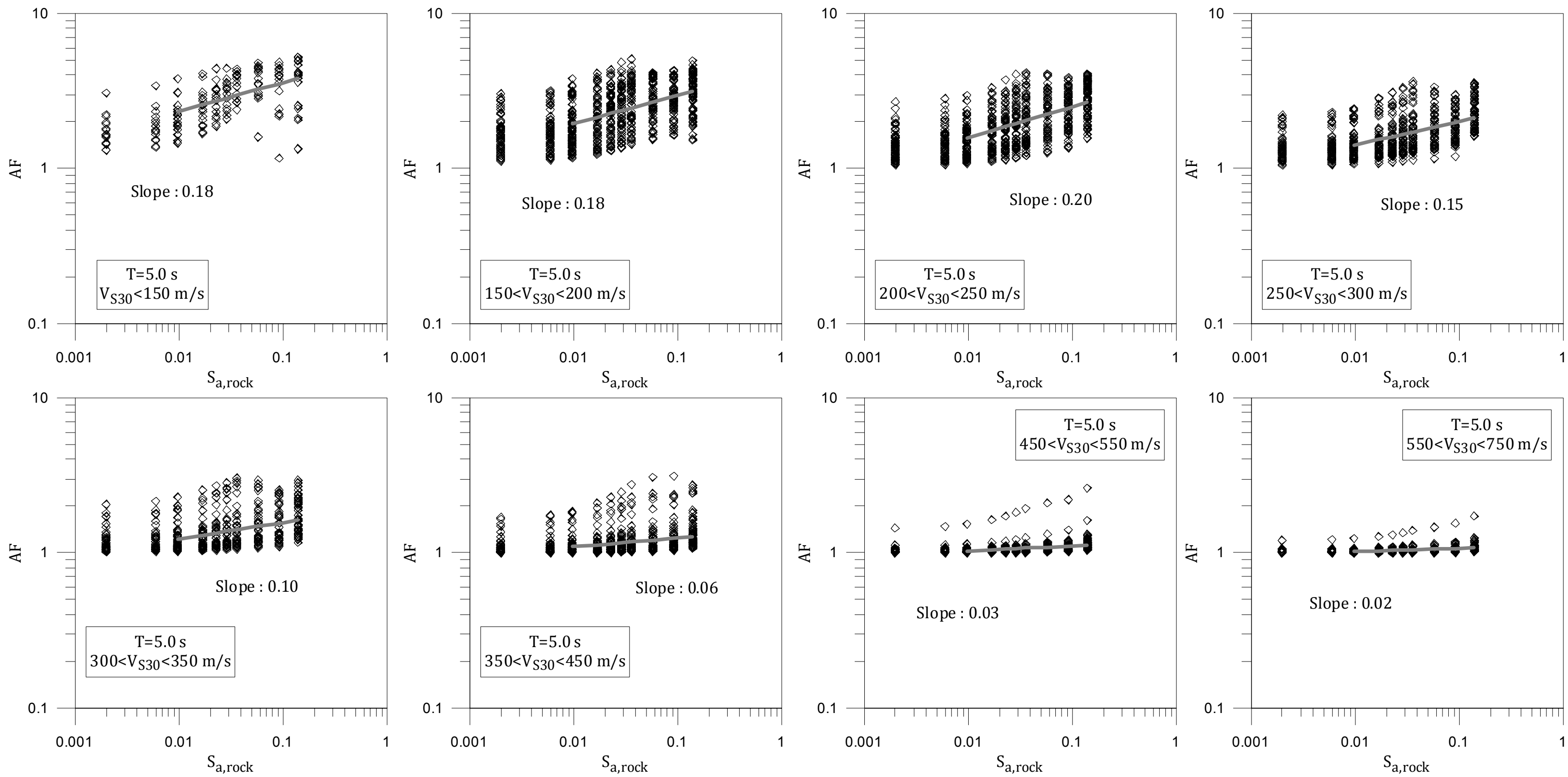

Figure 5.13 Amplification for T = 5.0 sec versus $S_{a,rock}$ for different V_{S30} bins.

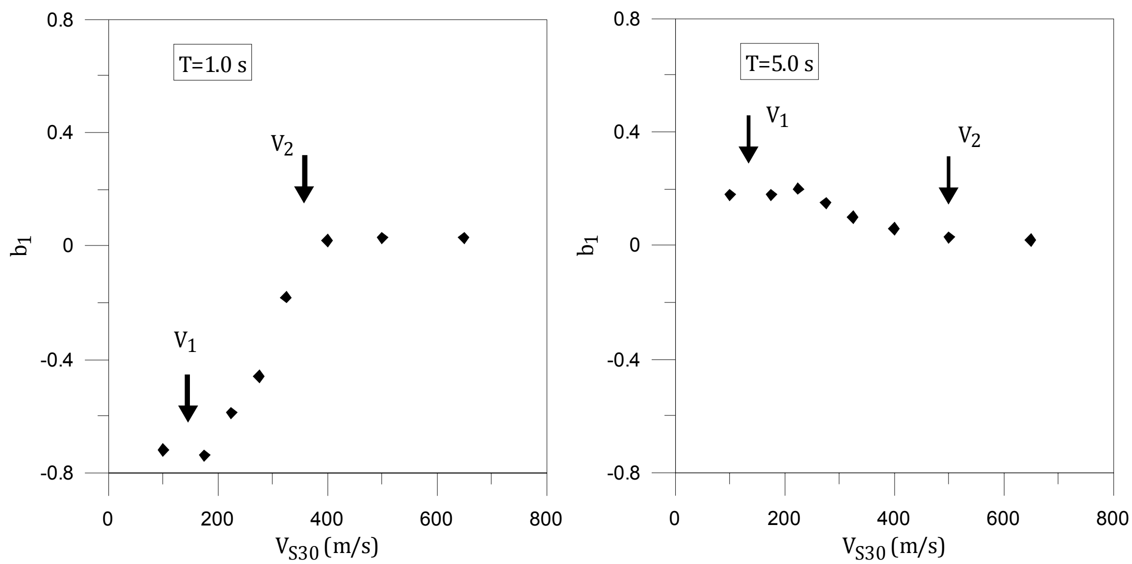

Figure 5.14 b_1 versus median V_{S30} of each bin at T = 1.0 sec and 5.0 sec.

6 Final Site Amplification Model

6.1 INTRODUCTION

The linear and nonlinear components of the site amplification model presented in Chapters 4 and 5 are combined and summarized in this chapter. Separate functional forms are fitted to the amplification data for short and long periods. To demonstrate the fit of the developed model, the amplification data are plotted along with predictions from the developed models. The calculated residuals from the developed functional forms are plotted versus the independent variables in the site amplification model. Finally, the influence of V_{ratio} on predicted acceleration response spectra is demonstrated.

6.2 SITE AMPLIFICATION MODEL FOR SHORT PERIODS

Combining the linear-elastic and nonlinear components of the site amplification model for short periods, the following model is proposed for the amplification factor for spectral accelerations at short periods ($T \leq 0.5$ sec):

If $\mathrm{V_{S30}} < \mathrm{V_{ref}}$:

$$\ln(\mathrm{AF}) = \mathrm{a_1} \cdot \ln\left(\frac{\mathrm{V_{S30}}}{\mathrm{V_{ref}}}\right) + \mathrm{a_2} \cdot \left[\ln\left(\frac{\mathrm{V_{S30}}}{\mathrm{V_{ref}}}\right)\right]^2 + \mathrm{a_3} \cdot \ln\left(\frac{V_{\mathrm{ratio}}}{1.4}\right) + \mathrm{b_1} \cdot \ln\left(\frac{\mathrm{S_{a,rock}+c}}{\mathrm{c}}\right) + \mathrm{b_2} \cdot \ln\left[\frac{\max\left(\mathrm{S_{a,rock}}, \mathrm{S_{a,rock-min}}\right)}{\mathrm{S_{a,rock-min}}}\right] \cdot \ln\left(\frac{\mathrm{V_{ratio}}}{1.4}\right) \tag{6.1a}$$

If $\mathrm{V_{S30}} \geq \mathrm{V_{ref}}$:

$$\ln(\mathrm{AF}) = \mathrm{b_1} \cdot \ln\left(\frac{\mathrm{S_{a,rock}+c}}{\mathrm{c}}\right) + \mathrm{b_2} \cdot \ln\left[\frac{\max\left(\mathrm{S_{a,rock}}, \mathrm{S_{a,rock-min}}\right)}{\mathrm{S_{a,rock-min}}}\right] \cdot \ln\left(\frac{\mathrm{V_{ratio}}}{1.4}\right) \tag{6.1b}$$

This model is fit independently to each short period. The parameters a_3 and b_1 are V_{S30} dependent, and the V_{S30} dependencies are described by:

$$a_3 = \begin{cases} a_0, V_{S30} \leq V_a \\ a_0 - \dfrac{a_0}{(V_b - V_a)} \cdot (V_{S30} - V_a), V_a < V_{S30} \leq V_b \\ 0, V_{S30} > V_b \end{cases} \tag{6.2}$$

$$b_1 = \begin{cases} b_{o1}, V_{S30} \leq V_1 \\ b_{o1} + \dfrac{b_{o2} - b_{o1}}{\ln\left(\frac{V_2}{V_1}\right)} \cdot \ln\left(\dfrac{V_{S30}}{V_1}\right), V_1 < V_{S30} \leq V_2 \\ b_{o2}, V_{S30} > V_2 \end{cases} \tag{6.3}$$

The regression process is executed in three steps. Each step uses the maximum likelihood method for regression. In the first step, the coefficients for the linear-elastic component are estimated (i.e., a_1, a_2, a_0, V_a, V_b) using the AF data from the lowest intensity input motions (i.e., $PGA_{rock} = 0.01g$). These parameters are kept fixed in subsequent steps. In the second step, the parameters for the nonlinear model (b_{o1}, b_{o2}, V_1, V_2, and c) are estimated excluding the effect of V_{ratio} (i.e., b_2) using the AF data for all input intensities. To ensure that the nonlinear component of the model does not influence the computed amplification at small $S_{a,rock}$, a minimum value of c was set to $0.1g$. If $c = 0.1g$, then the $\ln\left(\frac{S_{a,rock}+c}{c}\right)$ term is equal to 0.095 for $S_{a,rock} = 0.01g$. Thus, the nonlinear effect on the computed amplification is minimal. In the last and final step, all previously parameters are fixed and b_2 (i.e., the V_{ratio} effect in the nonlinear model) is computed. The final estimated values of all coefficients for the six short periods studied here are listed in Table 6.1.

Figure 6.1 shows the residuals [i.e., ln(data)-ln(predicted)] plotted versus V_{S30}, $S_{a,rock}$, and V_{ratio} for the amplification factors for PGA. The residuals indicate overprediction in amplification (negative residuals) for smaller V_{S30} and a slight overprediction over all V_{S30} (overall average residual equal to –0.07). There is no systematic trend between the residuals and the various parameters. However the variability in the residuals increases with the increase of $S_{a,rock}$. For all the other considered short periods, the residuals also do not show a systematic trend with any of independent variables in the model; however, the average residual across these other periods range from about -0.07 to +0.08.

It is difficult to fully evaluate the model looking at the overall residuals, therefore AF predictions are plotted versus $S_{a,rock}$ along with the AF data in the next several figures. To demonstrate the effects of V_{S30} and V_{ratio} on the AF predictions, the predicted AF values are plotted versus $S_{a,rock}$ for select V_{S30} bins and for a range of V_{ratio} values. As discussed previously, the range of V_{ratio} values is slightly different among the V_{S30} bins, but most of the values fall between 0.8 and 2.5. Considering these ranges, AF predictions are shown for $V_{ratio} = 0.8$, 1.4, and 2.5 in Figures 6.2 to 6.7 for the six periods considered.

Table 6.1 Regression coefficients of the site amplification model for short periods.

	PGA	0.05 sec	0.1 sec	0.2 sec	0.3 sec	0.5 sec
a_1	-0.69	-0.70	-0.76	-0.9	-0.89	-0.67
a_2	-0.13	-0.15	-0.21	-0.32	-0.28	-0.10
a_0	0.34	0.38	0.38	0.44	0.57	0.39
V_a (m/sec)	176	130	110	414	100	100
V_b (m/sec)	481	513	737	726	750	750
b_{o1}	-0.91	-1.26	-0.98	-1.21	-1.93	-2.60
b_{o2}	-0.24	-0.21	-0.19	-0.16	-0.14	-0.11
V_1 (m/sec)	184	118	192	188	133	103
V_2 (m/sec)	454	581	583	557	530	447
c	0.1	0.1	0.1	0.21	0.37	0.4
b_2	0.09	0.08	0.08	0.07	0.08	0.06
V_{ref} (m/sec)	1000	1000	1000	1000	1000	1000
$S_{a,rock-min}$ (g)	0.01	0.01	0.02	0.03	0.03	0.03

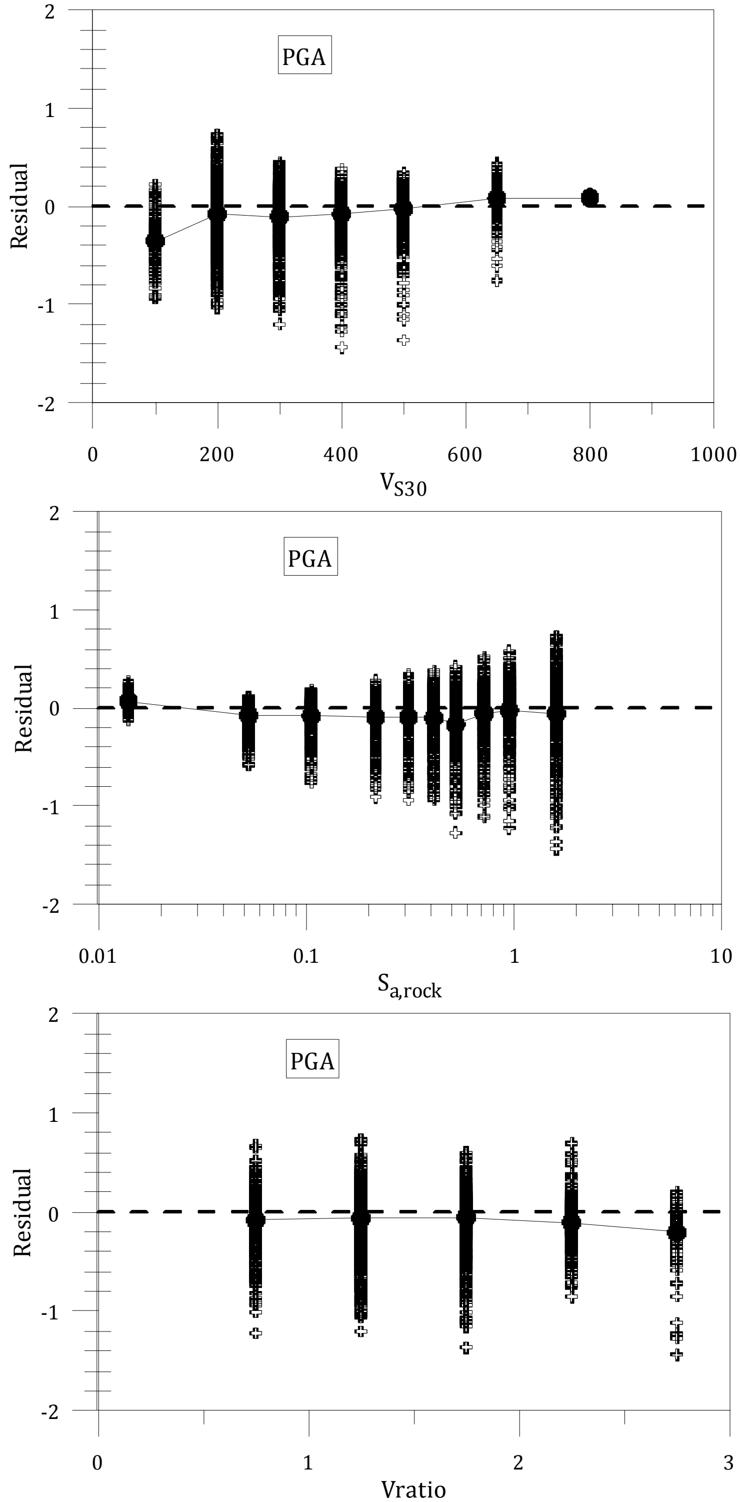

Figure 6.1 Model residuals for PGA versus V_{S30}, $S_{a,rock}$, and V_{ratio}.

The predictions in Figures 6.2 through 6.7 are in general agreement with the data. Additionally, sites with larger values of V_{ratio} have larger amplification and sites with smaller V_{ratio} have smaller amplification. This effect helps explain some of the scatter shown in the AF data. The effect of V_{ratio} at low input intensity (i.e., smallest $S_{a,rock}$) is strongest for the smaller values of V_{S30} and essentially non-existent for larger V_{S30} (greater than about 350 m/sec). However, the input intensity effect modeled with V_{ratio} results in V_{ratio} becoming important for larger V_{S30} at larger input intensities (note the predictions for V_{S30} = 450–550 m/sec in Figures 6.2 to 6.7).

While there is general agreement between the model predictions and data shown in Figures 6.2 through 6.7, there are some areas of deviation. Note that at the smallest input intensity and the smallest V_{S30} values, the AF predictions tend to be smaller than observed for T ≤ 0.2 sec. This result is due to the parameter c being small (~ 0.1*g*) relative to the smallest $S_{a,rock}$ used in this study (0.01*g*) and the large, negative values of b_1 for small V_{S30} sites. As a result, the nonlinear component of the amplification model contributes to the AF prediction even for $S_{a,rock}$ ~ 0.01*g*. This issue is not apparent at periods of 0.3 and 0.5 sec because the parameter c is larger (Table 6.1). Another challenging area is amplification for the larger V_{S30} values (450–550 m/sec) at periods of 0.1 and 0.2 sec. The model tends to underpredict the amplification at moderate $S_{a,rock}$ and overpredicts amplification at larger AF. This issue again appears to be due to c being relatively small and the model for the V_{S30}-dependence for b_1.

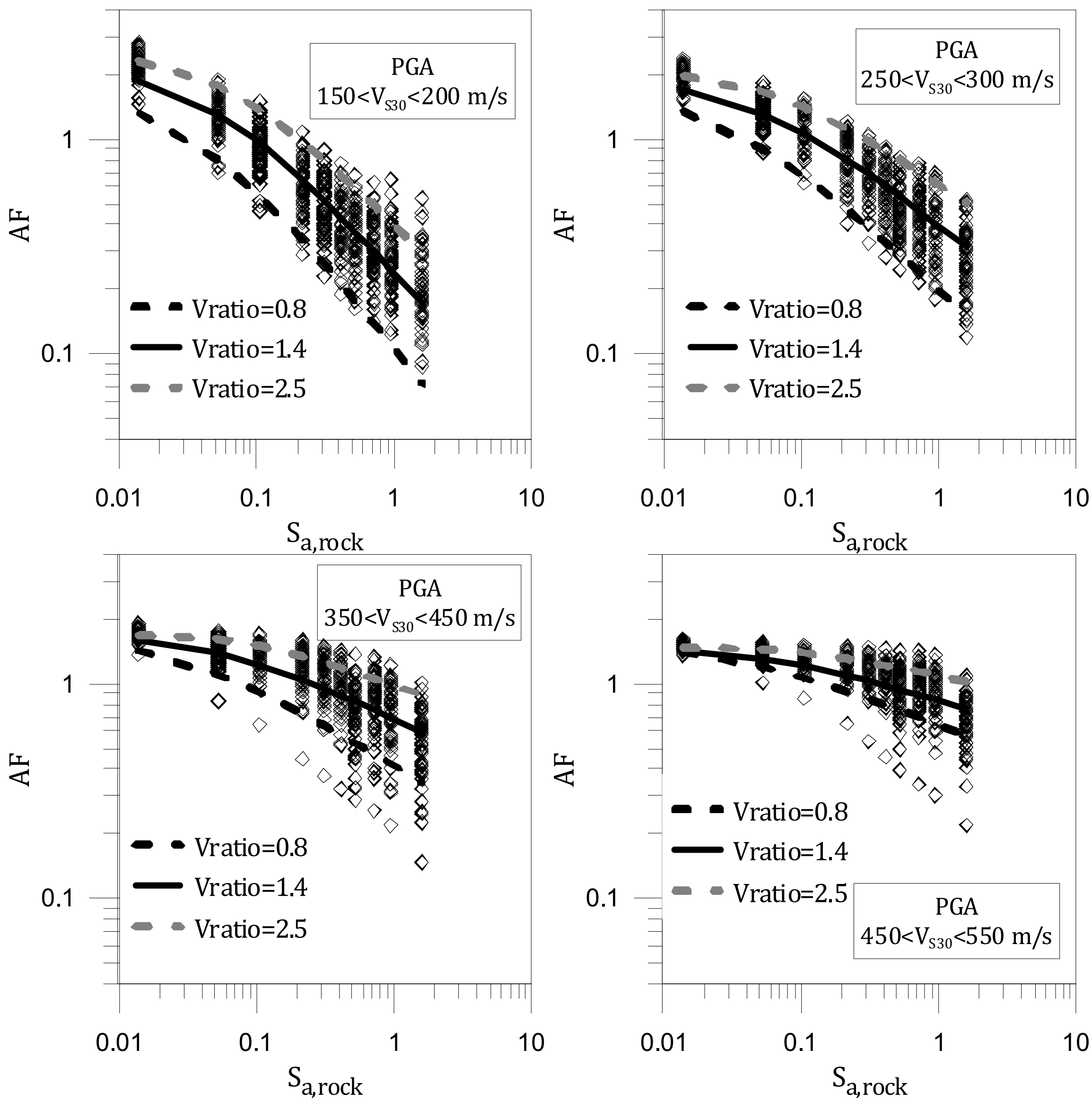

Figure 6.2 **Amplification factor for PGA versus $S_{a,rock}$ and model predictions for different values of V_{ratio}.**

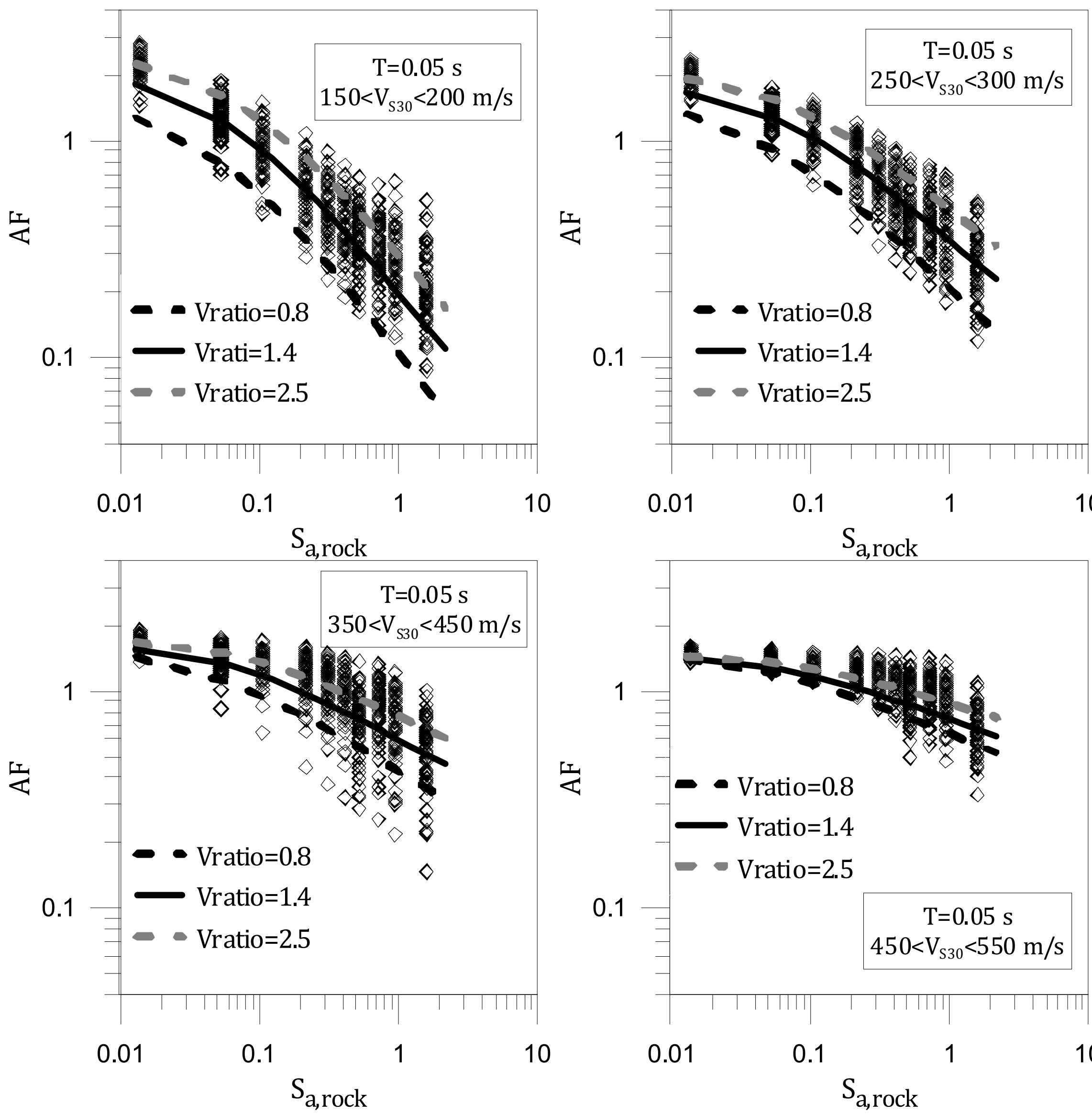

Figure 6.3 Amplification factor for T = 0.05 sec versus $S_{a,rock}$ and model predictions for different values of V_{ratio}.

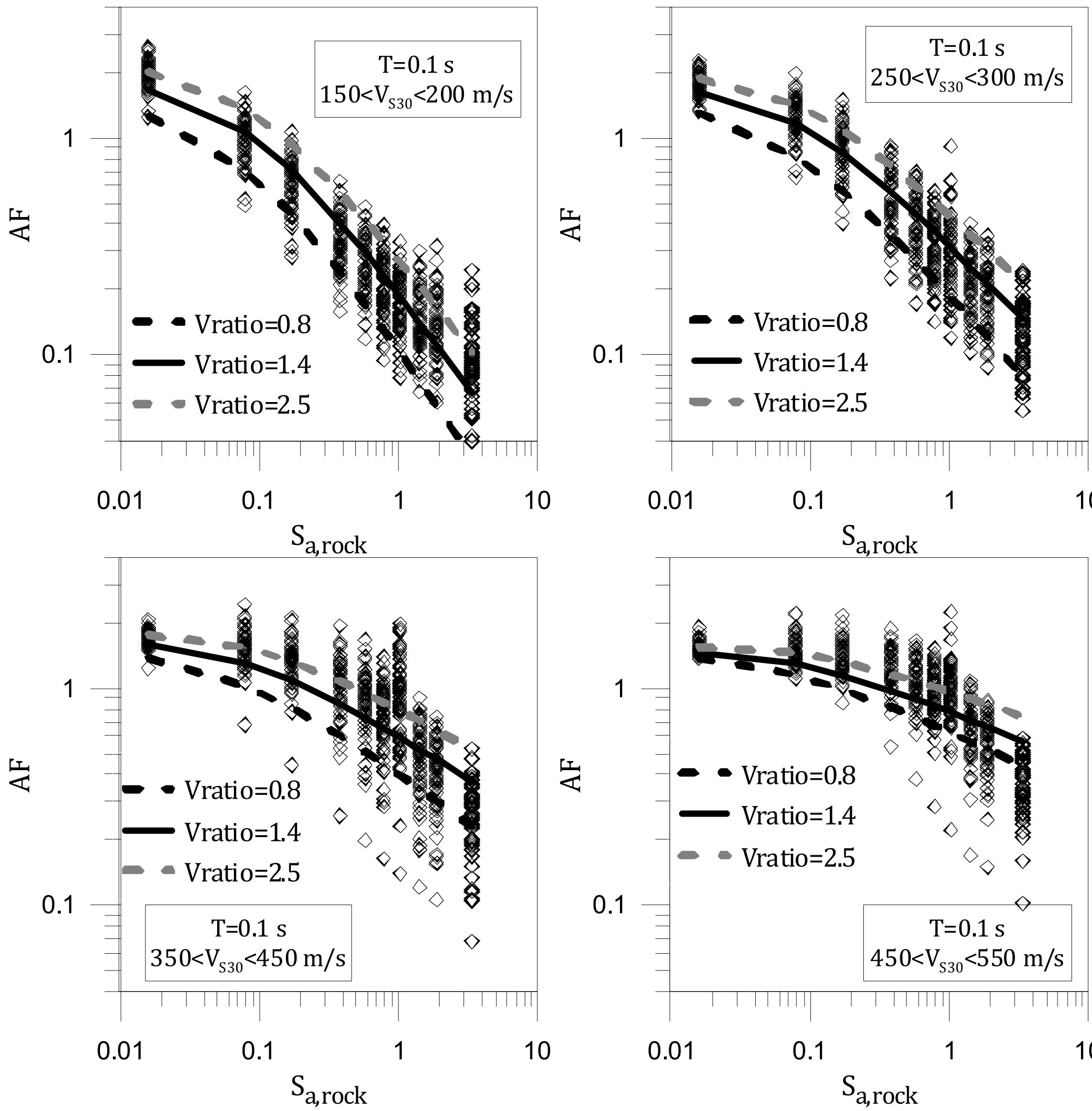

Figure 6.4 **Amplification factor for T = 0.1 sec versus $S_{a,rock}$ and model predictions for different values of V_{ratio}.**

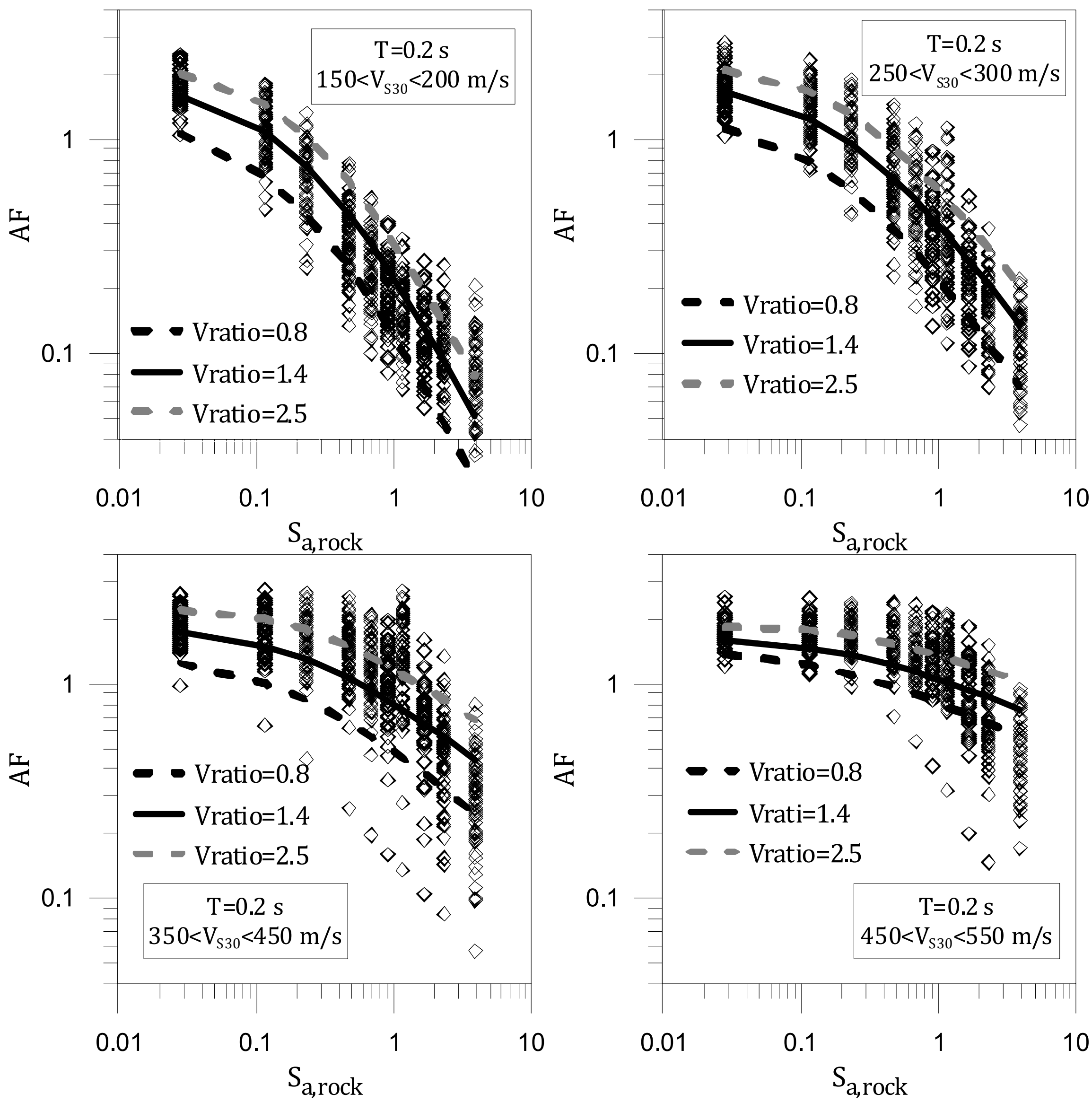

Figure 6.5 **Amplification factor for T = 0.2 sec versus $S_{a,rock}$ and model predictions for different values of V_{ratio}.**

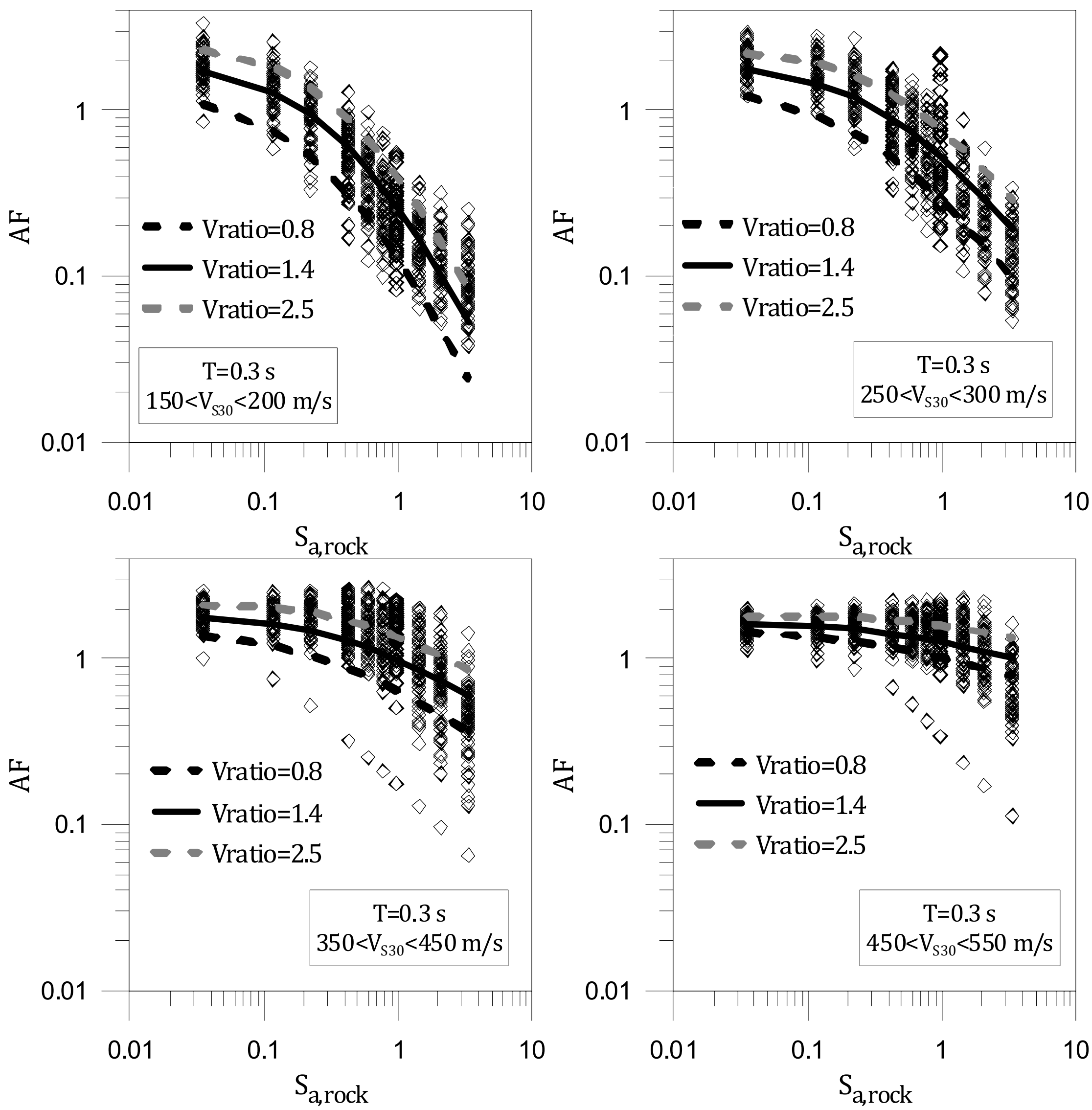

Figure 6.6 **Amplification factor for T = 0.3 sec versus $S_{a,rock}$ and model predictions for different values of V_{ratio}.**

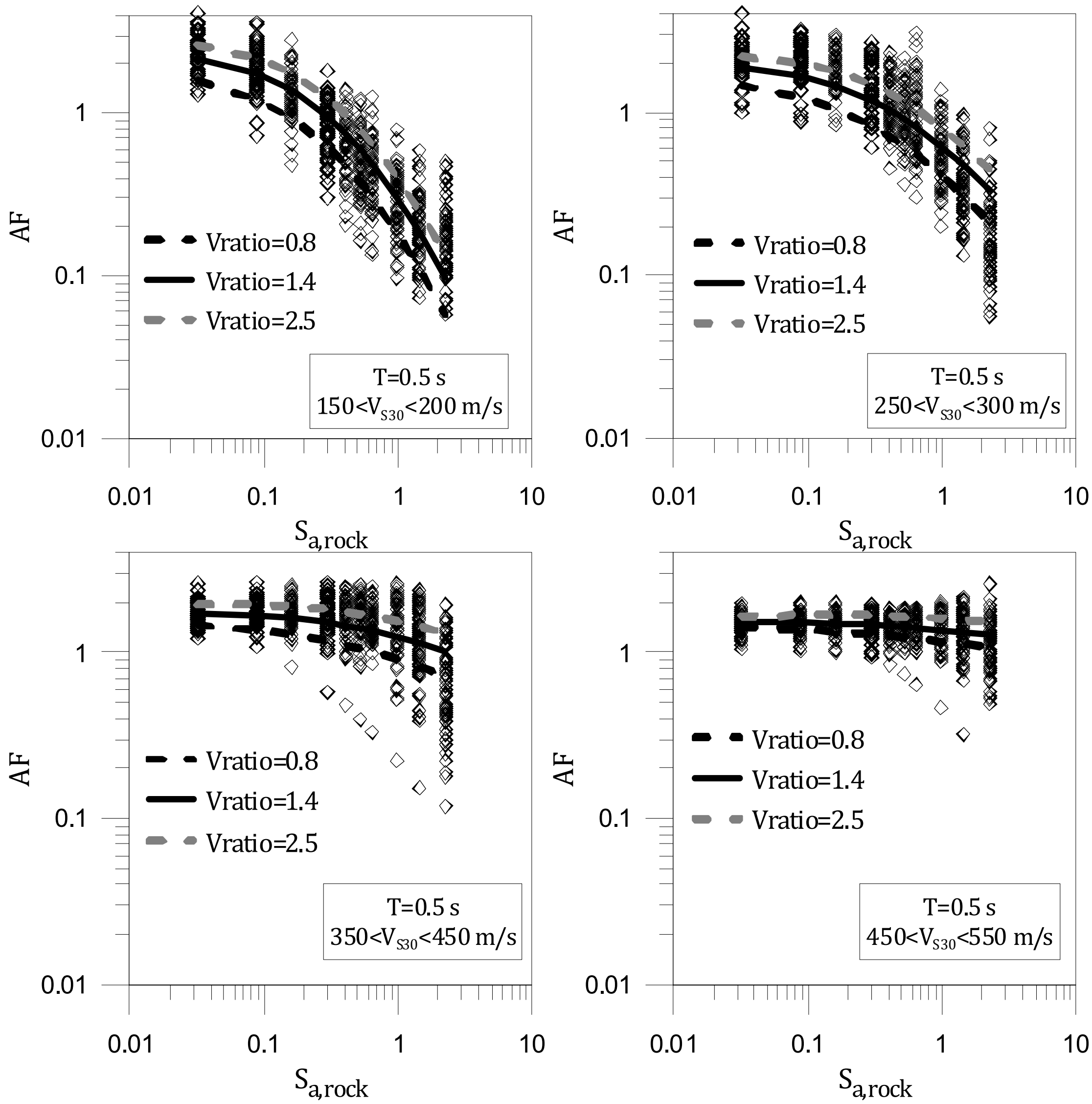

Figure 6.7 **Amplification factor for T = 0.5 sec versus $S_{a,rock}$ and model predictions for different values of V_{ratio}.**

To evaluate the effect of adding V_{ratio} to the full amplification model, the standard deviation of the residuals [i.e., ln(data)-ln(predicted)] for models with and without including V_{ratio} is computed. The standard deviations (i.e., σ_{lnAF}) are listed in Table 6.2 for each period. The standard deviation of the full model decreases when including V_{ratio} (in most cases from about 8 to 15%), however the level of reduction is not as significant as it was for the linear elastic model

(Chapter 4). The modest reduction in $\sigma_{\ln AF}$ may be influenced by the strength of ln(AF)-ln(V_{ratio}) relationship at larger input intensities. Considering the data from Chapter 5 shown in Figures 5.6 through 5.8, the strength of the AF–V_{ratio} relationship decreases with increasing input intensity.

In addition to the standard deviation of the residuals, the models with and without V_{ratio} can be compared through the parameter R^2_{M1-M2}, defined as :

$$R^2_{M1-M2} = \frac{\sum(\mathrm{Residual_{M1}})^2 - \sum(\mathrm{Residual_{M2}})^2}{\sum(\mathrm{Residual_{M1}})^2} \quad (6.4)$$

where $\sum(\mathrm{Residual_{M1}})^2$ is the sum of the squared residuals from Model 1 (i.e., the model that does not include V_{ratio}) and $\sum(\mathrm{Residual_{M2}})^2$ is the sum of the squared residuals from Model 2 (i.e., the model that includes V_{ratio}). The calculated R^2_{M1-M2} values for each period are also listed in Table 6.2. The R^2_{M1-M2} values range from 0.08 to 0.33, indicating that V_{ratio} model explains 8 to 33% of the variation that exists in the non-V_{ratio} model At a spectral period of 0.2 sec, the calculated R^2_{M1-M2} reaches its maximum value of 33%.

Table 6.2 $\sigma_{\ln AF}$ **and** R^2_{M1-M2} **of the site amplification models with and without** V_{ratio}**.**

T (sec)	$\sigma_{\ln AF}$ model without V_{ratio}	$\sigma_{\ln AF}$ model with V_{ratio}	% Reduction	R^2_{M1-M2}
PGA	0.28	0.25	11	0.08
0.05	0.30	0.25	17	0.19
0.1	0.36	0.32	11	0.19
0.2	0.45	0.37	18	0.33
0.3	0.41	0.36	12	0.19
0.5	0.39	0.36	8	0.11

6.3 SITE AMPLIFICATION MODEL FOR LONG PERIODS

Combining the linear-elastic and nonlinear components of the amplification model for long periods, the following model is proposed for the amplification factor for spectral accelerations at long periods (T ≥ 1.0 sec):

If $V_{S30} < V_{ref}$:

$$\ln(AF) = a_1 \cdot \alpha \cdot \ln\left(\frac{V_{S30}}{V_{ref}}\right) + b_1 \cdot \ln\left(\frac{S_{a,rock} + c}{c}\right) \tag{6.5a}$$

If $V_{S30} \geq V_{ref}$:

$$\ln(AF) = b_1 \cdot \ln\left(\frac{S_{a,rock} + c}{c}\right) \tag{6.5b}$$

with α and b_1 defined as:

$$\alpha = \left[\frac{\min(Z^*, Z_{1.0}) + 1}{Z^* + 1}\right]^b \tag{6.6}$$

$$b_1 = \begin{cases} b_{o1}, V_{S30} \leq V_1 \\ b_{o1} + \dfrac{b_{o2} - b_{o1}}{\ln\left(\frac{V_2}{V_1}\right)} \cdot \ln\left(\dfrac{V_{S30}}{V_1}\right), V_1 < V_{S30} \leq V_2 \\ b_{o2}, V_{S30} > V_2 \end{cases} \tag{6.7}$$

All other parameters are estimated in the maximum likelihood regression. The regression process is executed in two steps. In the first step, the coefficients of the linear-elastic component of the model (i.e., a_1, Z^*, and b) are estimated. These coefficients are kept fixed in the second step, which estimates the parameters in the nonlinear component of the model (b_{o1}, b_{o2}, V_1, V_2, and c). The derived values of all coefficients for the four long periods studied here are listed in Table 6.3. Note that positive values of b_1 (i.e., b_{o1} and b_{o2}) are derived for periods of 5.0 and 10.0 sec, indicating that amplification increases with increases $S_{a,rock}$ at these periods. At T = 1.0 and 2.0 sec, b_1 becomes slightly positive at large V_{S30} values (i.e., b_{o2} become positive). The standard deviation for each model (σ_{lnAF}) is also listed in Table 6.3 and ranges from 0.32 to 0.14.

Figure 6.8 shows the residuals [i.e., ln(data)-ln(predicted)] plotted versus V_{S30}, $S_{a,rock}$, and $Z_{1.0}$ for spectral period of 1.0 sec. The residuals do not show any systematic trend with respect to V_{S30}, $S_{a,rock}$, and $Z_{1.0}$. For all the other long periods considered in this study, the residuals do not show any systematic trend with any of the independent variables in the model.

To investigate how the proposed functional form at long periods (T ≥ 1.0 sec) fits the data, predictions of AF are plotted versus $S_{a,rock}$ for three different values of $Z_{1.0}$ in Figures 6.9 to 6.12. The AF data are also shown in these plots. As noted previously, there is a relationship between V_{S30} of a site and its depth to bedrock (i.e., $Z_{1.0}$) with stiffer sites reaching bedrock at shallower depth. Based on the data shown in Chapter 3 for V_{S30} < 300 m/sec, $Z_{1.0}$ ranges from about 100 to 600 m. Therefore, the predicted AF values are plotted for $Z_{1.0}$ of 100, 300, and 600 m for V_{S30} < 300 m/sec. For V_{S30} > 300 m/sec, $Z_{1.0}$ ranges from 20 to 400 m. For V_{S30} > 300 m/sec, AF predictions are shown for $Z_{1.0}$ of 20, 200, and 400 m. As discussed in the previous chapter, the α parameter incorporates the effect of depth in the model and α is equal to 1.0 for sites with $Z_{1.0}$ greater than Z^*. Therefore, amplification for sites with $Z_{1.0} > Z^*$ is not influenced by $Z_{1.0}$.

At a spectral period of 1.0 sec (Figure 6.9), Z^* is equal to 121 m such that most of the curves shown do not show any $Z_{1.0}$ effect. The curve with $Z_{1.0}$ equal to 100 m for $V_{S30} < 300$ m/sec shows a very small effect; the curve for $Z_{1.0}$ equal to 20 m for $V_{S30} > 300$ m/sec shows a larger effect. However, few of the data have $Z_{1.0}$ equal to 20 m. Similar trends are observed at T = 2.0 sec, but with Z* equal to 292 m the $Z_{1.0}$ effect is more apparent. At longer periods (i.e., 5.0 and 10.0 sec), Z* is much larger (490 and 1000 m, respectively), such that a clear increase in amplification as the depth to the bedrock ($Z_{1.0}$) increases is observed for $V_{S30} <$ 3 00 m/sec. For larger V_{S30}, the V_{S30} approaches V_{ref} (i.e., V_{ref} = 500 m/sec for these periods and AF = 1.0 for $V_{S30} > V_{ref}$) such that the $Z_{1.0}$ effect is not significant.

Table 6.3 Regression coefficients of the site amplification model for long periods.

T (sec)	1.0	2.0	5.0	10.0
a_1	-0.62	-0.75	-0.63	-0.44
Z^* (m)	121	292	490	1000
b	0.70	0.71	1.16	0.76
b_{o1}	-1.6	-0.70	0.17	0.36
b_{02}	0.06	0.10	0.02	0.04
V_1 (m/sec)	114	120	193	143
V_1 (m/sec)	387	380	470	390
c	0.2	0.15	0.005	0.005
V_{ref} (m/sec)	850	600	500	500
σ_{lnAF}	0.32	0.27	0.21	0.14

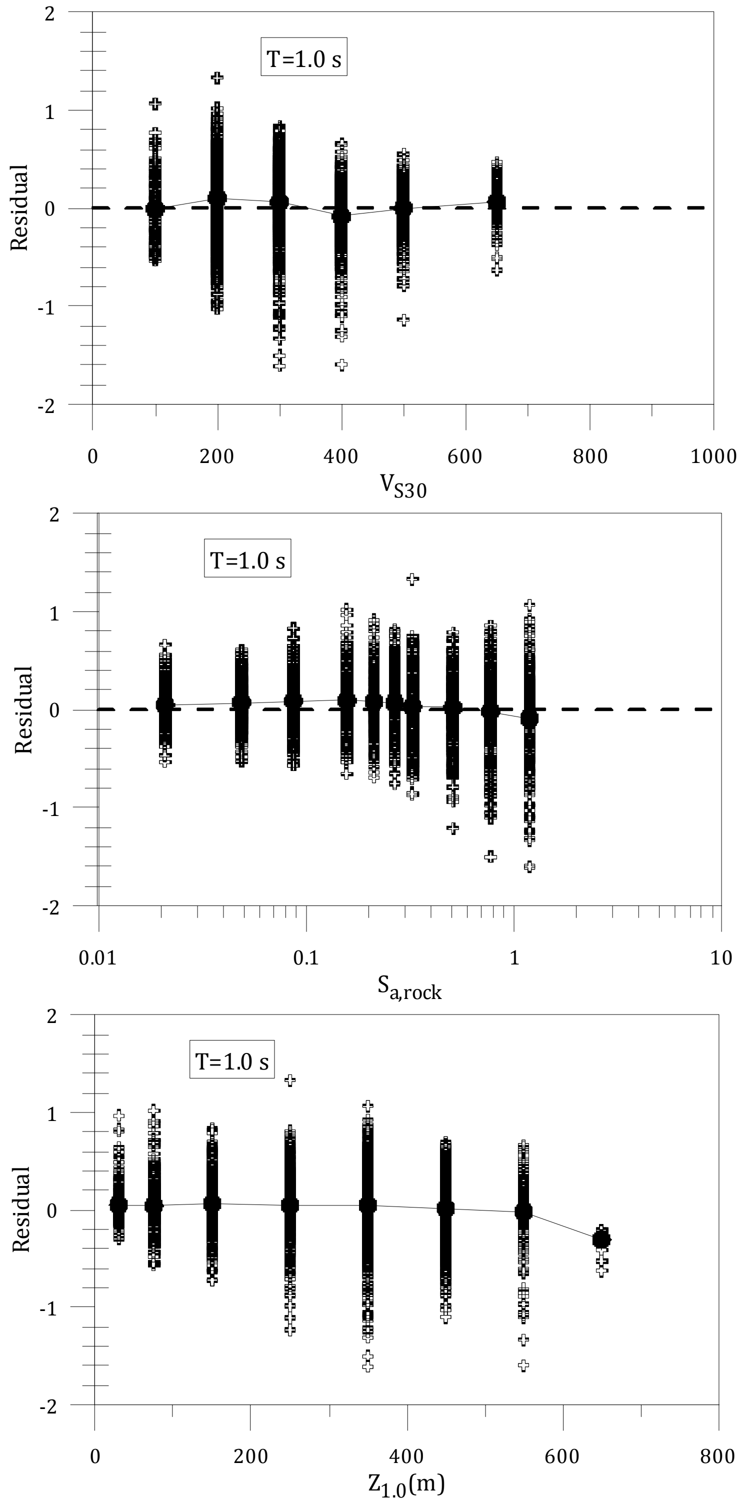

Figure 6.8 **Model residuals for T = 1.0 sec versus V_{S30}, $S_{a,rock}$, and $Z_{1.0}$.**

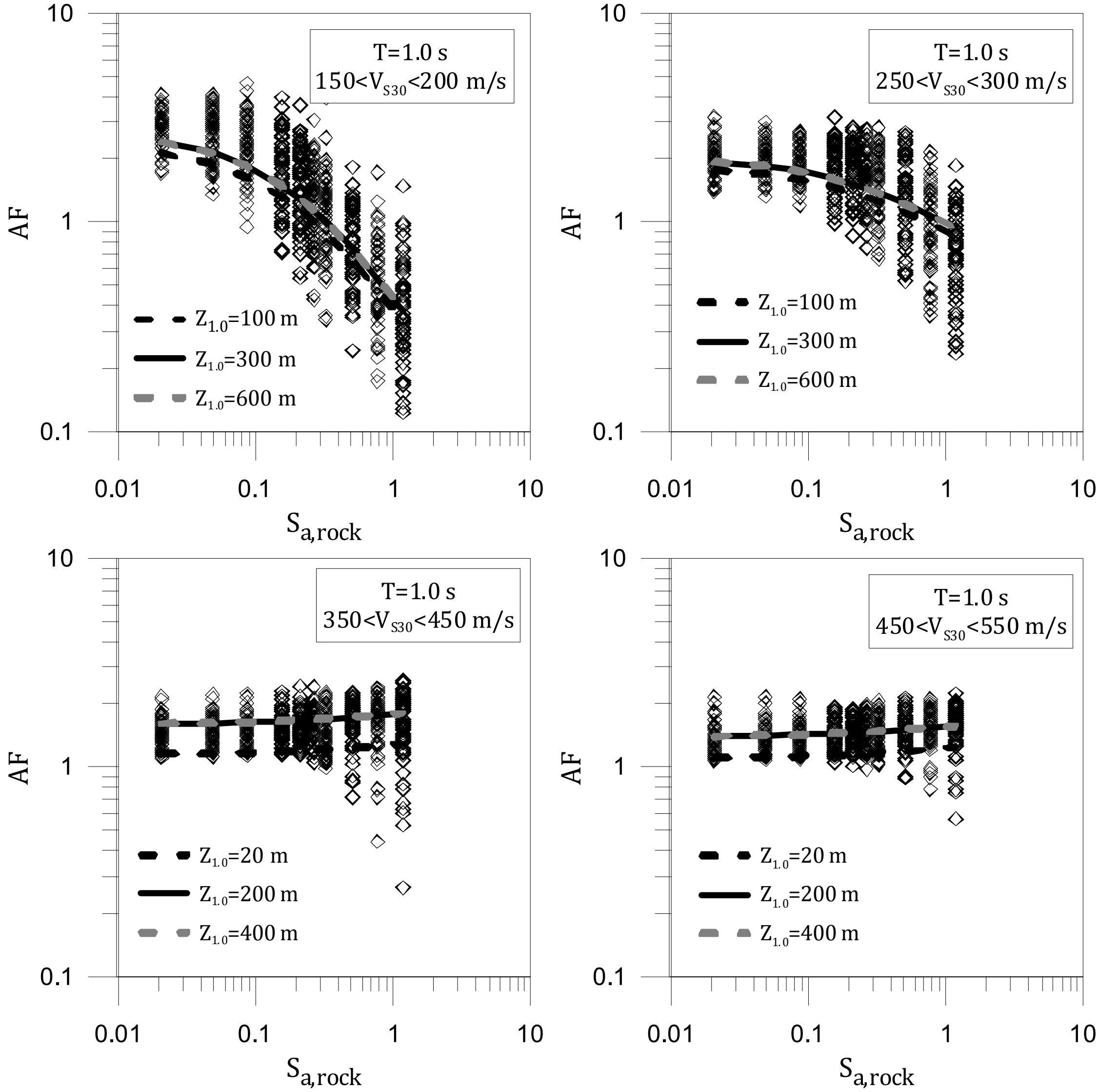

Figure 6.9 Amplification factor for T = 1.0 sec versus $S_{a,rock}$ and model predictions for different values of $Z_{1.0}$.

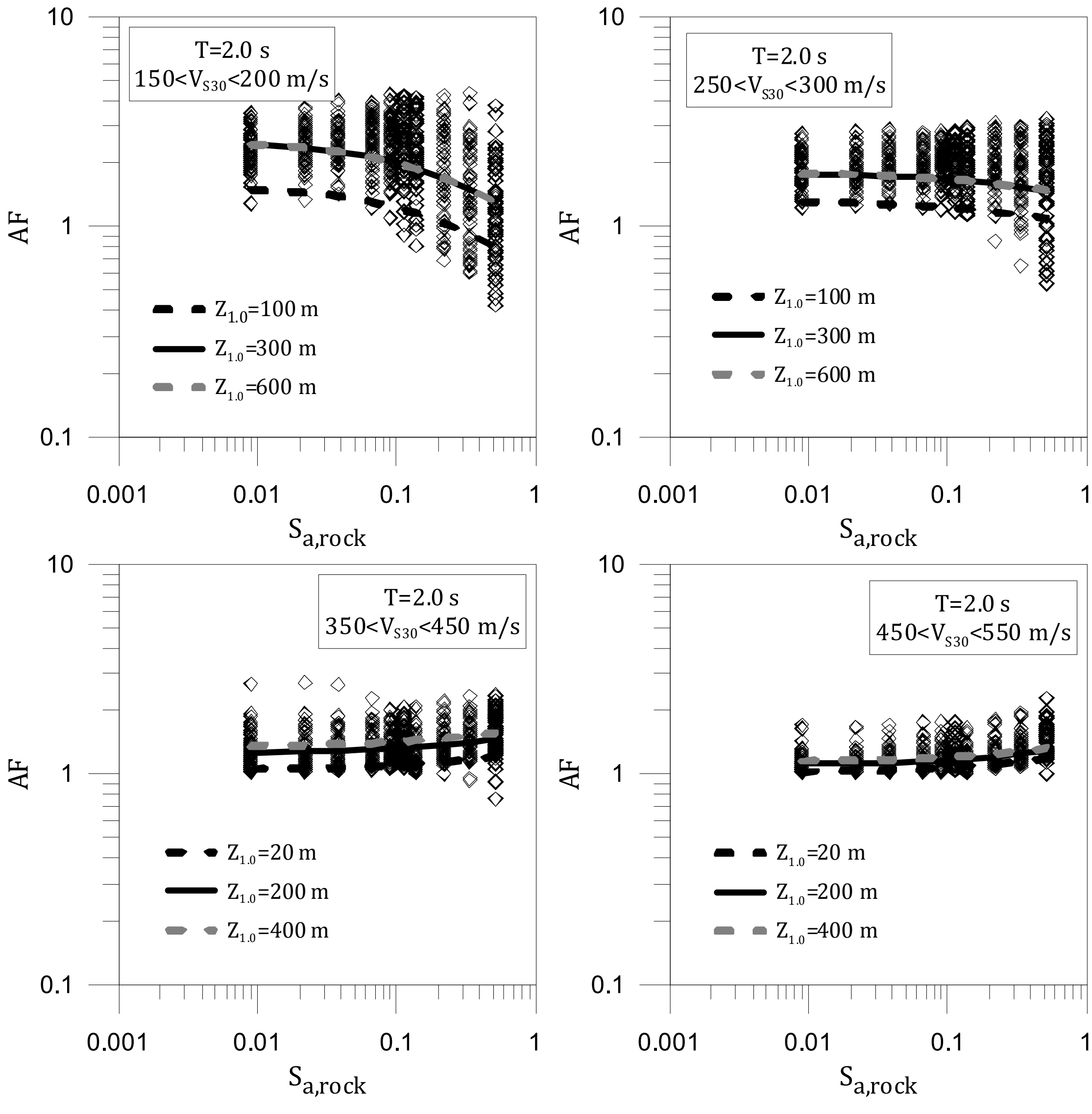

Figure 6.10 Amplification factor for T = 2.0 sec versus $S_{a,rock}$ and model predictions for different values of $Z_{1.0}$.

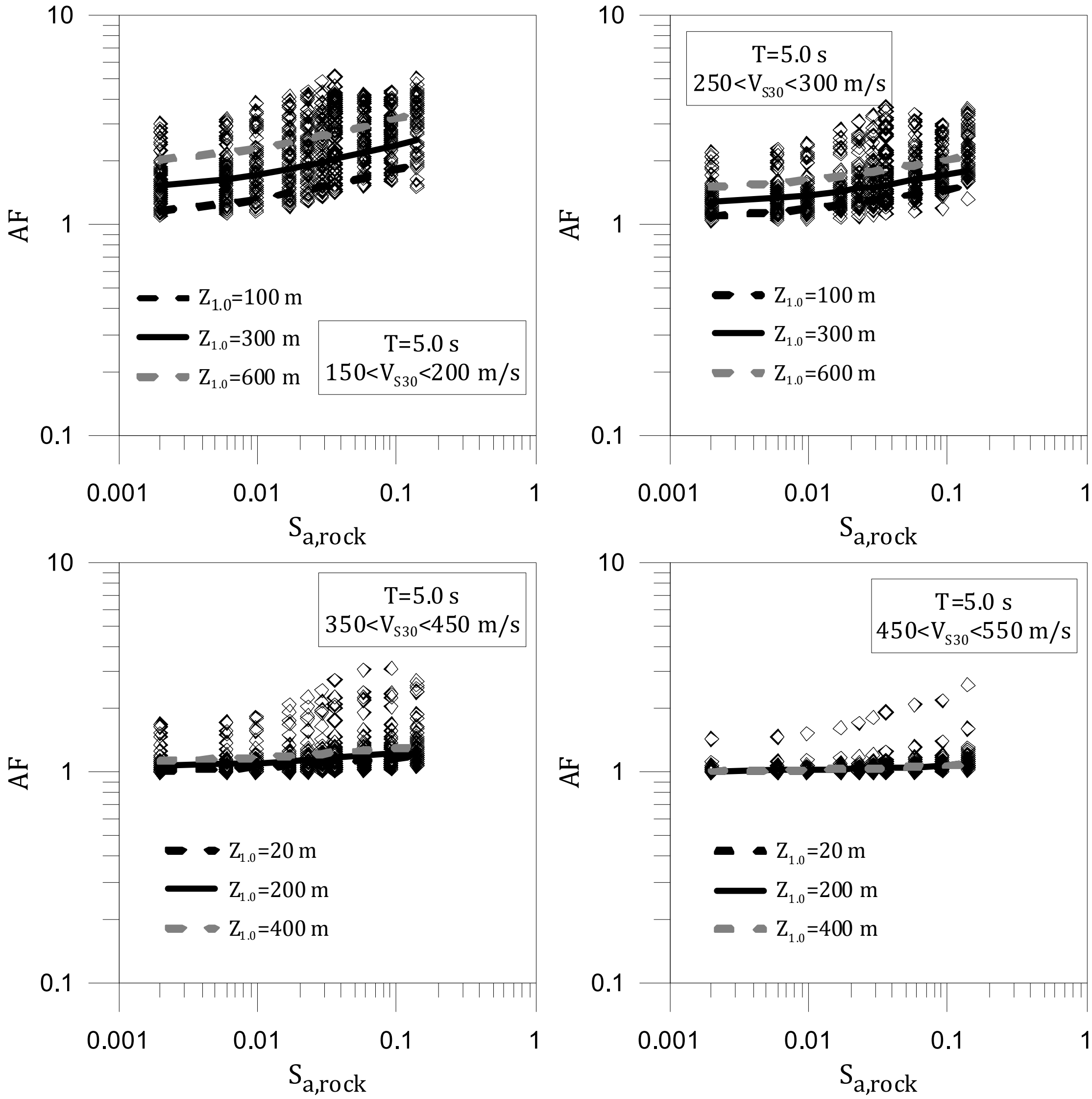

Figure 6.11 **Amplification factor for T = 5.0 sec versus $S_{a,rock}$ and model predictions for different values of $Z_{1.0}$.**

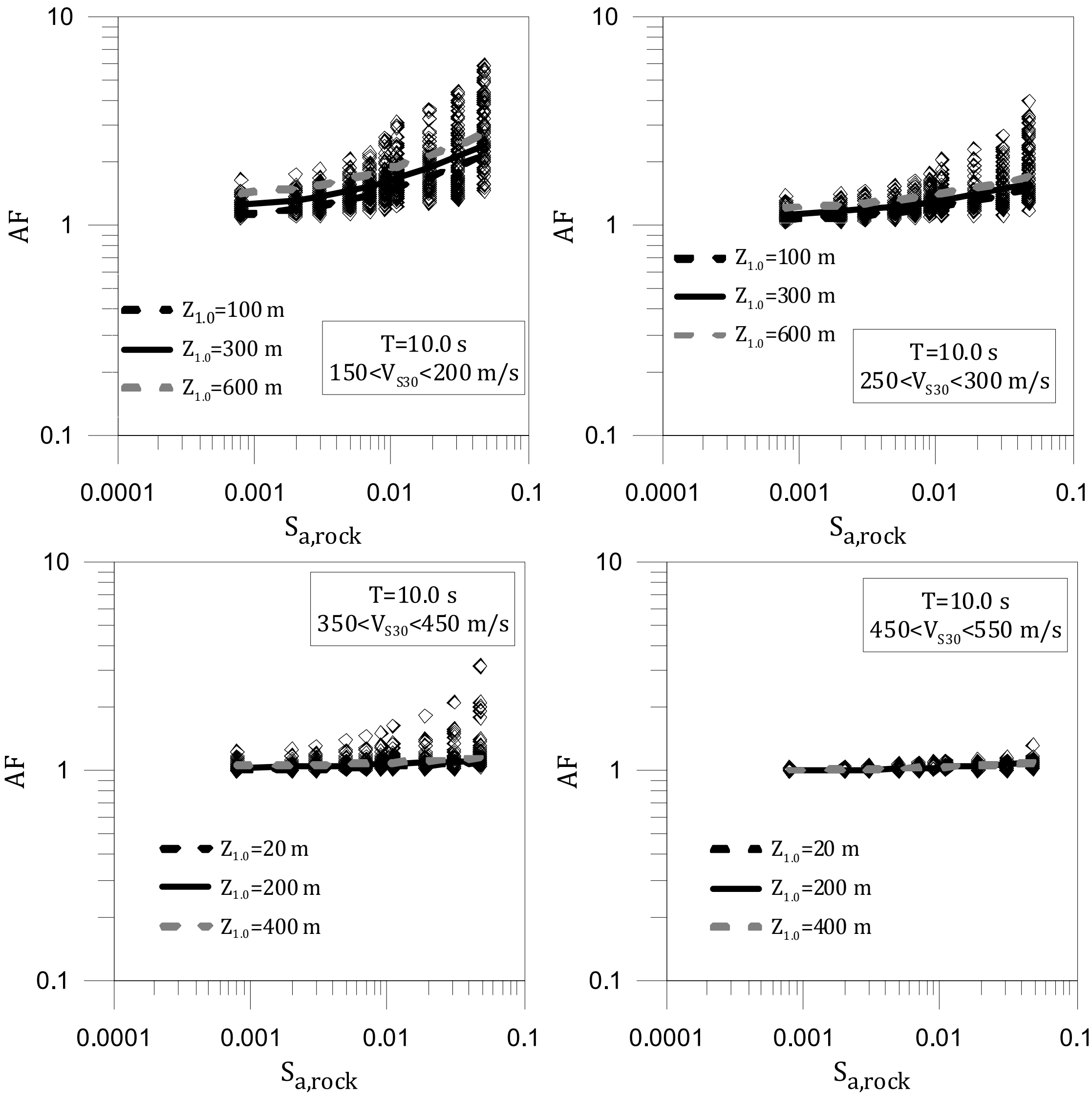

Figure 6.12 Amplification factor versus $S_{a,rock}$ and model predictions for different values of $Z_{1.0}$ for T = 10.0 sec.

6.4 MODEL PREDICTIONS

Two sites with different V_{S30} values (250 m/sec and 350 m/sec) and three input motion intensities were considered to demonstrate the site amplification value predicted by the developed model and the resulting surface response spectra. To show the influence of V_{ratio} on the prediction of amplification, the amplification for each site was predicted for three values of V_{ratio} (i.e., V_{ratio} = 0.85, 1.4, and 2.3), and their amplifications were compared. Both V_{S30} values represent medium stiff soil sites and the $Z_{1.0}$ values assigned to these profiles are consistent with the V_{S30} ($Z_{1.0}$ = 300 m for V_{S30} = 250 m/sec, $Z_{1.0}$ = 100 m for V_{S30} = 350 m/sec).

The response of the soil profiles were predicted for three different levels of shaking; low input intensity (i.e., PGA_{rock} = 0.06*g*), medium input intensity (i.e., PGA_{rock} = 0.13*g*), and high input intensity (i.e., PGA_{rock} = 0.3*g*). These input motions were derived using the average of the predictions from the Next Generation Attenuation (NGA) GMPEs for M_w = 7.0, V_{S30} = 1000 m/sec, and distances of 5, 20, and 50 km, respectively. The resulting input rock response spectra are shown in Figure 6.13.

The AF values predicted by the developed site amplification model for the selected scenarios and for V_{ratio} equal to 0.85, 1.4, and 2.3 are shown in Figure 6.14. The different values of V_{ratio} influence amplification at periods less than 1.0 sec; this difference can be significant at high input intensities. Here, an increase in V_{ratio} from 0.85 to 2.3 can increase the amplification by as much as a factor of 2.0. The resulting soil surface response spectra obtained from applying the AFs from Figure 6.14 to the rock response spectra from Figure 6.13 are shown in Figure 6.15. In all cases, the response of the sites shifts the spectrum to longer periods with the peaks occurring at 0.3 to 0.4 sec rather than at 0.2 sec. The influence of different values of V_{ratio} is readily apparent, with the PGA and maximum spectral acceleration significantly larger for larger V_{ratio}.

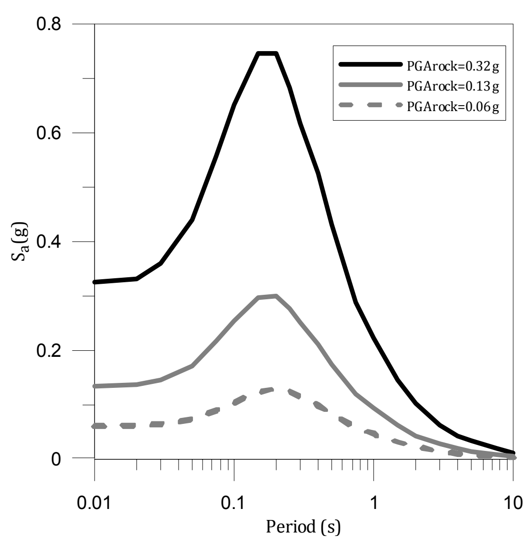

Figure 6.13 Response spectra of the input motions used in model predictions.

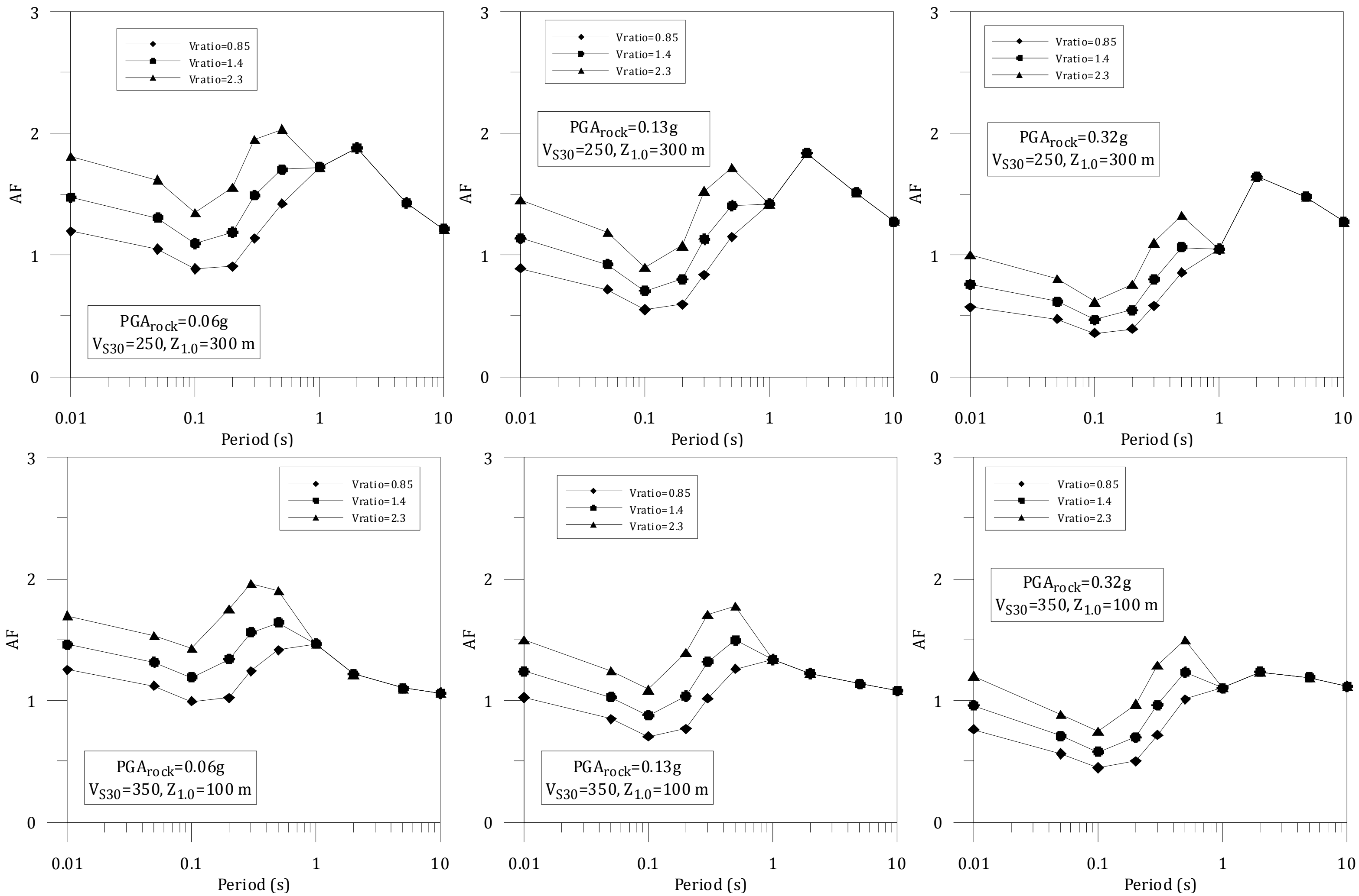

Figure 6.14 Model predictions of amplification factor for different values of V_{ratio} and PGA_{rock}

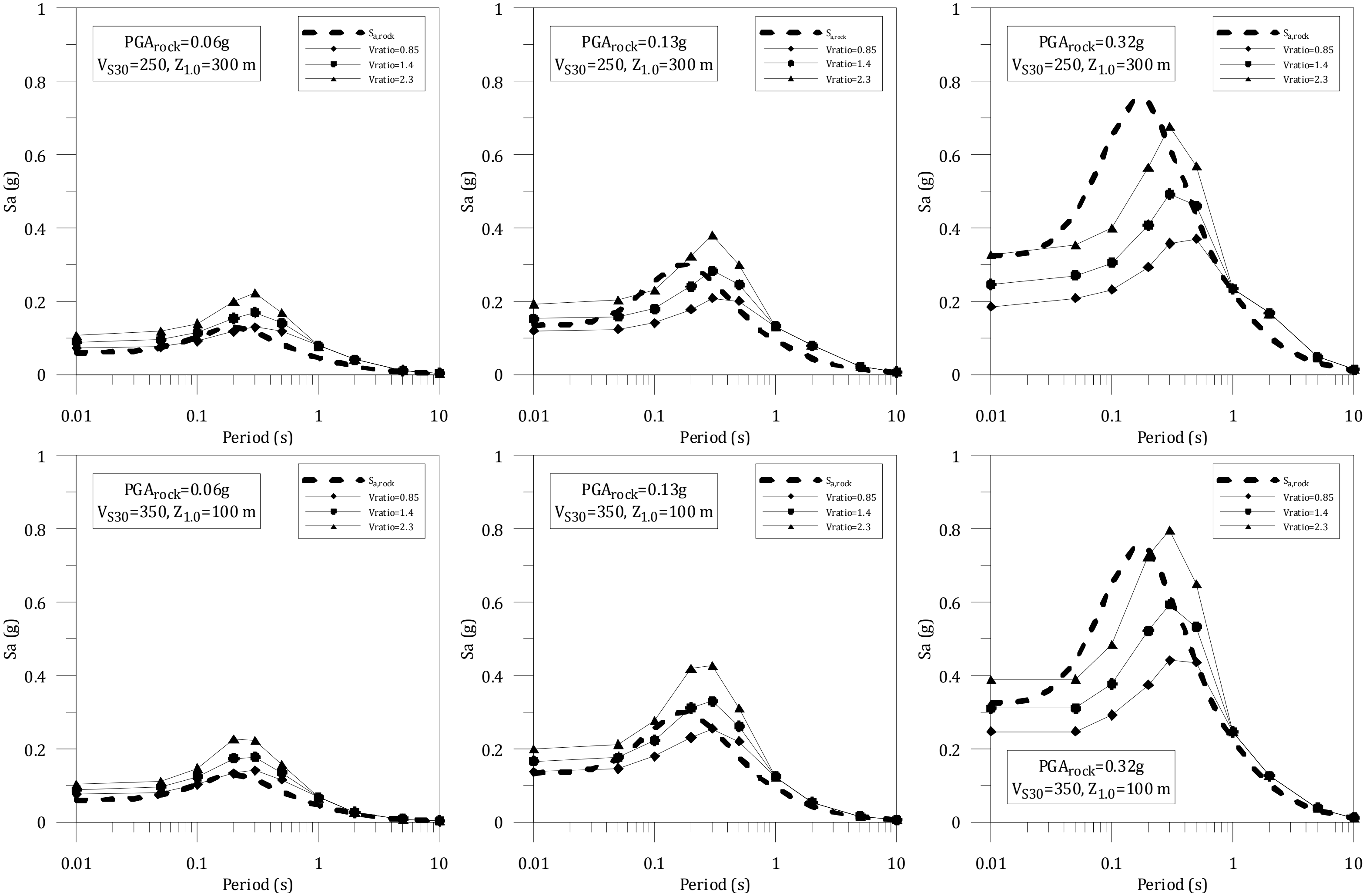

Figure 6.15 Model predictions of surface response spectra for different values of V_{ratio}.

6.5 MODEL LIMITATIONS

The site AFs computed in this study were all based on equivalent linear analysis. The equivalent linear assumption employed in the analysis is often considered invalid at shear strains greater than about 1.0%. At high levels of shaking, softer soil profiles may experience strains significantly larger than 1.0%. This issue introduces some limitations to the model when applying it to softer sites at larger input intensities.

The level of generated shear strain in a soil profile depends on the stiffness of the site and the level of shaking. Softer soil profiles experience larger strains than stiffer soil profiles subjected to the same level of input intensity. Figure 6.16 plots shear strain profiles induced in the softest site considered in this study (V_{S30} = 118 m/sec) for four different input intensities. At PGA_{rock} = 0.1*g*, the maximum generated strain in the site is about 0.4%. The maximum induced strain increases as PGA_{rock} increases and exceeds 1% for PGA_{rock} = 0.22*g* and larger. This result indicates that the AF values from this site are not realistic for PGA_{rock} greater than 0.22*g*.

The PGA_{rock} that first induces maximum shear strains greater than 1% is called $PGA_{rock\text{ -}1\%}$. This value is compiled for the profiles analyzed and used to identify the limitations of the developed model. Figure 6.17 plots $PGA_{rock\text{ -}1\%}$ versus V_{S30} for the soil profiles analyzed in this study. For soil profiles with V_{S30} less than 200 m/sec, the maximum shear strain exceeds 1% at PGA_{rock} = 0.22*g*. The maximum shear strain exceeds 1% at larger input intensities for stiffer sites (e.g., $PGA_{rock\text{ -}1\%}$ ~ 0.4*g* for V_{S30} = 300 m/sec, $PGA_{rock\text{ -}1\%}$ ~ 1.0*g* for V_{S30} = 400 m/sec). For soil profiles with V_{S30} greater than 500 m/sec, the maximum induced shear strain does not exceed 1% for the sites and input motions analyzed in this study. Figure 6.17 shows the ranges of V_{S30} and PGA_{rock} for which the developed model is appropriate. For stiff sites with V_{S30}> 500 m/sec, the developed model can be used at all levels of shaking.

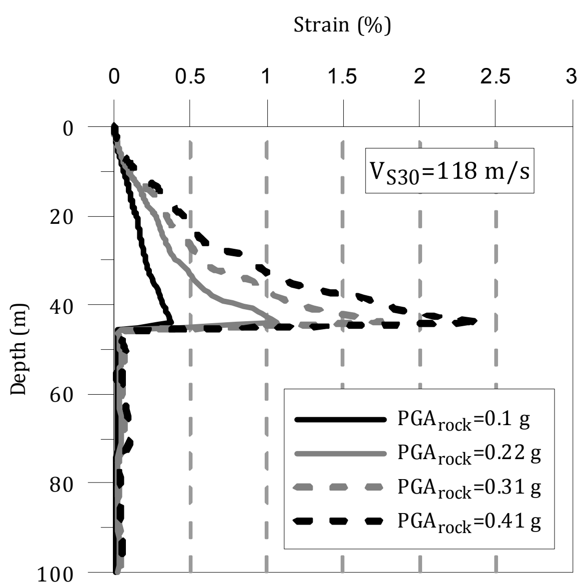

Figure 6.16 Induced shear strain profile in a soft site (V_{S30} = 118 m/sec) for different levels of shaking.

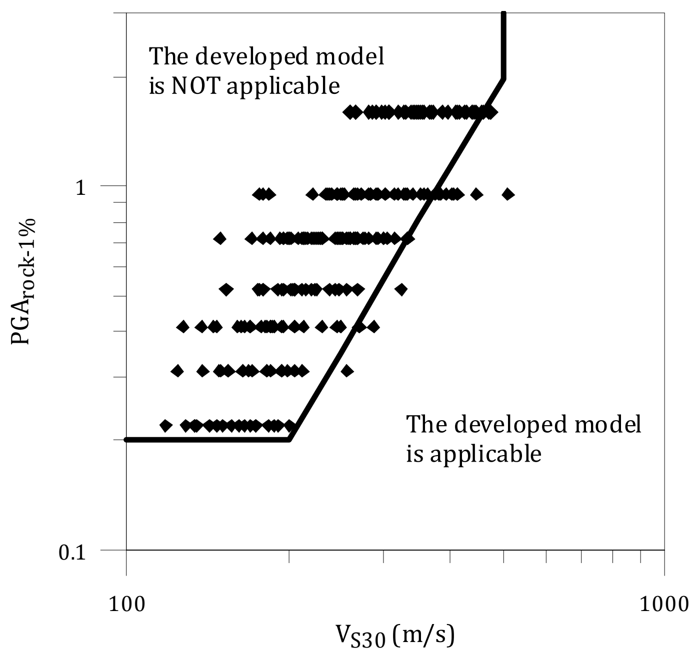

Figure 6.17 Relationship between PGA$_{rock-1\%}$ and V$_{S30}$ for the analyses performed.

7 Summary and Conclusions

The study presented herein developed an improved site amplification model that considers the effect of multiple site parameters that affect site amplification. This model includes parameters previously considered in GMPEs (e.g., V_{S30} and $Z_{1.0}$), but also identifies an additional parameter that influences site amplification (V_{ratio}).

To identify the appropriate site parameters to be included in the site amplification model, 99 soil profiles were generated manually using five baseline velocity profiles. The top 30 m of each baseline shear wave velocity profile was modified to maintain the same V_{S30} but to simulate a different V_S structure. The seismic responses of the generated profiles were analyzed using the equivalent linear approach as implemented in the site response program *Strata* [Kottke and Rathje 2008]. Different site parameters such as V_{min}, thV_{min}, MAXIR, and V_{ratio} were considered to explain the variability in AF across sites with a common V_{S30}. These analyses identified V_{ratio} as the site parameter that influences site amplification most significantly, helping to explain the variability in amplification across sites with the same V_{S30}.

To generalize the findings from the analyses in which only the top 30 m of the velocity profile were varied, a suite of fully randomized velocity profiles were generated and their responses analyzed using *Strata* for a range of input motion intensities. The results of the site response analyses conducted on these 400 fully randomized velocity profiles confirmed the influence of V_{ratio} on site amplification. The computed AFs were used to develop a functional form that incorporates its influence on both the linear-elastic and nonlinear components of the site amplification model. The computed site AFs under low input intensity (PGA_{rock} = 0.01*g*) were used to develop the linear-elastic component of the model, and the AFs from higher input intensities were used to develop the nonlinear component.

The effect of V_{ratio} on site amplification is significant only at shorter periods (T < 1.0 sec). Therefore, different models were developed for shorter (T < 1.0 sec) and longer (T ≥ 1.0 sec) periods. At short periods, the linear-elastic component of the model uses a second-order polynomial functional form for modeling the effect of ln(V_{S30}) on ln(AF) rather than the linear relationship used in other site amplification models. The second-order polynomial better fits the AF data at low intensities, particularly at smaller values of V_{S30}. The linear-elastic model incorporates the effects of V_{ratio} through a linear relationship between ln(V_{ratio}) and ln(AF). The slope of this relationship is V_{S30} dependent. At longer periods, the model uses a linear relationship between ln(V_{S30}) and ln(AF) rather than a second-order polynomial, and no V_{ratio}

effect is modeled. Additionally, at long periods site amplification is affected by the depth to bedrock (i.e., $Z_{1.0}$) in addition to V_{S30}. The effect of $Z_{1.0}$ is considered in the linear component of the proposed model because it is not influenced by soil nonlinearity.

The nonlinear component of the model incorporates the effect of input intensity on the V_{S30} and V_{ratio} scaling. The effect of input intensity is coupled with the V_{S30} scaling by making ln(AF) a function of $S_{a,rock}$ and V_{S30}. The effect of input intensity on the V_{ratio} scaling is incorporated by making the relationship between ln(AF) and ln(V_{ratio}) a function of $S_{a,rock}$.

The resulting amplification model accounts for the influence of V_{S30}, V_{ratio}, $S_{a,rock}$, and $Z_{1.0}$. Generally, larger amplification is predicted for sites with smaller V_{S30}, larger V_{ratio}, and larger $Z_{1.0}$. For sites with the same average shear wave velocity in top 30 m (V_{S30}), a larger value of V_{ratio} indicates a larger change in V_S over the top 30 m; these sites will experience larger site amplification.

A limitation of the developed model is that it is based on AFs computed from equivalent-linear site response analysis. Soft soil profiles under high levels of shaking may experience strains significantly large enough (i.e., greater than about 1%) to make the equivalent-linear assumption invalid. The shaking level above which the maximum generated shear strain in a profile exceeds 1% is V_{S30} dependent. The PGA_{rock} at which shear strains exceeded 1% in the analyses was identified and used to define the limitations on PGA_{rock} for the developed model as a function of V_{S30}.

REFERENCES

Abrahamson N., Silva W.J. (2008). Summary of the Abrahamson and Silva ground motion relations, *Earthq. Spectra*, 24(1): 67–97.

Boore D.M. (2003). Simulation of ground motion using the stochastic method, *Pure and Applied. Geophys*., 160(3–4): 635–676.

Boore D.M., Joyner W.B., Fumal T.E. (1993). Estimation of response spectra and peak accelerations from western North American earthquakes: An interim report, U.S. Geological Survey, *USGS Open-File Report 93–509*, 72 pgs.

Boore D.M. et al (1997). Equations for estimating horizontal response spectra and peak acceleration from western North American earthquakes: A summary of recent work (with 2005 erratum), *Seism. Res. Lett.,* 68: 128–153.

Brune J.N. (1970) Tectonic stress and the spectra of seismic shear waves from earthquakes, *J. Geophys. Res*., 75(26): 4997−5009.

Campbell K.W. (1993). Empirical prediction of near-source ground motion from large earthquakes, *Proceedings, Inter. Workshop on Earthquake Hazards and Large Dams in the Himalaya*, New Delhi, India.

Campbell K.W. (2003). Prediction of strong ground motion using the hybrid empirical method and its use in the development of ground-motion (attenuation) relationships in Eastern North America, *Bull. Seismol. Soc. Am*., 93(3): 1012–1033.

Campbell K.W., Bozorgnia Y. (2008). NGA Ground motion model for the geometric mean horizontal component of PGA, PGV, PGD, and 5% damped linear elastic response spectra for periods ranging from 0.01 to 10 s, *Earthq. Spectra*, 24(1): 139–171.

Chiou B.S.J., Youngs R.R. (2008). An NGA model for the average horizontal component of peak ground motion and response spectra, *Earthq. Spectra*, 24(1): 173–215.

Choi Y., Stewart J.P. (2005). Nonlinear site amplification as function of 30 m shear wave velocity, *Earthq. Spectra*, 21(1): 1–30.

Costantino C.J., Heymsfield E., Gu Y.-T. (1991). Site specific estimates of surface ground motions for the K-reactor site, Savannah River Plant, Technical Report, Brookhaven National Laboratory, Nuclear Energy Department, Structural Analysis Division, Upton, NY.

Darendeli M.B. (2001). *Development of a New Family of Normalized Modulus Reduction and Material Damping Curves*, Ph.D. Dissertation, Dept. of Civil and Enviro. Eng., University of Texas, Austin, TX.

Kottke A.R., Rathje E.M. (2008). Technical manual for Strata. *Report PEER 2008/10*, Pacific Earthquake Engineering Research Center, University of California, Berkeley, CA.

Kottke A.R. (2011). Site amplification model considering VS30 and depth, unpublished report.

McGuire R.K., Toro G.R., O'Hara T.P., Jacobson J.P., Silva W.J. (1989). Probabilistic seismic hazard evaluation at nuclear plant sites in the Central and Eastern United States: Resolution of the Charleston Earthquake Issue. Electric Power Research Institute, Palo Alto, CA.

Navidi S. (2012) *Development of Site Amplification Model for Use in Ground Motion Prediction Equations*. Ph.D. Dissertation, Dept. of Civil, Arch. and Envir. Eng., University of Texas, Austin, TX.

Sadigh K., Chang C.-Y., Egan J.A., Makdisi F., Youngs R.R. (1997). Attenuation relationships for shallow crustal earthquakes based on California strong motion data, *Seismol. Res. Lett*., 68(1): 180–189.

Toro G.R. (1995) Probabilistic models of site velocity profiles for generic and site-specific ground-motion amplification studies, *Technical Report 779574,* Brookhaven National Laboratory, Upton, NY.

Toro G.R., Silva W.J., McGuire R., Hermann R. (1992). Probabilistic seismic hazard mapping of the Mississippi Embayment, *Seismol. Res. Lett*., 63(3): 449–475.

Walling M, Silva W.J., Abrahamson N.A. (2008). Nonlinear site amplification factors for constraining the NGA models, *Earthq. Spectra,* 24(1): 243–255.

PEER REPORTS

PEER reports are available as a free PDF download from http://peer.berkeley.edu/publications/peer_reports_complete.html. Printed hard copies of PEER reports can be ordered directly from our printer by following the instructions at http://peer.berkeley.edu/publications/peer_reports.html. For other related questions about the PEER Report Series, contact the Pacific Earthquake Engineering Research Center, 325 Davis Hall mail code 1792, Berkeley, CA 94720. Tel.: (510) 642-3437; Fax: (510) 665-1655; Email: peer_editor@berkeley.edu

PEER 2013/18 *Identification of Site Parameters that Improve Predictions of Site Amplification.* Ellen M. Rathje and Sara Navidi. July 2013.

PEER 2013/17 *Response Spectrum Analysis of Concrete Gravity Dams Including Dam-Water-Foundation Interaction.* Arnkjell Løkke and Anil K. Chopra. July 2013.

PEER 2013/16 *Effect of hoop reinforcement spacing on the cyclic response of large reinforced concrete special moment frame beams.* Marios Panagiotou, Tea Visnjic, Grigorios Antonellis, Panagiotis Galanis, and Jack P. Moehle. June 2013.

PEER 2013/15 *publication pending*

PEER 2013/14 *publication pending*

PEER 2013/13 *publication pending*

PEER 2013/12 *Nonlinear Horizontal Site Response for the NGA-West2 Project.* Ronnie Kamai, Norman A. Abramson, Walter J. Silva. May 2013.

PEER 2013/11 *Epistemic Uncertainty for NGA-West2 Models.* Linda Al Atik and Robert R. Youngs. May 2013.

PEER 2013/10 *NGA-West 2 Models for Ground-Motion Directionality.* Shrey K. Shahi and Jack W. Baker. May 2013.

PEER 2013/09 *Final Report of the NGA-West2 Directivity Working Group.* Paul Spudich, Jeffrey R. Bayless, Jack W. Baker, Brian S.J. Chiou, Badie Rowshandel, Shrey Shahi, and Paul Somerville. May 2013.

PEER 2013/08 *NGA-West2 Model for Estimating Average Horizontal Values of Pseudo-Absolute Spectral Accelerations Generated by Crustal Earthquakes.* I. M. Idriss. May 2013.

PEER 2013/07 *Update of the Chiou and Youngs NGA Ground Motion Model for Average Horizontal Component of Peak Ground Motion and Response Spectra.* Brian Chiou and Robert Youngs. May 2013.

PEER 2013/06 *NGA-West2 Campbell-Bozorgnia Ground Motion Model for the Horizontal Components of PGA, PGV, and 5%-Damped Elastic Pseudo-Acceleration Response Spectra for Periods Ranging from 0.01 to 10 sec.* Kenneth W. Campbell and Yousef Bozorgnia. May 2013.

PEER 2013/05 *NGA-West 2 Equations for Predicting Response Spectral Accelerations for Shallow Crustal Earthquakes.* David M. Boore, Jonathan P. Stewart, Emel Seyhan, Gail M. Atkinson. May 2013.

PEER 2013/04 *Update of the AS08 Ground-Motion Prediction Equations Based on the NGA-West2 Data Set.* Norman Abrahamson, Walter Silva, and Ronnie Kamai. May 2013.

PEER 2013/03 *PEER NGA-West2 Database.* Timothy D. Ancheta, Robert B. Darragh, Jonathan P. Stewart, Emel Seyhan, Walter J. Silva, Brian S.J. Chiou, Katie E. Wooddell, Robert W. Graves, Albert R. Kottke, David M. Boore, Tadahiro Kishida, and Jennifer L. Donahue. May 2013.

PEER 2013/02 *Hybrid Simulation of the Seismic Response of Squat Reinforced Concrete Shear Walls.* Catherine A. Whyte and Bozidar Stojadinovic. May 2013.

PEER 2013/01 *Housing Recovery in Chile: A Qualitative Mid-program Review.* Mary C. Comerio. February 2013.

PEER 2012/08 *Guidelines for Estimation of Shear Wave Velocity.* Bernard R. Wair, Jason T. DeJong, and Thomas Shantz. December 2012.

PEER 2012/07 *Earthquake Engineering for Resilient Communities: 2012 PEER Internship Program Research Report Collection.* Heidi Tremayne (Editor), Stephen A. Mahin (Editor), Collin Anderson, Dustin Cook, Michael Erceg, Carlos Esparza, Jose Jimenez, Dorian Krausz, Andrew Lo, Stephanie Lopez, Nicole McCurdy, Paul Shipman, Alexander Strum, Eduardo Vega. December 2012.

PEER 2012/06 *Fragilities for Precarious Rocks at Yucca Mountain.* Matthew D. Purvance, Rasool Anooshehpoor, and James N. Brune. December 2012.

PEER 2012/05 *Development of Simplified Analysis Procedure for Piles in Laterally Spreading Layered Soils.* Christopher R. McGann, Pedro Arduino, and Peter Mackenzie–Helnwein. December 2012.

PEER 2012/04 *Unbonded Pre-Tensioned Columns for Bridges in Seismic Regions.* Phillip M. Davis, Todd M. Janes, Marc O. Eberhard, and John F. Stanton. December 2012.

PEER 2012/03 *Experimental and Analytical Studies on Reinforced Concrete Buildings with Seismically Vulnerable Beam-Column Joints.* Sangjoon Park and Khalid M. Mosalam. October 2012.

PEER 2012/02 *Seismic Performance of Reinforced Concrete Bridges Allowed to Uplift during Multi-Directional Excitation.* Andres Oscar Espinoza and Stephen A. Mahin. July 2012.

PEER 2012/01 *Spectral Damping Scaling Factors for Shallow Crustal Earthquakes in Active Tectonic Regions.* Sanaz Rezaeian, Yousef Bozorgnia, I. M. Idriss, Kenneth Campbell, Norman Abrahamson, and Walter Silva. July 2012.

PEER 2011/10 *Earthquake Engineering for Resilient Communities: 2011 PEER Internship Program Research Report Collection.* Eds. Heidi Faison and Stephen A. Mahin. December 2011.

PEER 2011/09 *Calibration of Semi-Stochastic Procedure for Simulating High-Frequency Ground Motions.* Jonathan P. Stewart, Emel Seyhan, and Robert W. Graves. December 2011.

PEER 2011/08 *Water Supply in regard to Fire Following Earthquake.* Charles Scawthorn. November 2011.

PEER 2011/07 *Seismic Risk Management in Urban Areas. Proceedings of a U.S.-Iran-Turkey Seismic Workshop.* September 2011.

PEER 2011/06 *The Use of Base Isolation Systems to Achieve Complex Seismic Performance Objectives.* Troy A. Morgan and Stephen A. Mahin. July 2011.

PEER 2011/05 *Case Studies of the Seismic Performance of Tall Buildings Designed by Alternative Means.* Task 12 Report for the Tall Buildings Initiative. Jack Moehle, Yousef Bozorgnia, Nirmal Jayaram, Pierson Jones, Mohsen Rahnama, Nilesh Shome, Zeynep Tuna, John Wallace, Tony Yang, and Farzin Zareian. July 2011.

PEER 2011/04 *Recommended Design Practice for Pile Foundations in Laterally Spreading Ground.* Scott A. Ashford, Ross W. Boulanger, and Scott J. Brandenberg. June 2011.

PEER 2011/03 *New Ground Motion Selection Procedures and Selected Motions for the PEER Transportation Research Program.* Jack W. Baker, Ting Lin, Shrey K. Shahi, and Nirmal Jayaram. March 2011.

PEER 2011/02 *A Bayesian Network Methodology for Infrastructure Seismic Risk Assessment and Decision Support.* Michelle T. Bensi, Armen Der Kiureghian, and Daniel Straub. March 2011.

PEER 2011/01 *Demand Fragility Surfaces for Bridges in Liquefied and Laterally Spreading Ground.* Scott J. Brandenberg, Jian Zhang, Pirooz Kashighandi, Yili Huo, and Minxing Zhao. March 2011.

PEER 2010/05 *Guidelines for Performance-Based Seismic Design of Tall Buildings.* Developed by the Tall Buildings Initiative. November 2010.

PEER 2010/04 *Application Guide for the Design of Flexible and Rigid Bus Connections between Substation Equipment Subjected to Earthquakes.* Jean-Bernard Dastous and Armen Der Kiureghian. September 2010.

PEER 2010/03 *Shear Wave Velocity as a Statistical Function of Standard Penetration Test Resistance and Vertical Effective Stress at Caltrans Bridge Sites.* Scott J. Brandenberg, Naresh Bellana, and Thomas Shantz. June 2010.

PEER 2010/02 *Stochastic Modeling and Simulation of Ground Motions for Performance-Based Earthquake Engineering.* Sanaz Rezaeian and Armen Der Kiureghian. June 2010.

PEER 2010/01 *Structural Response and Cost Characterization of Bridge Construction Using Seismic Performance Enhancement Strategies.* Ady Aviram, Božidar Stojadinović, Gustavo J. Parra-Montesinos, and Kevin R. Mackie. March 2010.

PEER 2009/03 *The Integration of Experimental and Simulation Data in the Study of Reinforced Concrete Bridge Systems Including Soil-Foundation-Structure Interaction.* Matthew Dryden and Gregory L. Fenves. November 2009.

PEER 2009/02 *Improving Earthquake Mitigation through Innovations and Applications in Seismic Science, Engineering, Communication, and Response. Proceedings of a U.S.-Iran Seismic Workshop.* October 2009.

PEER 2009/01 *Evaluation of Ground Motion Selection and Modification Methods: Predicting Median Interstory Drift Response of Buildings.* Curt B. Haselton, Ed. June 2009.

PEER 2008/10 *Technical Manual for Strata.* Albert R. Kottke and Ellen M. Rathje. February 2009.

PEER 2008/09 *NGA Model for Average Horizontal Component of Peak Ground Motion and Response Spectra.* Brian S.-J. Chiou and Robert R. Youngs. November 2008.

PEER 2008/08 *Toward Earthquake-Resistant Design of Concentrically Braced Steel Structures.* Patxi Uriz and Stephen A. Mahin. November 2008.

PEER 2008/07 *Using OpenSees for Performance-Based Evaluation of Bridges on Liquefiable Soils.* Stephen L. Kramer, Pedro Arduino, and HyungSuk Shin. November 2008.

PEER 2008/06 *Shaking Table Tests and Numerical Investigation of Self-Centering Reinforced Concrete Bridge Columns.* Hyung IL Jeong, Junichi Sakai, and Stephen A. Mahin. September 2008.

PEER 2008/05 *Performance-Based Earthquake Engineering Design Evaluation Procedure for Bridge Foundations Undergoing Liquefaction-Induced Lateral Ground Displacement.* Christian A. Ledezma and Jonathan D. Bray. August 2008.

PEER 2008/04 *Benchmarking of Nonlinear Geotechnical Ground Response Analysis Procedures.* Jonathan P. Stewart, Annie On-Lei Kwok, Yousseff M. A. Hashash, Neven Matasovic, Robert Pyke, Zhiliang Wang, and Zhaohui Yang. August 2008.

PEER 2008/03 *Guidelines for Nonlinear Analysis of Bridge Structures in California.* Ady Aviram, Kevin R. Mackie, and Božidar Stojadinović. August 2008.

PEER 2008/02 *Treatment of Uncertainties in Seismic-Risk Analysis of Transportation Systems.* Evangelos Stergiou and Anne S. Kiremidjian. July 2008.

PEER 2008/01 *Seismic Performance Objectives for Tall Buildings.* William T. Holmes, Charles Kircher, William Petak, and Nabih Youssef. August 2008.

PEER 2007/12 *An Assessment to Benchmark the Seismic Performance of a Code-Conforming Reinforced Concrete Moment-Frame Building.* Curt Haselton, Christine A. Goulet, Judith Mitrani-Reiser, James L. Beck, Gregory G. Deierlein, Keith A. Porter, Jonathan P. Stewart, and Ertugrul Taciroglu. August 2008.

PEER 2007/11 *Bar Buckling in Reinforced Concrete Bridge Columns.* Wayne A. Brown, Dawn E. Lehman, and John F. Stanton. February 2008.

PEER 2007/10 *Computational Modeling of Progressive Collapse in Reinforced Concrete Frame Structures.* Mohamed M. Talaat and Khalid M. Mosalam. May 2008.

PEER 2007/09 *Integrated Probabilistic Performance-Based Evaluation of Benchmark Reinforced Concrete Bridges.* Kevin R. Mackie, John-Michael Wong, and Božidar Stojadinović. January 2008.

PEER 2007/08 *Assessing Seismic Collapse Safety of Modern Reinforced Concrete Moment-Frame Buildings.* Curt B. Haselton and Gregory G. Deierlein. February 2008.

PEER 2007/07 *Performance Modeling Strategies for Modern Reinforced Concrete Bridge Columns.* Michael P. Berry and Marc O. Eberhard. April 2008.

PEER 2007/06 *Development of Improved Procedures for Seismic Design of Buried and Partially Buried Structures.* Linda Al Atik and Nicholas Sitar. June 2007.

PEER 2007/05 *Uncertainty and Correlation in Seismic Risk Assessment of Transportation Systems.* Renee G. Lee and Anne S. Kiremidjian. July 2007.

PEER 2007/04 *Numerical Models for Analysis and Performance-Based Design of Shallow Foundations Subjected to Seismic Loading.* Sivapalan Gajan, Tara C. Hutchinson, Bruce L. Kutter, Prishati Raychowdhury, José A. Ugalde, and Jonathan P. Stewart. May 2008.

PEER 2007/03 *Beam-Column Element Model Calibrated for Predicting Flexural Response Leading to Global Collapse of RC Frame Buildings.* Curt B. Haselton, Abbie B. Liel, Sarah Taylor Lange, and Gregory G. Deierlein. May 2008.

PEER 2007/02 *Campbell-Bozorgnia NGA Ground Motion Relations for the Geometric Mean Horizontal Component of Peak and Spectral Ground Motion Parameters.* Kenneth W. Campbell and Yousef Bozorgnia. May 2007.

PEER 2007/01 *Boore-Atkinson NGA Ground Motion Relations for the Geometric Mean Horizontal Component of Peak and Spectral Ground Motion Parameters.* David M. Boore and Gail M. Atkinson. May. May 2007.

PEER 2006/12 *Societal Implications of Performance-Based Earthquake Engineering.* Peter J. May. May 2007.

PEER 2006/11 *Probabilistic Seismic Demand Analysis Using Advanced Ground Motion Intensity Measures, Attenuation Relationships, and Near-Fault Effects.* Polsak Tothong and C. Allin Cornell. March 2007.

PEER 2006/10 *Application of the PEER PBEE Methodology to the I-880 Viaduct.* Sashi Kunnath. February 2007.

PEER 2006/09 *Quantifying Economic Losses from Travel Forgone Following a Large Metropolitan Earthquake.* James Moore, Sungbin Cho, Yue Yue Fan, and Stuart Werner. November 2006.

PEER 2006/08 *Vector-Valued Ground Motion Intensity Measures for Probabilistic Seismic Demand Analysis.* Jack W. Baker and C. Allin Cornell. October 2006.

PEER 2006/07 *Analytical Modeling of Reinforced Concrete Walls for Predicting Flexural and Coupled–Shear-Flexural Responses.* Kutay Orakcal, Leonardo M. Massone, and John W. Wallace. October 2006.

PEER 2006/06 *Nonlinear Analysis of a Soil-Drilled Pier System under Static and Dynamic Axial Loading.* Gang Wang and Nicholas Sitar. November 2006.

PEER 2006/05 *Advanced Seismic Assessment Guidelines.* Paolo Bazzurro, C. Allin Cornell, Charles Menun, Maziar Motahari, and Nicolas Luco. September 2006.

PEER 2006/04 *Probabilistic Seismic Evaluation of Reinforced Concrete Structural Components and Systems.* Tae Hyung Lee and Khalid M. Mosalam. August 2006.

PEER 2006/03 *Performance of Lifelines Subjected to Lateral Spreading.* Scott A. Ashford and Teerawut Juirnarongrit. July 2006.

PEER 2006/02 *Pacific Earthquake Engineering Research Center Highway Demonstration Project.* Anne Kiremidjian, James Moore, Yue Yue Fan, Nesrin Basoz, Ozgur Yazali, and Meredith Williams. April 2006.

PEER 2006/01 *Bracing Berkeley. A Guide to Seismic Safety on the UC Berkeley Campus.* Mary C. Comerio, Stephen Tobriner, and Ariane Fehrenkamp. January 2006.

PEER 2005/16 *Seismic Response and Reliability of Electrical Substation Equipment and Systems.* Junho Song, Armen Der Kiureghian, and Jerome L. Sackman. April 2006.

PEER 2005/15 *CPT-Based Probabilistic Assessment of Seismic Soil Liquefaction Initiation.* R. E. S. Moss, R. B. Seed, R. E. Kayen, J. P. Stewart, and A. Der Kiureghian. April 2006.

PEER 2005/14 *Workshop on Modeling of Nonlinear Cyclic Load-Deformation Behavior of Shallow Foundations.* Bruce L. Kutter, Geoffrey Martin, Tara Hutchinson, Chad Harden, Sivapalan Gajan, and Justin Phalen. March 2006.

PEER 2005/13 *Stochastic Characterization and Decision Bases under Time-Dependent Aftershock Risk in Performance-Based Earthquake Engineering.* Gee Liek Yeo and C. Allin Cornell. July 2005.

PEER 2005/12 *PEER Testbed Study on a Laboratory Building: Exercising Seismic Performance Assessment.* Mary C. Comerio, editor. November 2005.

PEER 2005/11 *Van Nuys Hotel Building Testbed Report: Exercising Seismic Performance Assessment.* Helmut Krawinkler, editor. October 2005.

PEER 2005/10 *First NEES/E-Defense Workshop on Collapse Simulation of Reinforced Concrete Building Structures.* September 2005.

PEER 2005/09 *Test Applications of Advanced Seismic Assessment Guidelines.* Joe Maffei, Karl Telleen, Danya Mohr, William Holmes, and Yuki Nakayama. August 2006.

PEER 2005/08 *Damage Accumulation in Lightly Confined Reinforced Concrete Bridge Columns.* R. Tyler Ranf, Jared M. Nelson, Zach Price, Marc O. Eberhard, and John F. Stanton. April 2006.

PEER 2005/07 *Experimental and Analytical Studies on the Seismic Response of Freestanding and Anchored Laboratory Equipment.* Dimitrios Konstantinidis and Nicos Makris. January 2005.

PEER 2005/06 *Global Collapse of Frame Structures under Seismic Excitations.* Luis F. Ibarra and Helmut Krawinkler. September 2005.

PEER 2005//05 *Performance Characterization of Bench- and Shelf-Mounted Equipment.* Samit Ray Chaudhuri and Tara C. Hutchinson. May 2006.

PEER 2005/04 *Numerical Modeling of the Nonlinear Cyclic Response of Shallow Foundations.* Chad Harden, Tara Hutchinson, Geoffrey R. Martin, and Bruce L. Kutter. August 2005.

PEER 2005/03 *A Taxonomy of Building Components for Performance-Based Earthquake Engineering.* Keith A. Porter. September 2005.

PEER 2005/02 *Fragility Basis for California Highway Overpass Bridge Seismic Decision Making.* Kevin R. Mackie and Božidar Stojadinović. June 2005.

PEER 2005/01 *Empirical Characterization of Site Conditions on Strong Ground Motion.* Jonathan P. Stewart, Yoojoong Choi, and Robert W. Graves. June 2005.

PEER 2004/09 *Electrical Substation Equipment Interaction: Experimental Rigid Conductor Studies.* Christopher Stearns and André Filiatrault. February 2005.

PEER 2004/08 *Seismic Qualification and Fragility Testing of Line Break 550-kV Disconnect Switches.* Shakhzod M. Takhirov, Gregory L. Fenves, and Eric Fujisaki. January 2005.

PEER 2004/07 *Ground Motions for Earthquake Simulator Qualification of Electrical Substation Equipment.* Shakhzod M. Takhirov, Gregory L. Fenves, Eric Fujisaki, and Don Clyde. January 2005.

PEER 2004/06 *Performance-Based Regulation and Regulatory Regimes.* Peter J. May and Chris Koski. September 2004.

PEER 2004/05 *Performance-Based Seismic Design Concepts and Implementation: Proceedings of an International Workshop.* Peter Fajfar and Helmut Krawinkler, editors. September 2004.

PEER 2004/04 *Seismic Performance of an Instrumented Tilt-up Wall Building.* James C. Anderson and Vitelmo V. Bertero. July 2004.

PEER 2004/03 *Evaluation and Application of Concrete Tilt-up Assessment Methodologies.* Timothy Graf and James O. Malley. October 2004.

PEER 2004/02 *Analytical Investigations of New Methods for Reducing Residual Displacements of Reinforced Concrete Bridge Columns.* Junichi Sakai and Stephen A. Mahin. August 2004.

PEER 2004/01 *Seismic Performance of Masonry Buildings and Design Implications.* Kerri Anne Taeko Tokoro, James C. Anderson, and Vitelmo V. Bertero. February 2004.

PEER 2003/18 *Performance Models for Flexural Damage in Reinforced Concrete Columns.* Michael Berry and Marc Eberhard. August 2003.

PEER 2003/17 *Predicting Earthquake Damage in Older Reinforced Concrete Beam-Column Joints.* Catherine Pagni and Laura Lowes. October 2004.

PEER 2003/16 *Seismic Demands for Performance-Based Design of Bridges.* Kevin Mackie and Božidar Stojadinović. August 2003.

PEER 2003/15 *Seismic Demands for Nondeteriorating Frame Structures and Their Dependence on Ground Motions.* Ricardo Antonio Medina and Helmut Krawinkler. May 2004.

PEER 2003/14 *Finite Element Reliability and Sensitivity Methods for Performance-Based Earthquake Engineering.* Terje Haukaas and Armen Der Kiureghian. April 2004.

PEER 2003/13 *Effects of Connection Hysteretic Degradation on the Seismic Behavior of Steel Moment-Resisting Frames.* Janise E. Rodgers and Stephen A. Mahin. March 2004.

PEER 2003/12 *Implementation Manual for the Seismic Protection of Laboratory Contents: Format and Case Studies.* William T. Holmes and Mary C. Comerio. October 2003.

PEER 2003/11 *Fifth U.S.-Japan Workshop on Performance-Based Earthquake Engineering Methodology for Reinforced Concrete Building Structures.* February 2004.

PEER 2003/10 *A Beam-Column Joint Model for Simulating the Earthquake Response of Reinforced Concrete Frames.* Laura N. Lowes, Nilanjan Mitra, and Arash Altoontash. February 2004.

PEER 2003/09 *Sequencing Repairs after an Earthquake: An Economic Approach.* Marco Casari and Simon J. Wilkie. April 2004.

PEER 2003/08 *A Technical Framework for Probability-Based Demand and Capacity Factor Design (DCFD) Seismic Formats.* Fatemeh Jalayer and C. Allin Cornell. November 2003.

PEER 2003/07 *Uncertainty Specification and Propagation for Loss Estimation Using FOSM Methods.* Jack W. Baker and C. Allin Cornell. September 2003.

PEER 2003/06 *Performance of Circular Reinforced Concrete Bridge Columns under Bidirectional Earthquake Loading.* Mahmoud M. Hachem, Stephen A. Mahin, and Jack P. Moehle. February 2003.

PEER 2003/05 *Response Assessment for Building-Specific Loss Estimation.* Eduardo Miranda and Shahram Taghavi. September 2003.

PEER 2003/04 *Experimental Assessment of Columns with Short Lap Splices Subjected to Cyclic Loads.* Murat Melek, John W. Wallace, and Joel Conte. April 2003.

PEER 2003/03 *Probabilistic Response Assessment for Building-Specific Loss Estimation.* Eduardo Miranda and Hesameddin Aslani. September 2003.

PEER 2003/02 *Software Framework for Collaborative Development of Nonlinear Dynamic Analysis Program.* Jun Peng and Kincho H. Law. September 2003.

PEER 2003/01 *Shake Table Tests and Analytical Studies on the Gravity Load Collapse of Reinforced Concrete Frames.* Kenneth John Elwood and Jack P. Moehle. November 2003.

PEER 2002/24 *Performance of Beam to Column Bridge Joints Subjected to a Large Velocity Pulse.* Natalie Gibson, André Filiatrault, and Scott A. Ashford. April 2002.

PEER 2002/23 *Effects of Large Velocity Pulses on Reinforced Concrete Bridge Columns.* Greg L. Orozco and Scott A. Ashford. April 2002.

PEER 2002/22 *Characterization of Large Velocity Pulses for Laboratory Testing.* Kenneth E. Cox and Scott A. Ashford. April 2002.

PEER 2002/21 *Fourth U.S.-Japan Workshop on Performance-Based Earthquake Engineering Methodology for Reinforced Concrete Building Structures.* December 2002.

PEER 2002/20 *Barriers to Adoption and Implementation of PBEE Innovations.* Peter J. May. August 2002.

PEER 2002/19 *Economic-Engineered Integrated Models for Earthquakes: Socioeconomic Impacts.* Peter Gordon, James E. Moore II, and Harry W. Richardson. July 2002.

PEER 2002/18 *Assessment of Reinforced Concrete Building Exterior Joints with Substandard Details.* Chris P. Pantelides, Jon Hansen, Justin Nadauld, and Lawrence D. Reaveley. May 2002.

PEER 2002/17 *Structural Characterization and Seismic Response Analysis of a Highway Overcrossing Equipped with Elastomeric Bearings and Fluid Dampers: A Case Study.* Nicos Makris and Jian Zhang. November 2002.

PEER 2002/16 *Estimation of Uncertainty in Geotechnical Properties for Performance-Based Earthquake Engineering.* Allen L. Jones, Steven L. Kramer, and Pedro Arduino. December 2002.

PEER 2002/15 *Seismic Behavior of Bridge Columns Subjected to Various Loading Patterns.* Asadollah Esmaeily-Gh. and Yan Xiao. December 2002.

PEER 2002/14 *Inelastic Seismic Response of Extended Pile Shaft Supported Bridge Structures.* T.C. Hutchinson, R.W. Boulanger, Y.H. Chai, and I.M. Idriss. December 2002.

PEER 2002/13 *Probabilistic Models and Fragility Estimates for Bridge Components and Systems.* Paolo Gardoni, Armen Der Kiureghian, and Khalid M. Mosalam. June 2002.

PEER 2002/12 *Effects of Fault Dip and Slip Rake on Near-Source Ground Motions: Why Chi-Chi Was a Relatively Mild M7.6 Earthquake.* Brad T. Aagaard, John F. Hall, and Thomas H. Heaton. December 2002.

PEER 2002/11 *Analytical and Experimental Study of Fiber-Reinforced Strip Isolators*. James M. Kelly and Shakhzod M. Takhirov. September 2002.

PEER 2002/10 *Centrifuge Modeling of Settlement and Lateral Spreading with Comparisons to Numerical Analyses***.** Sivapalan Gajan and Bruce L. Kutter. January 2003.

PEER 2002/09 *Documentation and Analysis of Field Case Histories of Seismic Compression during the 1994 Northridge, California, Earthquake.* Jonathan P. Stewart, Patrick M. Smith, Daniel H. Whang, and Jonathan D. Bray. October 2002.

PEER 2002/08 *Component Testing, Stability Analysis and Characterization of Buckling-Restrained Unbonded Braces™.* Cameron Black, Nicos Makris, and Ian Aiken. September 2002.

PEER 2002/07 *Seismic Performance of Pile-Wharf Connections.* Charles W. Roeder, Robert Graff, Jennifer Soderstrom, and Jun Han Yoo. December 2001.

PEER 2002/06 *The Use of Benefit-Cost Analysis for Evaluation of Performance-Based Earthquake Engineering Decisions*. Richard O. Zerbe and Anthony Falit-Baiamonte. September 2001.

PEER 2002/05 *Guidelines, Specifications, and Seismic Performance Characterization of Nonstructural Building Components and Equipment*. André Filiatrault, Constantin Christopoulos, and Christopher Stearns. September 2001.

PEER 2002/04 *Consortium of Organizations for Strong-Motion Observation Systems and the Pacific Earthquake Engineering Research Center Lifelines Program: Invited Workshop on Archiving and Web Dissemination of Geotechnical Data, 4–5 October 2001*. September 2002.

PEER 2002/03 *Investigation of Sensitivity of Building Loss Estimates to Major Uncertain Variables for the Van Nuys Testbed.* Keith A. Porter, James L. Beck, and Rustem V. Shaikhutdinov. August 2002.

PEER 2002/02 *The Third U.S.-Japan Workshop on Performance-Based Earthquake Engineering Methodology for Reinforced Concrete Building Structures*. July 2002.

PEER 2002/01 *Nonstructural Loss Estimation: The UC Berkeley Case Study.* Mary C. Comerio and John C. Stallmeyer. December 2001.

PEER 2001/16 *Statistics of SDF-System Estimate of Roof Displacement for Pushover Analysis of Buildings.* Anil K. Chopra, Rakesh K. Goel, and Chatpan Chintanapakdee. December 2001.

PEER 2001/15 *Damage to Bridges during the 2001 Nisqually Earthquake.* R. Tyler Ranf, Marc O. Eberhard, and Michael P. Berry. November 2001.

PEER 2001/14 *Rocking Response of Equipment Anchored to a Base Foundation.* Nicos Makris and Cameron J. Black. September 2001.

PEER 2001/13 *Modeling Soil Liquefaction Hazards for Performance-Based Earthquake Engineering.* Steven L. Kramer and Ahmed-W. Elgamal. February 2001.

PEER 2001/12 *Development of Geotechnical Capabilities in OpenSees.* Boris Jeremić. September 2001.

PEER 2001/11 *Analytical and Experimental Study of Fiber-Reinforced Elastomeric Isolators.* James M. Kelly and Shakhzod M. Takhirov. September 2001.

PEER 2001/10 *Amplification Factors for Spectral Acceleration in Active Regions.* Jonathan P. Stewart, Andrew H. Liu, Yoojoong Choi, and Mehmet B. Baturay. December 2001.

PEER 2001/09 *Ground Motion Evaluation Procedures for Performance-Based Design.* Jonathan P. Stewart, Shyh-Jeng Chiou, Jonathan D. Bray, Robert W. Graves, Paul G. Somerville, and Norman A. Abrahamson. September 2001.

PEER 2001/08 *Experimental and Computational Evaluation of Reinforced Concrete Bridge Beam-Column Connections for Seismic Performance.* Clay J. Naito, Jack P. Moehle, and Khalid M. Mosalam. November 2001.

PEER 2001/07 *The Rocking Spectrum and the Shortcomings of Design Guidelines.* Nicos Makris and Dimitrios Konstantinidis. August 2001.

PEER 2001/06 *Development of an Electrical Substation Equipment Performance Database for Evaluation of Equipment Fragilities.* Thalia Agnanos. April 1999.

PEER 2001/05 *Stiffness Analysis of Fiber-Reinforced Elastomeric Isolators.* Hsiang-Chuan Tsai and James M. Kelly. May 2001.

PEER 2001/04 *Organizational and Societal Considerations for Performance-Based Earthquake Engineering.* Peter J. May. April 2001.

PEER 2001/03 *A Modal Pushover Analysis Procedure to Estimate Seismic Demands for Buildings: Theory and Preliminary Evaluation.* Anil K. Chopra and Rakesh K. Goel. January 2001.

PEER 2001/02 *Seismic Response Analysis of Highway Overcrossings Including Soil-Structure Interaction.* Jian Zhang and Nicos Makris. March 2001.

PEER 2001/01 *Experimental Study of Large Seismic Steel Beam-to-Column Connections.* Egor P. Popov and Shakhzod M. Takhirov. November 2000.

PEER 2000/10 *The Second U.S.-Japan Workshop on Performance-Based Earthquake Engineering Methodology for Reinforced Concrete Building Structures.* March 2000.

PEER 2000/09 *Structural Engineering Reconnaissance of the August 17, 1999 Earthquake: Kocaeli (Izmit), Turkey.* Halil Sezen, Kenneth J. Elwood, Andrew S. Whittaker, Khalid Mosalam, John J. Wallace, and John F. Stanton. December 2000.

PEER 2000/08 *Behavior of Reinforced Concrete Bridge Columns Having Varying Aspect Ratios and Varying Lengths of Confinement.* Anthony J. Calderone, Dawn E. Lehman, and Jack P. Moehle. January 2001.

PEER 2000/07 *Cover-Plate and Flange-Plate Reinforced Steel Moment-Resisting Connections.* Taejin Kim, Andrew S. Whittaker, Amir S. Gilani, Vitelmo V. Bertero, and Shakhzod M. Takhirov. September 2000.

PEER 2000/06 *Seismic Evaluation and Analysis of 230-kV Disconnect Switches.* Amir S. J. Gilani, Andrew S. Whittaker, Gregory L. Fenves, Chun-Hao Chen, Henry Ho, and Eric Fujisaki. July 2000.

PEER 2000/05 *Performance-Based Evaluation of Exterior Reinforced Concrete Building Joints for Seismic Excitation.* Chandra Clyde, Chris P. Pantelides, and Lawrence D. Reaveley. July 2000.

PEER 2000/04 *An Evaluation of Seismic Energy Demand: An Attenuation Approach.* Chung-Che Chou and Chia-Ming Uang. July 1999.

PEER 2000/03 *Framing Earthquake Retrofitting Decisions: The Case of Hillside Homes in Los Angeles.* Detlof von Winterfeldt, Nels Roselund, and Alicia Kitsuse. March 2000.

PEER 2000/02 *U.S.-Japan Workshop on the Effects of Near-Field Earthquake Shaking.* Andrew Whittaker, ed. July 2000.

PEER 2000/01 *Further Studies on Seismic Interaction in Interconnected Electrical Substation Equipment.* Armen Der Kiureghian, Kee-Jeung Hong, and Jerome L. Sackman. November 1999.

PEER 1999/14 *Seismic Evaluation and Retrofit of 230-kV Porcelain Transformer Bushings.* Amir S. Gilani, Andrew S. Whittaker, Gregory L. Fenves, and Eric Fujisaki. December 1999.

PEER 1999/13 *Building Vulnerability Studies: Modeling and Evaluation of Tilt-up and Steel Reinforced Concrete Buildings.* John W. Wallace, Jonathan P. Stewart, and Andrew S. Whittaker, editors. December 1999.

PEER 1999/12 *Rehabilitation of Nonductile RC Frame Building Using Encasement Plates and Energy-Dissipating Devices.* Mehrdad Sasani, Vitelmo V. Bertero, James C. Anderson. December 1999.

PEER 1999/11 *Performance Evaluation Database for Concrete Bridge Components and Systems under Simulated Seismic Loads.* Yael D. Hose and Frieder Seible. November 1999.

PEER 1999/10 *U.S.-Japan Workshop on Performance-Based Earthquake Engineering Methodology for Reinforced Concrete Building Structures.* December 1999.

PEER 1999/09 *Performance Improvement of Long Period Building Structures Subjected to Severe Pulse-Type Ground Motions*. James C. Anderson, Vitelmo V. Bertero, and Raul Bertero. October 1999.

PEER 1999/08 *Envelopes for Seismic Response Vectors.* Charles Menun and Armen Der Kiureghian. July 1999.

PEER 1999/07 *Documentation of Strengths and Weaknesses of Current Computer Analysis Methods for Seismic Performance of Reinforced Concrete Members.* William F. Cofer. November 1999.

PEER 1999/06 *Rocking Response and Overturning of Anchored Equipment under Seismic Excitations.* Nicos Makris and Jian Zhang. November 1999.

PEER 1999/05 *Seismic Evaluation of 550 kV Porcelain Transformer Bushings.* Amir S. Gilani, Andrew S. Whittaker, Gregory L. Fenves, and Eric Fujisaki. October 1999.

PEER 1999/04 *Adoption and Enforcement of Earthquake Risk-Reduction Measures.* Peter J. May, Raymond J. Burby, T. Jens Feeley, and Robert Wood.

PEER 1999/03 *Task 3 Characterization of Site Response General Site Categories*. Adrian Rodriguez-Marek, Jonathan D. Bray, and Norman Abrahamson. February 1999.

PEER 1999/02 *Capacity-Demand-Diagram Methods for Estimating Seismic Deformation of Inelastic Structures: SDF Systems*. Anil K. Chopra and Rakesh Goel. April 1999.

PEER 1999/01 *Interaction in Interconnected Electrical Substation Equipment Subjected to Earthquake Ground Motions.* Armen Der Kiureghian, Jerome L. Sackman, and Kee-Jeung Hong. February 1999.

PEER 1998/08 *Behavior and Failure Analysis of a Multiple-Frame Highway Bridge in the 1994 Northridge Earthquake.* Gregory L. Fenves and Michael Ellery. December 1998.

PEER 1998/07 *Empirical Evaluation of Inertial Soil-Structure Interaction Effects.* Jonathan P. Stewart, Raymond B. Seed, and Gregory L. Fenves. November 1998.

PEER 1998/06 *Effect of Damping Mechanisms on the Response of Seismic Isolated Structures.* Nicos Makris and Shih-Po Chang. November 1998.

PEER 1998/05 *Rocking Response and Overturning of Equipment under Horizontal Pulse-Type Motions.* Nicos Makris and Yiannis Roussos. October 1998.

PEER 1998/04 *Pacific Earthquake Engineering Research Invitational Workshop Proceedings, May 14–15, 1998: Defining the Links between Planning, Policy Analysis, Economics and Earthquake Engineering.* Mary Comerio and Peter Gordon. September 1998.

PEER 1998/03 *Repair/Upgrade Procedures for Welded Beam to Column Connections.* James C. Anderson and Xiaojing Duan. May 1998.

PEER 1998/02 *Seismic Evaluation of 196 kV Porcelain Transformer Bushings.* Amir S. Gilani, Juan W. Chavez, Gregory L. Fenves, and Andrew S. Whittaker. May 1998.

PEER 1998/01 *Seismic Performance of Well-Confined Concrete Bridge Columns.* Dawn E. Lehman and Jack P. Moehle. December 2000.

ONLINE PEER REPORTS

The following PEER reports are available by Internet only at http://peer.berkeley.edu/publications/peer_reports_complete.html.

PEER 2012/103 *Performance-Based Seismic Demand Assessment of Concentrically Braced Steel Frame Buildings.* Chui-Hsin Chen and Stephen A. Mahin. December 2012.

PEER 2012/102 *Procedure to Restart an Interrupted Hybrid Simulation: Addendum to PEER Report 2010/103.* Vesna Terzic and Bozidar Stojadinovic. October 2012.

PEER 2012/101 *Mechanics of Fiber Reinforced Bearings.* James M. Kelly and Andrea Calabrese. February 2012.

PEER 2011/107 *Nonlinear Site Response and Seismic Compression at Vertical Array Strongly Shaken by 2007 Niigata-ken Chuetsu-oki Earthquake.* Eric Yee, Jonathan P. Stewart, and Kohji Tokimatsu. December 2011.

PEER 2011/106 *Self Compacting Hybrid Fiber Reinforced Concrete Composites for Bridge Columns.* Pardeep Kumar, Gabriel Jen, William Trono, Marios Panagiotou, and Claudia Ostertag. September 2011.

PEER 2011/105 *Stochastic Dynamic Analysis of Bridges Subjected to Spacially Varying Ground Motions.* Katerina Konakli and Armen Der Kiureghian. August 2011.

PEER 2011/104 *Design and Instrumentation of the 2010 E-Defense Four-Story Reinforced Concrete and Post-Tensioned Concrete Buildings.* Takuya Nagae, Kenichi Tahara, Taizo Matsumori, Hitoshi Shiohara, Toshimi Kabeyasawa, Susumu Kono, Minehiro Nishiyama (Japanese Research Team) and John Wallace, Wassim Ghannoum, Jack Moehle, Richard Sause, Wesley Keller, Zeynep Tuna (U.S. Research Team). June 2011.

PEER 2011/103 *In-Situ Monitoring of the Force Output of Fluid Dampers: Experimental Investigation.* Dimitrios Konstantinidis, James M. Kelly, and Nicos Makris. April 2011.

PEER 2011/102 *Ground-motion prediction equations 1964 - 2010.* John Douglas. April 2011.

PEER 2011/101 *Report of the Eighth Planning Meeting of NEES/E-Defense Collaborative Research on Earthquake Engineering.* Convened by the Hyogo Earthquake Engineering Research Center (NIED), NEES Consortium, Inc. February 2011.

PEER 2010/111 *Modeling and Acceptance Criteria for Seismic Design and Analysis of Tall Buildings.* Task 7 Report for the Tall Buildings Initiative - Published jointly by the Applied Technology Council. October 2010.

PEER 2010/110 *Seismic Performance Assessment and Probabilistic Repair Cost Analysis of Precast Concrete Cladding Systems for Multistory Buildlings.* Jeffrey P. Hunt and Božidar Stojadinovic. November 2010.

PEER 2010/109 *Report of the Seventh Joint Planning Meeting of NEES/E-Defense Collaboration on Earthquake Engineering. Held at the E-Defense, Miki, and Shin-Kobe, Japan, September 18–19, 2009.* August 2010.

PEER 2010/108 *Probabilistic Tsunami Hazard in California.* Hong Kie Thio, Paul Somerville, and Jascha Polet, preparers. October 2010.

PEER 2010/107 *Performance and Reliability of Exposed Column Base Plate Connections for Steel Moment-Resisting Frames.* Ady Aviram, Božidar Stojadinovic, and Armen Der Kiureghian. August 2010.

PEER 2010/106 *Verification of Probabilistic Seismic Hazard Analysis Computer Programs.* Patricia Thomas, Ivan Wong, and Norman Abrahamson. May 2010.

PEER 2010/105 *Structural Engineering Reconnaissance of the April 6, 2009, Abruzzo, Italy, Earthquake, and Lessons Learned.* M. Selim Günay and Khalid M. Mosalam. April 2010.

PEER 2010/104 *Simulating the Inelastic Seismic Behavior of Steel Braced Frames, Including the Effects of Low-Cycle Fatigue.* Yuli Huang and Stephen A. Mahin. April 2010.

PEER 2010/103 *Post-Earthquake Traffic Capacity of Modern Bridges in California.* Vesna Terzic and Božidar Stojadinović. March 2010.

PEER 2010/102 *Analysis of Cumulative Absolute Velocity (CAV) and JMA Instrumental Seismic Intensity (I_{JMA}) Using the PEER–NGA Strong Motion Database.* Kenneth W. Campbell and Yousef Bozorgnia. February 2010.

PEER 2010/101 *Rocking Response of Bridges on Shallow Foundations.* Jose A. Ugalde, Bruce L. Kutter, and Boris Jeremic. April 2010.

PEER 2009/109 *Simulation and Performance-Based Earthquake Engineering Assessment of Self-Centering Post-Tensioned Concrete Bridge Systems.* Won K. Lee and Sarah L. Billington. December 2009.

PEER 2009/108 *PEER Lifelines Geotechnical Virtual Data Center.* J. Carl Stepp, Daniel J. Ponti, Loren L. Turner, Jennifer N. Swift, Sean Devlin, Yang Zhu, Jean Benoit, and John Bobbitt. September 2009.

PEER 2009/107 *Experimental and Computational Evaluation of Current and Innovative In-Span Hinge Details in Reinforced Concrete Box-Girder Bridges: Part 2: Post-Test Analysis and Design Recommendations.* Matias A. Hube and Khalid M. Mosalam. December 2009.

PEER 2009/106 *Shear Strength Models of Exterior Beam-Column Joints without Transverse Reinforcement.* Sangjoon Park and Khalid M. Mosalam. November 2009.

PEER 2009/105 *Reduced Uncertainty of Ground Motion Prediction Equations through Bayesian Variance Analysis.* Robb Eric S. Moss. November 2009.

PEER 2009/104 *Advanced Implementation of Hybrid Simulation.* Andreas H. Schellenberg, Stephen A. Mahin, Gregory L. Fenves. November 2009.

PEER 2009/103 *Performance Evaluation of Innovative Steel Braced Frames.* T. Y. Yang, Jack P. Moehle, and Božidar Stojadinovic. August 2009.

PEER 2009/102 *Reinvestigation of Liquefaction and Nonliquefaction Case Histories from the 1976 Tangshan Earthquake.* Robb Eric Moss, Robert E. Kayen, Liyuan Tong, Songyu Liu, Guojun Cai, and Jiaer Wu. August 2009.

PEER 2009/101 *Report of the First Joint Planning Meeting for the Second Phase of NEES/E-Defense Collaborative Research on Earthquake Engineering.* Stephen A. Mahin et al. July 2009.

PEER 2008/104 *Experimental and Analytical Study of the Seismic Performance of Retaining Structures.* Linda Al Atik and Nicholas Sitar. January 2009.

PEER 2008/103 *Experimental and Computational Evaluation of Current and Innovative In-Span Hinge Details in Reinforced Concrete Box-Girder Bridges. Part 1: Experimental Findings and Pre-Test Analysis.* Matias A. Hube and Khalid M. Mosalam. January 2009.

PEER 2008/102 *Modeling of Unreinforced Masonry Infill Walls Considering In-Plane and Out-of-Plane Interaction.* Stephen Kadysiewski and Khalid M. Mosalam. January 2009.

PEER 2008/101 *Seismic Performance Objectives for Tall Buildings.* William T. Holmes, Charles Kircher, William Petak, and Nabih Youssef. August 2008.

PEER 2007/101 *Generalized Hybrid Simulation Framework for Structural Systems Subjected to Seismic Loading.* Tarek Elkhoraibi and Khalid M. Mosalam. July 2007.

PEER 2007/100 *Seismic Evaluation of Reinforced Concrete Buildings Including Effects of Masonry Infill Walls.* Alidad Hashemi and Khalid M. Mosalam. July 2007.

The Pacific Earthquake Engineering Research Center (PEER) is a multi-institutional research and education center with headquarters at the University of California, Berkeley. Investigators from over 20 universities, several consulting companies, and researchers at various state and federal government agencies contribute to research programs focused on performance-based earthquake engineering.

These research programs aim to identify and reduce the risks from major earthquakes to life safety and to the economy by including research in a wide variety of disciplines including structural and geotechnical engineering, geology/seismology, lifelines, transportation, architecture, economics, risk management, and public policy.

PEER is supported by federal, state, local, and regional agencies, together with industry partners.

PEER Core Institutions:
University of California, Berkeley (Lead Institution)
California Institute of Technology
Oregon State University
Stanford University
University of California, Davis
University of California, Irvine
University of California, Los Angeles
University of California, San Diego
University of Southern California
University of Washington

PEER reports can be ordered at http://peer.berkeley.edu/publications/peer_reports.html or by contacting

Pacific Earthquake Engineering Research Center
University of California, Berkeley
325 Davis Hall, mail code 1792
Berkeley, CA 94720-1792
Tel: 510-642-3437
Fax: 510-642-1655
Email: peer_editor@berkeley.edu

ISSN 1547-0587X